Università degli Studi di Torino
Scuola di Dottorato in Scienza ed Alta Tecnologia

First observation of the rare decay mode $K^+ \to \mu^+\nu(\mu)\mu^+\mu^-$ in the NA62 experiment at CERN SPS

Marco Boretto

Tutor: Ezio Menichetti
Co-Tutor: Giovanna Lehmann Miotto

Contents

A mio zio, che oggi non può essere qui...

Introduction

High energy colliders provide tools to investigate the frontiers of subnuclear physics knowledge by probing the ultimate constituents of matter within smaller and smaller space-time regions. A complementary approach to the understanding of the fundamental properties of nature is the study at a very high degree of precision of rare phenomena, which clarify critical items of the theories and open the possibility of discriminating between different physics models.

The NA62 experiment pursues the latter line of research: it aims at measuring the Branching Ratio (BR) of the extremely rare kaon decay: $K^+ \to \pi^+\nu\bar{\nu}$. This process is a flavour-changing neutral current (FCNC) decay; its amplitude is reduced by the quadratic GIM mechanism and the Cabibbo suppression. In the Standard Model $BR(K^+ \to \pi^+\nu\bar{\nu}) = (8.4 \pm 1.0) \cdot 10^{-11}$[1]; the prediction is particularly clean and the dominant contribution arises from the short-distance physics of the top-quark loop. The BR of this decay, since the rate is low and the corresponding error very precise, is an excellent probe of new physics.

To precisely measure such a small quantity, a beam of high intensity is needed. The abundant production of K^+ mesons paves the way to a broad collateral program of physics: the charged kaon decay modes, up the $K^+ \to \pi^+\nu\bar{\nu}$, can be studied as never before. In this thesis, the first measurement of the $K^+ \to \mu^+\nu_\mu\mu^+\mu^-$ Branching Ratio is presented. The measurement uses the data collected during the 2017 data-taking by the NA62 collaboration.

The thesis is organised as follow: the first chapter introduces the physics behind the rare kaon decays in the Chiral Perturbation Theory framework; after that, the NA62 detector and the beam line will be presented. The author of the thesis gave a contribution to the renovation of the Data AcQuisition (DAQ) system in view of the 2017 data-taking; for that reason, a description of the NA62 DAQ system will be given in chapter 3. Finally, chapter 4 is devoted to the $K^+ \to \mu^+\nu_\mu\mu^+\mu^-$ analysis strategy and to the measurement of the BR.

1

Theoretical Introduction

1.1 Rare kaon decays

Kaon physics has played a major role in the development of Standard Model, from the discovery of the strange flavour, parity and CP violation, $SU(3)$ and quark model, flavour mixing, flavour changing neutral currents suppression and GIM mechanism. The subfield of rare kaon decays covers a wide range of processes induced by the weak interaction, allowing for interesting tests of the Standard Model and, most importantly, for sensitive probing of new physics. While the main goal of the NA62 experiment at the CERN SPS is a new measurement of the ultrarare decay $K^+ \to \pi^+\nu\bar{\nu}$, the beam and detector are ideally suited to improve the measurement of many other K^+ rare decays. The subject of this work is the study of the rare decay mode

$$K^+ \to \mu^+\nu_\mu\mu^+\mu^-, \tag{1.1}$$

never observed in previous experiments.

Kaon decay processes originate from a complicated mix of effects of weak, electromagnetic and strong interactions. Following the Particle Data Group[2], the charged kaon decays can be classified as leptonic, semileptonic and hadronic modes. The total fraction accounted, adding together the seven most common leptonic, semileptonic and hadronic

Process	Short name	Mode	BR
$K^+ \to \mu^+\nu_\mu$	$K_{\mu 2}$	Leptonic	$(63.56 \pm 0.11)\%$
$K^+ \to \pi^+\pi^0$	$K_{2\pi}$	Hadronic	$(20.67 \pm 0.08)\%$
$K^+ \to \pi^+\pi^-\pi^+$	$K_{3\pi}$	Hadronic	$(5.583 \pm 0.024)\%$
$K^+ \to \pi^0 e^+\nu_e$	K_{e3}	Semileptonic	$(5.07 \pm 0.04)\%$
$K^+ \to \pi^0\mu^+\nu_\mu$	$K_{\mu 3}$	Semileptonic	$(3.352 \pm 0.033)\%$
$K^+ \to \pi^+\pi^0\pi^0$	$K_{2\pi}$	Hadronic	$(1.760 \pm 0.0023)\%$
$K^+ \to \mu^+\nu_\mu\gamma$		Leptonic with photons	$(6.2 \pm 0.8) \cdot 10^{-3}$
Total			$> 99\%$

Table 1.1: Most common kaon decays and their branching ratio. The main seven decay modes account for more than 99% of the total fraction.

decays, is more than 99%. All the remaining channels, more than 30 including several predicted but not yet observed, can be defined as rare decays, most often occurring as electroweak radiative corrections to main modes. The experimental study of rare kaon decays has several motivations, ranging from search of new physics beyond the Standard Model, like lepton flavour violation, to precision measurement of poorly known CKM elements via strongly suppressed modes, to accurate validation of low energy behaviour of QCD by testing the Chiral Perturbation Theory.

1.2 Chiral Perturbation Theory

The Chiral Perturbation Theory (ChPT), the effective field theory of the Standard Model (SM) at low energies, describes the physics of light flavour u, d and s. The symmetries are the main input for the construction of the ChPT, the domain of validity is restricted to the confinement of QCD, at energies below of m_ρ.

The chiral symmetry arises theoretically from the chiral limit that assumes the quarks u, d and s massless. Under that constraint, the QCD Lagrangian can be written as

$$\mathcal{L}^0_{QCD} = i\bar{q}_L \not{D} q_L + i\bar{q}_R \not{D} q_R \tag{1.2}$$

Where the right and the left handed quark fields are given by

$$q_{R,L} = \frac{1}{2}(1 \pm \gamma_5)q \qquad q \equiv \begin{pmatrix} u \\ d \\ s \end{pmatrix} \tag{1.3}$$

The QCD Lagrangian $\mathcal{L}^0_{QCD}$ exibits a chiral symmetry:

$$G_\chi = SU(3)_L \times SU(3)_R \tag{1.4}$$

which is called chiral because it acts differently on the left and right-handed quarks. The chiral symmetry G_χ is spontaneously broken to the vectorial subgroup $SU(3)_V$:

$$G_\chi \to H = SU(3)_V. \tag{1.5}$$

Spontaneously broken symmetries are realised nonlinearly on the Goldstone boson fields, in the case of the chiral symmetry there are $F^2 - 1$ fields. For the three-flavour case ($n_F = 3$), there are eight broken generators, and as a consequence, eight Goldstone boson degrees of freedom are expected. The octet of pseudoscalar mesons is the natural candidate, it is composed of the three pions, π^0, $\pi^\pm$, the four kaons, $K^\pm$, K^0, $\bar{K}^0$ and the eta, η. The Goldstone theorem thus explains their low mass compared to the other hadrons as well as the fact that their interactions are relatively weak.

1.2.1 Lowest order ChPT

The resulting Goldstone boson can be parameterised by a special unitary matrix U which transforms under the chiral symmetry group:

$$U = e^{i\sqrt{2}M/F_\pi} \text{ with } M = \begin{pmatrix} \frac{1}{\sqrt{2}}\pi^0 + \frac{1}{\sqrt{6}}\eta & \pi^+ & K^+ \\ \pi^- & -\frac{1}{\sqrt{2}}\pi^0 + \frac{1}{\sqrt{6}}\eta & K^0 \\ K^- & \bar{K}^0 & -\frac{2}{\sqrt{6}}\eta \end{pmatrix} \tag{1.6}$$

At the lowest order in quarks momentum $O(p^2)$ the chiral Lagrangian compatible with Lorentz invariance and with the chiral symmetry group can be defined as follow:

$$\mathcal{L}_2 = \frac{F_\pi^2}{4} Tr[D_\mu U^\dagger D^\mu U + \chi U^\dagger + U\chi^\dagger] \tag{1.7}$$

with

$$\chi = 2B(s + ip) \tag{1.8}$$

Where D_μ is the covariant derivative, F_π and B are related to the pion decay constant and to the quark condensate.

1.2.2 Higher orders ChPT

At the leading order two constant F_π and B are enough to determine the low energy behaviour of the Green functions, at the next-to-leading-order, $O(p^4)$, there are 10 new low energy constants $L_1, ..., L_{10}$. Since the L_i constants have been determined phenomenologically, there is a completely predictive scheme to this order. Currently the Chiral Perturbation Theory calculation has been worked out until the next-to-next-to-leading-order (NNLO) $O(p^6)$[3]. The ChPT is a large subject; more information can be found in the following reviews[3, 4, 5, 6] which are also the main sources of this section.

1.3 Leptonic decays

Leptonic and semileptonic decays are the cleanest from the theoretical point of view: Chiral Perturbation Theory and lattice QCD predictions allow for accurate calculations of branching fractions and decays distributions, providing nontrivial checks of the Standard Model. For example, a typical prediction is the ratio R of leptonic modes for the pseudoscalar mesons helicity suppressed in the Standard Model due to $V - A$ structure of charged current couplings. The K decay rates ratio

$$R^K_{e/\mu} = \frac{\Gamma(K^+ \to e^+\nu_e)}{\Gamma(K^+ \to \mu^+\nu_\mu)} \tag{1.9}$$

is a sensitive probe of all SM extensions yielding pseudoscalar currents and non-universal corrections to the lepton couplings.

The simplest Feynman diagram for the leptonic decay process $K^+ \to \mu^+\nu_\mu$ is shown in figure 1.1.

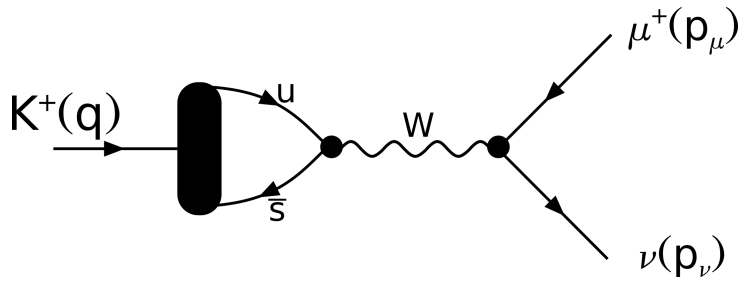

Figure 1.1: Feynman diagram for the leptonic decay process $K^+ \to \mu^+\nu_\mu$.

Since the quarks are not free inside the hadron, the matrix element is

$$M = -i\frac{G_F}{\sqrt{2}}\bar{u_2}\gamma_\mu(1-\gamma^5)v_1\langle 0|J^{h\mu\dagger}(0)|K^+(q)\rangle \tag{1.10}$$

where $q = p_{K^+} = p_{\nu_\mu} + p_\mu$. The hadronic current is

$$\langle 0|J^{h\mu\dagger}(0)|K^+(q)\rangle = -i\sin\theta_C f_K q^\mu e^{-iq\cdot x}, \tag{1.11}$$

where the θ_C is the Cabibbo angle and f_K is the kaon decay constant. Thus using the Dirac equation,

$$M = \frac{-f_K G_F \sin\theta_C}{\sqrt{2}}\bar{u}_2(\not{p}_1 + \not{p}_2)(1-\gamma^5)v_1 \sim \frac{-f_K m_\mu G_F \sin\theta_C}{\sqrt{2}}\bar{u}_2(1-\gamma^5)v_1 \tag{1.12}$$

where m_ν is neglected. Summing over the final spins

$$|\bar{M}|^2 = \sum_{s_1 s_2}|M|^2 = \frac{f_K^2 m_\mu^2 G_F^2 \sin^2\theta_C}{2} Tr[(1-\gamma^5)\not{p}_1(1+\gamma^5)(\not{p}_2 + m_\mu)] \tag{1.13}$$

where

$$Tr[(1-\gamma^5)\not{p}_1(1+\gamma^5)(\not{p}_2 + m_\mu)] = 8p_1\cdot p_2 = 4(m_K^2 - m_\mu^2) \tag{1.14}$$

so that

$$|\bar{M}|^2 = \sum_{s_1 s_2}|M|^2 = \frac{f_K^2 m_\mu^2 G_F^2 \sin^2\theta_C}{2} 4(m_K^2 - m_\mu^2) \tag{1.15}$$

For a 2-body decay the differential decay rate is

$$\begin{aligned} d\Gamma &= \frac{(2\pi)^4\delta^4(p_\mu + p_\nu - p_K)}{2m_K}\frac{d^3\vec{p_\nu}}{(2\pi)^3 2E_\nu}\frac{d^3\vec{p_\mu}}{(2\pi)^3 2E_\mu}|M|^2 \\ &= \frac{|M|^2}{32\pi^2 m_K}[\frac{p_\nu E_\nu dE_\nu}{E_\nu E_\mu}\delta(E_\nu + E_\mu - m_K)]d\Omega \\ &= \frac{p_\nu}{32\pi^2 m_K^2}|M|^2 d\Omega \end{aligned} \tag{1.16}$$

$$\Gamma = \frac{p_\nu}{32\pi^2 m_K^2}|M|^2 \underbrace{\int d\Omega}_{4\pi} = \frac{p_\nu}{8\pi m_K^2}|\bar{M}|^2 \tag{1.17}$$

Remembering that

$$\frac{p_\nu}{m_K} = \frac{\sqrt{m_K^2 - (\cancel{m_\nu} + m_\mu)^2}\sqrt{m_K^2 - (\cancel{m_\nu} + m_\mu)^2}}{2m_K^2} = \frac{m_K^2 - m_\mu^2}{2m_K^2} \tag{1.18}$$

and neglecting m_ν. The final decay rate $\Gamma(K^+ \to \mu^+\nu_\mu)$ is

$$\tau^{-1} = \Gamma(K^+ \to \mu^+\nu_\mu) = \frac{p_\nu}{8\pi m_K^2}|\bar{M}|^2 = \frac{G_F^2 \sin^2\theta_C f_K^2 m_K}{8\pi} m_\mu^2\Big(1 - \frac{m_\mu^2}{m_K^2}\Big)^2 \tag{1.19}$$

The kaon decay constant f_K, characterising the strong interaction effects on the $u\bar{s}$ weak annihilation probability, is difficult to compute in a bound state, non-perturbative QCD regime. Indeed, at low energies, the relevant degrees of freedom of the Standard Model

are not quarks and gluons, but rather the pseudoscalar mesons and other hadrons. In spite of the difficulties coming from the large value of QCD coupling constant, at low energies, the Standard Model in the hadronic sector can be effectively described by the Chiral Perturbation Theory.

The rate of $K^+ \to e^+\nu_e$ has the same form as 1.19 except that $m_\mu \to m_e$. Therefore the K decay rates ratio can be computed with a very accurate prediction[7]:

$$R^K_{e/\mu} = \frac{\Gamma(K^+ \to e^+\nu_e)}{\Gamma(K^+ \to \mu^+\nu_\mu)} = \frac{m_e^2}{m_\mu^2}\Big(\frac{m_K^2 - m_e^2}{m_K^2 - m_\mu^2}\Big)^2 = (2.477 \pm 0.001) \cdot 10^{-5} \tag{1.20}$$

to be compared to the most precise measurement available[8]

$$R^K_{e/\mu} = (2.488 \pm 0.0007_{stat} \pm 0.0007_{syst}) \cdot 10^{-5}. \tag{1.21}$$

1.4 K_{l2ll} decays

The kaon K_{l2ll} decays are K_{l2} radiative decays with a virtual photon producing a lepton pair. Radiative leptonic kaon decays and their internally converted partners, like

$$K^+ \to \mu^+\nu_\mu\gamma, \quad K^+ \to \mu^+\nu_\mu\mu^+\mu^- \tag{1.22}$$

are both a source of information and a test on the ChPT. The processes contributing to the radiative decay amplitudes are depicted in figure 1.2. The first two diagrams, where the photon is emitted by the final muon, or even by the initial kaon, are called Inner Bremmstrahlung (IB), while the third one, where the photon originates by some internal quark line, is called Structure Dependent (SD). While the IB contribution is a standard QED amplitude, the SD term is more interesting, since it is tied to the kaon inner structure, where ChPT is supposed to yield accurate predictions.

1.4.1 The $K^+ \to \mu^+\nu_\mu\mu^+\mu^-$ decay

The $K^+ \to \mu^+\nu_\mu\mu^+\mu^-$ decay, also indicated as $K_{\mu\nu\mu\mu}$, amplitude can be directly estimated from the Chiral Perturbation Theory. The subject has not been studied extensively in literature, the only source that provides the $BR(K^+ \to \mu^+\nu_\mu\mu^+\mu^-)$, considering both IB and SD contributions, is the "Radiative semileptonic kaon decays"[10] article published in 1992. The article derives the BR of radiative kaon decays using the next-to-leading-order $O(p^4)$ Chiral Perturbation Theory Lagrangian.

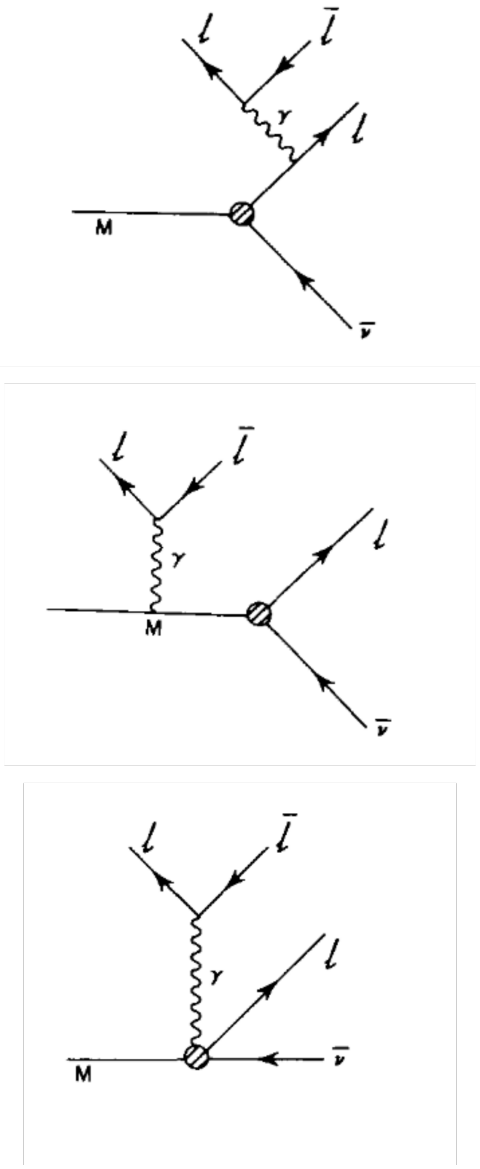

Figure 1.2: Feynmann diagrams for the Inner Bremmstrahlung (IB) and Structure Dependent (SD) contributions to $M \to l\nu ll$ decays[9].

The $K_{\mu\nu\mu\mu}$ matrix element is calculated in section 4 as a particular case of the following channel:

$$\begin{aligned} K^+(p) \to l^+(p_l)\nu_l(p_\nu)l'^+(p_1)l'^-(p_2) \\ (l,l') = (e,\mu) \text{ or } (\mu,e) \end{aligned} \tag{1.23}$$

The case $l = l'$ is more elaborate with respect to the $l \neq l'$ case because the integration over part of the phase space cannot be done analytically. The steps to derive the decay amplitude are carefully described in the article, for the purpose of this thesis is not appropriate to report them.

For the decays with three muons in the final state, the Branching Ratio, estimated taking into account only the Inner Bremsstrahlung contributions, is[10]:

$$BR_{IB}(K^+ \to \mu^+\nu_\mu\mu^+\mu^-) = 3.79 \cdot 10^{-9} \tag{1.24}$$

The order of magnitude is in agreement with another estimation

$$BR_{IB}(K^+ \to \mu^+\nu_\mu\mu^+\mu^-) \sim 3 \cdot 10^{-9} \tag{1.25}$$

reported in this article[9].

Including the effects of the form factors, that come from the SD diagram, the total Branching Ratio estimated is[10]

$$BR_{total}(K^+ \to \mu^+\nu_\mu\mu^+\mu^-) = 1.35 \cdot 10^{-8} \tag{1.26}$$

The BR is provided without an error estimation. The author reminds that there is no guarantee that the effects of higher order ChPT $O(p^6)$ can contribute significantly to the total amplitude.

1.5 $K^+ \to \mu^+\nu_\mu\mu^+\mu^-$ experimental measurements

The $K^+ \to \mu^+\nu_\mu\mu^+\mu^-$ decay has never been measured, a limit on his branching ratio was set in 1989 at Brookhaven National Laboratory (BNL) by the E787 experiment. Back at those times, physicists were looking into light Higgs boson production from kaon decays[11]; the following process:

$$K^+ \to \pi^+ H,\, H \to \mu^+\mu^- \tag{1.27}$$

was expected to be attractive. The experiment used the low-energy kaon beam produced by the BNL Alternating Gradient Synchrotron (AGS). The $K_{\mu\nu\mu\mu}$ decay was taken into account as a possible source of background. Using three candidates and an acceptance of $(2.2 \pm 0.3 \pm 0.6) \cdot 10^{-3}$ a limit was set to this process[11]:

$$BR(K^+ \to \mu^+\nu_\mu\mu^+\mu^-) < 4.1 \times 10^{-7}\ CL = 90\% \tag{1.28}$$

Up to the present day, there is not any other attempt to measure this decay; the limit reported above is the one provided by the Particle Data Group.

1.6 Dark matter at kaon factories

Lately the interest in the $K^+ \to \mu^+\nu_\mu\mu^+\mu^-$ decay has been awakened from the article "Dark matter at kaon factories"[12].

Rare kaon decays are excellent probes of new weakly-coupled light particles. If such particles X couple preferentially to muons, they can be produced in $K \to \mu\nu X$ decays, where X decays either invisibly or to a muon couple ($\mu^+\mu^-$). If X decays visibly to muons, the NA62 di-muon resonance search in

$$K \to \mu\nu X,\, X \to \mu^+\mu^- \tag{1.29}$$

processes could improve the existing constraints for both scalar and vector muonic forces, in the region $2m_\mu < m_X < m_K - m_\mu$.

The irreducible SM background for this search arises from $K^+ \to \mu^+\nu_\mu\mu^+\mu^-$ decay; the paper concludes estimating that NA62 can measure this process by analysing the already collected data.

2

NA62 Beam and detector

2.1 Introduction

The NA62 experimental apparatus is located in the CERN Prevessin site, also called North Area (NA). The NA62 detector uses the so-called decay-in-flight technique, which is innovative with respect to the one used by other kaon experiments. The E787[13] and E949[14], two rare kaon decays experiments located at Brookhaven National Laboratories in the USA, used to stop the kaons in the center of the detector and observe the decay products on the (almost) full solid angle. The decay-in-flight technique requires a fixed target to produce the kaons and a very long detector (see figure 2.1) to observe the kaon decay products that have a high kinematic boost.

In this section, the NA62 beam and the majority of the NA62 detectors are presented. Every detector is essential to study the $K^+ \to \pi^+ \nu\bar{\nu}$ decay but some of them: CHANTI, MUV1, MUV2, IRC and SAC, have been voluntarily omitted since their roles is not crucial in the DAQ system (see chapter 3) nor in the analysis presented in chapter 4. A thorough description of the missing detectors can be found in the NA62 detector paper[15], which is also one of the main sources of this chapter. The information reported in this chapter are also taken from the technical design report[16] unless otherwise specified.

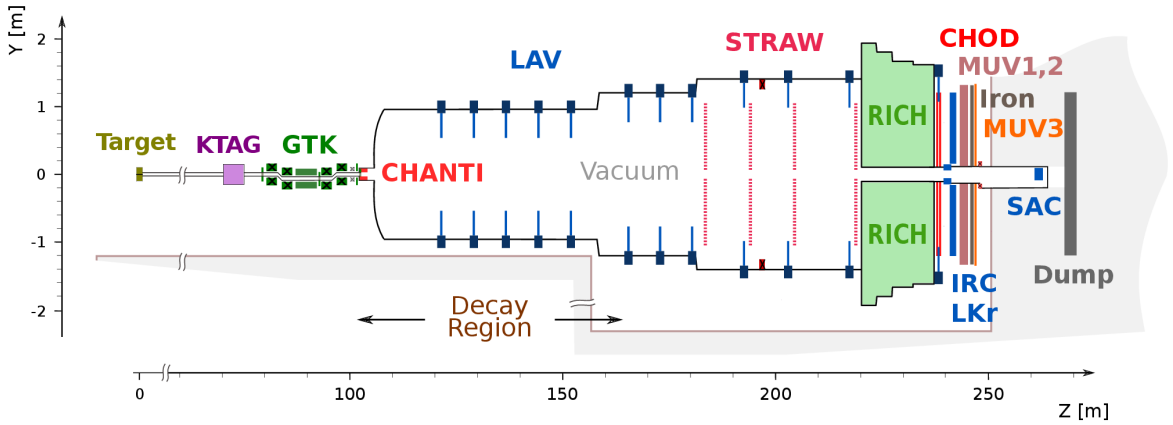

Figure 2.1: Side view of the NA62 experimental setup. Most detectors have an approximately cylindrical shape around the beam axis. An evacuated, passage surrounding the beam trajectory, allows the intense (750 MHz) flux of un-decayed beam particles to pass through, without interacting with detector material before reaching the dump.

2.1.1 High intensity kaon beam

The primary proton beam is extracted at 400 GeV/c from the CERN Super Proton Synchrotron (SPS) and directed to the T10 target via the P42 beam line. The T10 target is a 40 cm long cylinder with 2 mm of diameter made of beryllium. It is located in a tunnel connecting the SPS and the underground experimental area (see figure 2.2). The extraction of the beam last about ∼3 s and is called spill or burst. The time between two extractions depends on the SPS cycle; usually, it lasts ∼10 s but can be longer and last up to one minute. The nominal intensity of the extracted beam according to the design is $33 \cdot 10^{11}$ Proton Per Pulse (PPP). K12, the secondary beam produced after the impact with the target, contains protons, pions, and kaons. The particles rate of K12 is 750 MHz while the fraction of kaons is 6 %; as a consequence, the kaons flux is 45 MHz.

The first active elements of the high-intensity beam are three quadrupole magnets Q1, Q2 and Q3, which collect a large solid angle acceptance (±2.7 mrad horizontally and ±1.5 mrad vertically) at 75 GeV/c central momentum. A1, a front-end achromat, follows the quadrupoles and selects the beam of 75 GeV/c with a 1 % rms momentum bite. An achromat consists of four vertically-deflecting dipole magnets: the first two, produce a parallel downward displacement of the beam, while the following return the beam onto the original axis. The space between the two dipole magnet pairs is filled with TAX1 and TAX2, two motorised water-cooled beam-dump units, used to perform the momentum selection and to absorb the unwanted particles. The achromat is followed by a triplet

of quadrupoles Q4, Q5 and Q6, interspaced by three collimators C1, C2 and C3. At this point, the beam passes through three 2 m long dipole magnets with the purpose of sweep away the muons of both signs. The beam is then refocused and realigned by the two quadrupoles Q7 and Q8; C4 and C5, two collimators located downstream, absorb particles in the tails of the beam. This part is very important to satisfy the requirements of the KTAG detector (see section 2.2.1).

Following the KTAG, a doublet of weak-focusing quadrupoles (Q9, Q10) guides the beam to the beam spectrometer (see section 2.2.2). The gaps between the three beam spectrometer stations are occupied by four dipole magnets that allow to measure the momentum. The return yokes of the third and the fourth magnets, as well as a toroidally-magnetised iron collimator SCR1 deflect the muons which leave the beam in the section between the second and the third magnet of the achromat. The horizontal steering magnet (TRIM5) is used to deflect the beam toward a positive x by an angle of 1.2 mrad; this angle is compensated downstream by the spectrometer magnet MNP33 that kick the beam in the opposite direction by an angle of 3.6 mrad. Those two corrections allow to direct the beam through the central aperture of the LKr calorimeter (see section 2.2.7).

After the third beam spectrometer station, the particles travel through the 117 m long vacuum tank. The tank is made of several cylindrical parts, with different diameter, connected to each other. The tube diameter increases in the direction of the beam to cover the beam size and the divergence of the decay products. The pressure inside the tank is kept at 10^{-6} mbar, this allows to minimise the interaction of the particles with the remaining gas. The residual magnetic field inside the tube has been characterised creating a field map[17]. These measurements are used in the offline reconstruction framework to preserve the precision of the particles angle measured by the tracking system. The decay region is contained in the first 65 m of the vacuum tank starting at 102.4 m downstream of the target. A fraction of the kaons contained in the beam, about 10 %, decay in that volume.

2.2 Detectors

In this section, a subset of the NA62 detectors is briefly described. All the detector sensors produce analogue signals that need to be digitised and sampled by the coupled readout electronics. The smallest observable activity in a detector is called word. A word is a time measurement that corresponds to a leading or trailing edge of the digitised signal. A hit is the littlest information to evaluate the measured quantities that are used to take a trigger decision and at reconstruction level; it is composed of two words (one leading

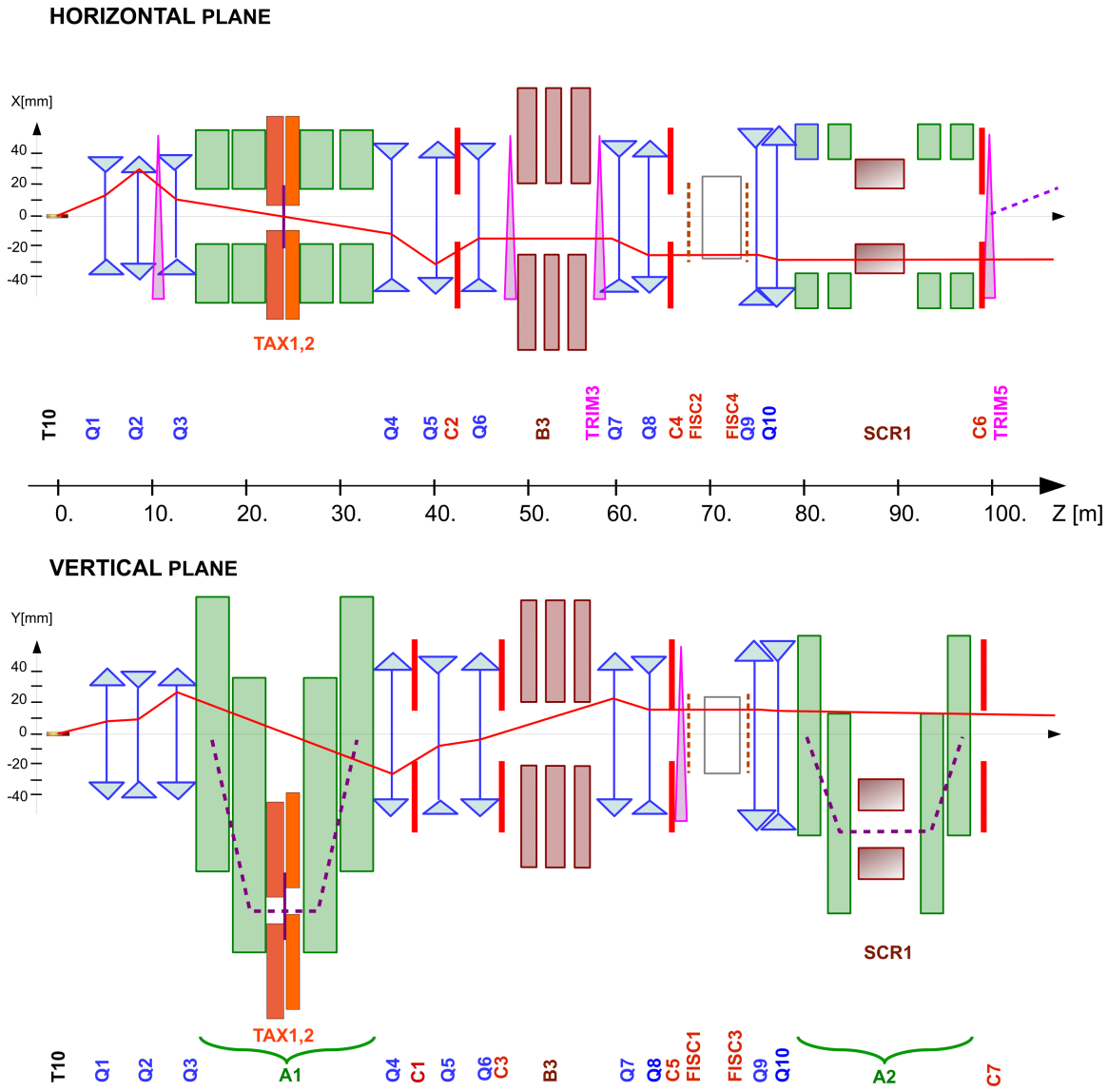

Figure 2.2: Schematic layout and optics of the high-intensity K^+ beam from the T10 target to the entrance of the decay region. In each view, the solid line corresponds to the trajectory of a particle leaving the target from the center at nominal momentum and at the angle indicated. The dashed line indicated the trajectory of an initially on-axis 75 GeV/c momentum particle.

and one trailing word).

2.2.1 Kaon tagger (KTAG)

The KTAG exploits the Cherenkov effect to identify positive kaons among all the other particles present in the beam. The detector (see figure 2.3) is a 0.94 m^3 vessel, filled with nitrogen (N_2) at 1.75 bar at room temperature. The Cherenkov light emission angle is unique, given the beam momentum and the particle mass. The light produced in the volume is reflected upstream by a spherical mirror, passes through the optical elements, the annular-shaped diaphragm and then exits the vessel through eight quartz windows. The pressure of the gas can be adjusted in such a manner to allow only the light of the wanted particle to be transmitted through the diaphragm. The advantage of this design is that only the light from kaons, a minority of the beam, contributes to the events rate. After the quartz windows, the light is reflected radially outwards into eight light boxes, also called sectors, equipped with 48 photomultipliers. The optical axis of the KTAG must be precisely aligned with the beam axis. The angular beam divergence have to be below 100 µrad in each plane, as well the alignment of the detector with the beam axis has to reach the same level of accuracy. The typical time resolution achieved by the KTAG is 70 ps.

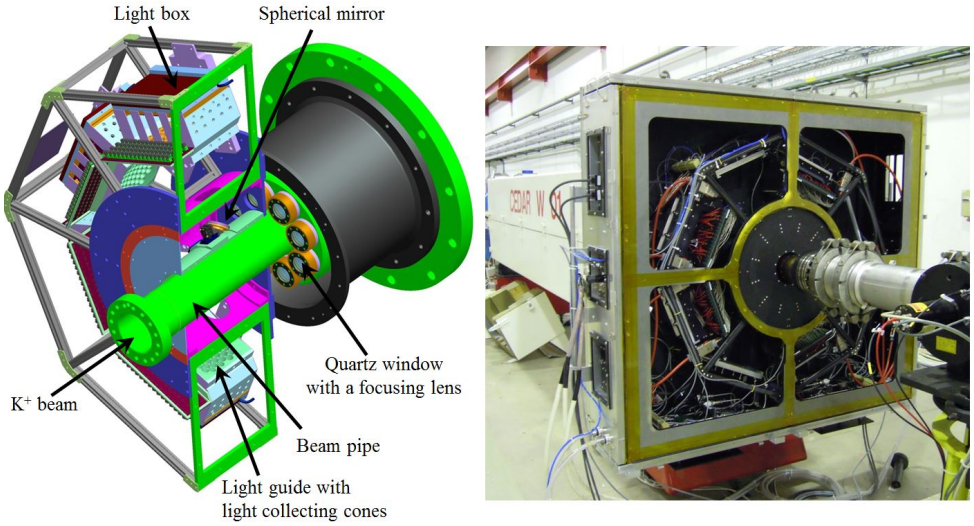

Figure 2.3: Left: drawing of the upstream part of the KTAG. Right: KTAG in the NA62 beam line during a test run in 2012, with four out of the eight sectors equipped.

2.2.2 Beam spectrometer (GTK)

The GigaTracKer (GTK) is a core part of the NA62 experiment. It is a spectrometer that provides precise measurement of the momentum, time and direction of the incoming 75 GeV/c kaon beam. Is located inside the vacuum pipe and is composed of three stations

interspersed by two couples of dipole magnets arranged as an achromat (see picture 2.4). Each station is a hybrid silicon pixel detector consisting of 18 000 pixels of $300 \times 300\,\mu m^2$ area each. The pixels are arranged in a matrix of 200×90 elements that correspond to a total area of $62.8 \times 27\,mm^2$. The sensors have been made from 200 µm thick wafer $3\,k\Omega\,cm$ resistivity silicon.

The GTK pixel sensors are located in a harsh radiation environment and, in order to minimise the ageing effects due to radiation damage, they are operated at approximately $-15\,°C$. The cooling system is composed of 150 parallel micro-channels etched on a silicon wafer. The single phase C_6F_{14} cooling liquid flows into the wafer which is directly coupled to the GTK sensor. The detector cooling has several purposes: a) it removes the heat produced by the electronics, b) keep the sensor at a stable low temperature and c) minimise the performance degradation due to leakage current induced by radiation[18]. The particles flux passing thought the sensor reach up to $2.0\,MHz/mm^2$[19] and the time resolution achieved on the track is 65 ps[19]. Considering the hit word size of 48 bit, the total bit load to be transmitted is estimated to be close to 6 Gbit/s. The radiation environment can affect the chip functioning by inducing single event upsets, for this reason, the internal logic is triplicated.

After the third GTK station, the particles travel through the vacuum tank.

2.2.3 Large Angle Veto system (LAV)

The Large Angle Veto system (LAV) is made of 12 ring-shaped photon veto stations, arranged in between the cylinder of the vacuum tank. The LAV detectors aim to identify decays with π^0 in the final state, such as $K^+ \to \pi^+\pi^0$. The LAVs provide full geometric coverage for photons emitted within the decay volume from 8.5 to 50 mrad, with respect to the beam axis. The LAV stations reuse the lead-glass blocks (see figure 2.5), formerly used in the OPAL electromagnetic calorimeter barrel[20]. The lead-glass blocks are composed by 75 % of PbO. A LAV station is made by arranging these modules around the perimeter of the sensitive volume of the experiment, with the blocks aligned radially to form an inward-facing ring. Multiple rings are used in each station in order to provide the depth required for the efficient detection of incident particles. The LAV time resolution for $1\,GeV/c$ photons is about 1 ns.

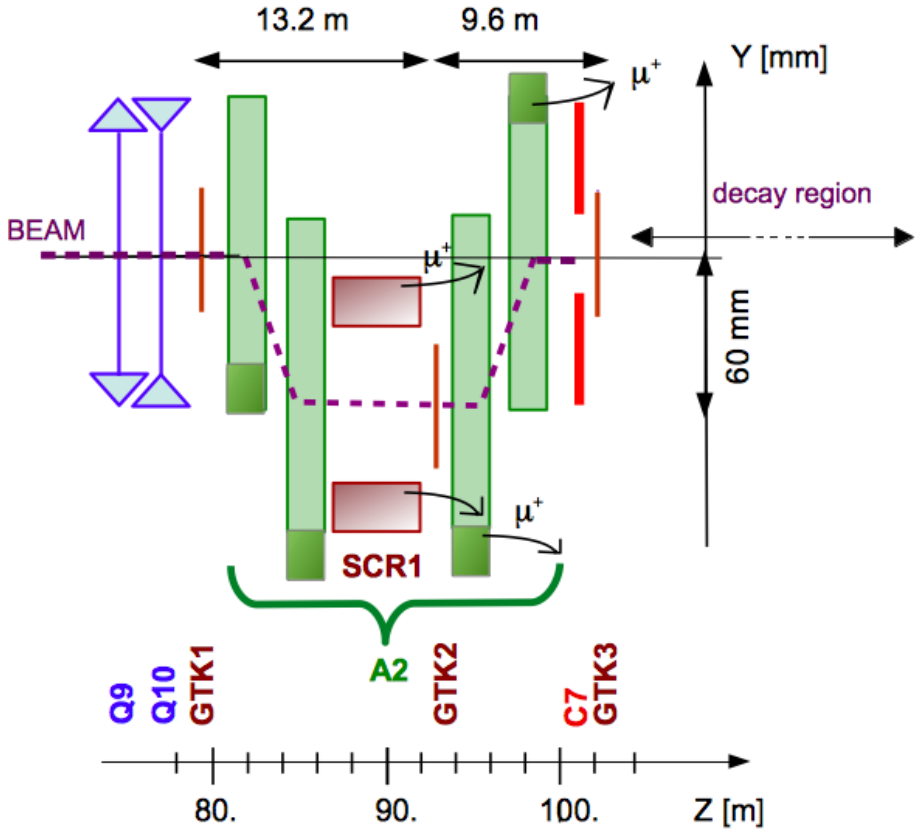

Figure 2.4: Schematic layout of the beam tracking and momentum measurement and the A2 achromat[15]. The beam is deflected vertically by 60 mm and returned to its nominal direction after the momentum measurement. Muons are swept away by the scraper (SCR1) and the return yokes of the last two C-shaped magnets of the achromat (dark shaded areas).

2.2.4 Straw spectrometer (Straw)

The Straw spectrometer measures the trajectories and the momenta of the charged particles produced by the decay of the kaon. It is made of four Straw chambers disposed over 35 m and MNP33 and a large aperture dipole magnet that provide a vertical magnetic field of 0.36 T. To minimise the multiple scattering, the Straws are directly installed into the vacuum tank and are made of light material. The smallest unit in the detector consists in a straw tube: an ultra-light drift chamber that measures 9.82 mm of diameter and 2.16 m of length. A straw tube is made of 36 µm thick polyethylene terephthalate (PET), coated with 50 nm of copper and 20 nm of gold on the inside. The inner anode wires, made of gold-plated tungsten, have a diameter of 30 µm, are tensioned at 80 g and crimped at both ends of the straw. The straws tube are arranged in planes; to achieve high detection redundancy, four layers of straw are stashed, this ensures that a track hits at least two

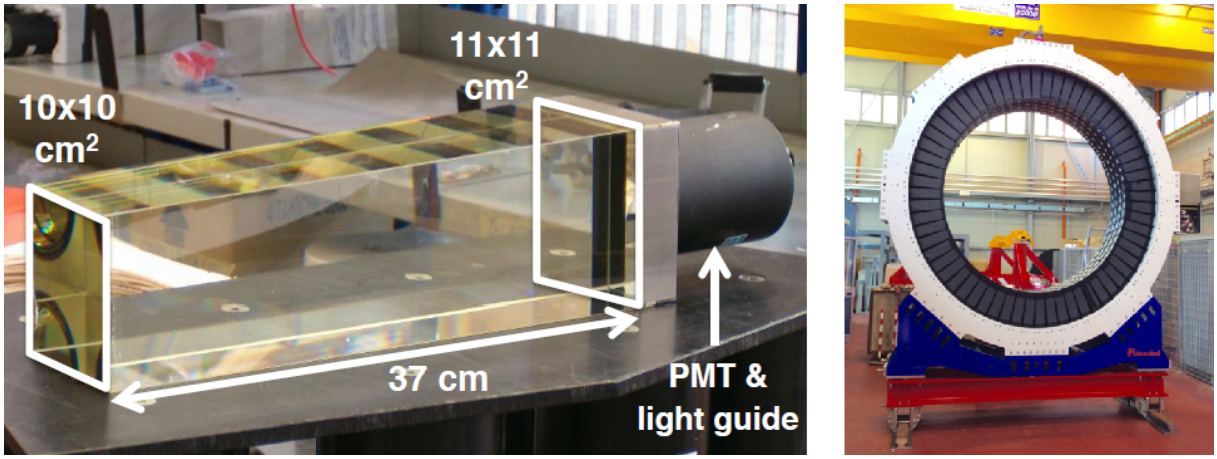

Figure 2.5: Left: One lead-glass blocks detector used in the LAV, those block have been previously used in the OPAL experiment, they were part of the electromagnetic calorimeter barrel[20]. Right: a fully assembled LAV12 station.

layers in each view. A Straw chamber is made of the overlap of 4 view planes (X, Y, U, V) tilted of 0°, 90°, 45° and −45° respectively (see figure 2.6). Some straws in the center of each view are removed intentionally to allow the passage of the un-decayed beam. The gap length in each view measures about 12 cm and, after overlaying and rotating all the chamber view, form a hole of octagonal shape. Each view is made of 448 tubes, the total amount of straw tube in the detector is 7168. For particles traversing all four chambers, the average number of straws hit is 27 and the track time resolution is found to be around 5 ns. The track momentum resolution of the Straw spectrometer is:

$$\frac{\sigma(P)}{P} = 0.30\% \oplus 0.005\% \cdot P, \tag{2.1}$$

where P is expressed in GeV/c. The tracks angular resolution decreases from 60 µrad at 10 GeV/c to 20 µrad at 50 GeV/c momentum.

2.2.5 Charged particles hodoscopes

The NA62 apparatus is equipped with two scintillation detectors called Charged Particles Hodoscopes (abbreviated as CHOD): NA48-CHOD and CHOD. The NA48-CHOD and CHOD are located respectively upstream and downstream the LAV12 station. They are operating independently at a distance of about 70 cm.

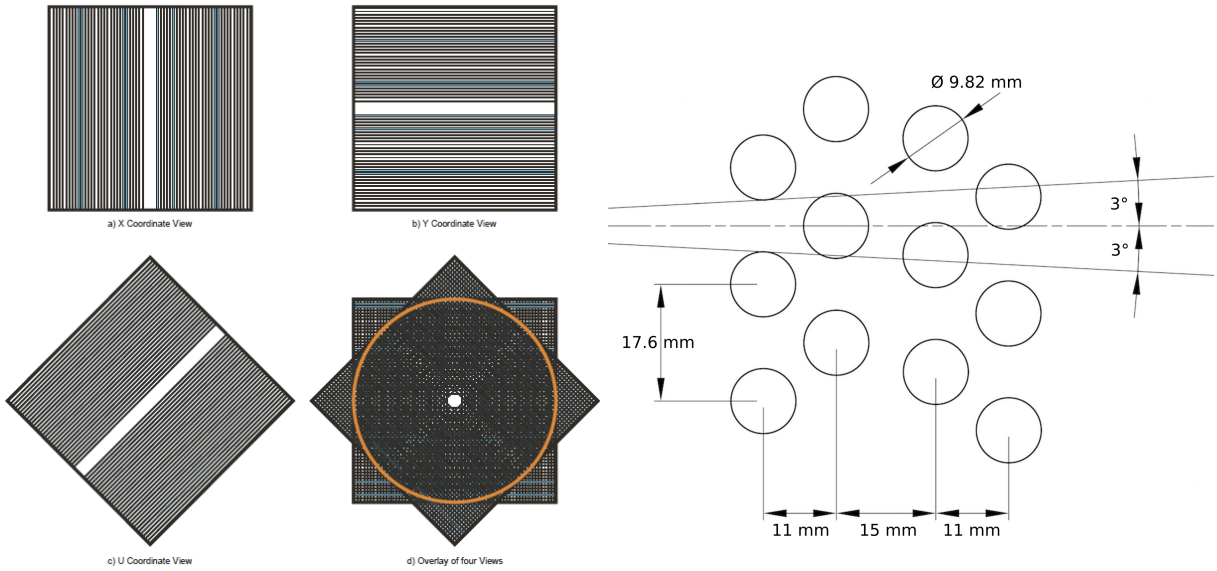

Figure 2.6: Left: one Straw chamber is composed of four views (X, Y, U, V), each view measures one coordinate. Near the middle of each view few straws are left out forming a free passage for the beam. Right: the straw geometry is based on two double layers per view with sufficient overlap to guarantee at least two straw crossing per view and per track. The 3° angle in the picture represent the angular range of tracks produced in kaon decay within the geometrical acceptance of the spectrometer.

Hodoscope (CHOD)

The CHOD active area is an array of 152 plastic scintillator tiles covering an annulus with inner (outer) radii of 140 mm (1070 mm). The light signal is collected and detected by 304 silicon photomultipliers (two for each tile). The tiles are 30 mm thick and their surface is optimised to distribute the hit rate; different groups of tiles can be selected to contribute to specific trigger requirements. The CHOD time resolution is 1 ns, a schema of the detector is reported in figure 4.1.

NA48 hodoscope (NA48-CHOD)

The NA48-CHOD hodoscope was previously used in the NA48 experiment; it consists of two layers of scintillator slabs, 64 vertical and 64 horizontal, made of BC408 plastic scintillator. The two layers provide two independent time measurements for each charged particle crossing the detector. Each slab is read out by a photomultiplier through a fishtail-shaped light guide. The 128 counters are assembled into four quadrants of 16 slabs in each plane. The slabs lengths vary from 1210 mm to 600 mm forming an octagon.

The slabs close to the beam have a width of 65 mm, because the beam flux in the central region is higher. In the outer region instead, the width is 99 mm. The layout of the NA48-CHOD is shown in figure 2.7. The NA48-CHOD track signal is defined as the coincidence of hits in one of the horizontal and vertical scintillators within a predefined time window. The signal time is the average of the two hits. The time resolution calculated using the KTAG as reference at nominal beam intensity is 210 ps.

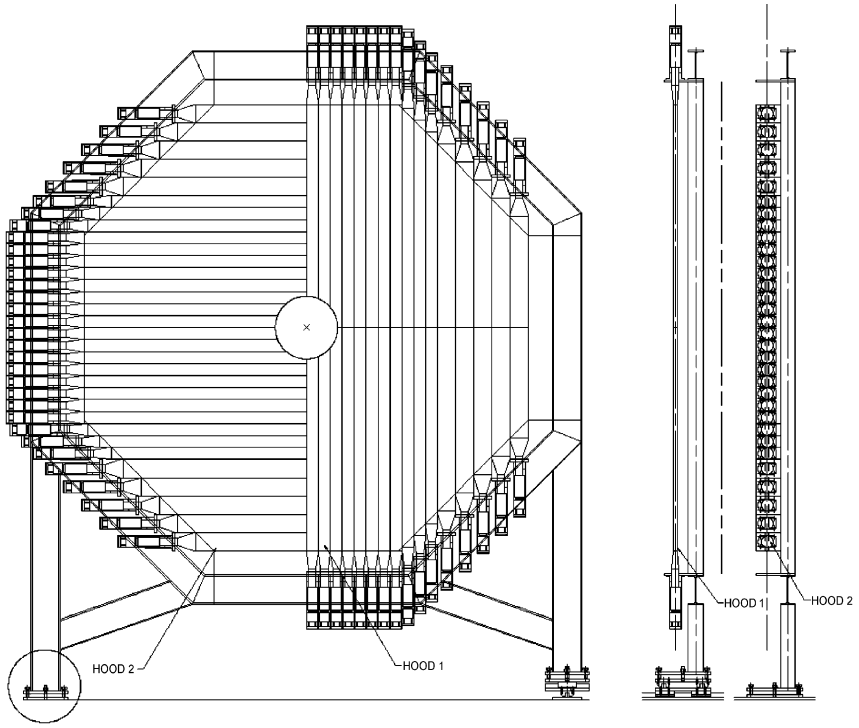

Figure 2.7: Drawing of the NA48-CHOD detector. Half sections of the horizontal and vertical planes are shown; the beam can traverse the detector thought the center.

2.2.6 Ring imaging Cherenkov counter (RICH)

The RICH detector is designed to separate pions from muons between momenta of 15 and 35 GeV/c. The RICH radiator, shown in picture 2.8, is a 17.5 m long cylindrical vessel filled with Neon gas (Ne). The vessel is made of 4 cylindrical sections with decreasing diameter and different length. The upstream part of the vessel is 4.2 m wide and hosts the two photomultipliers flanges that collect the Cherenkov light. The downstream vessel size is about 3.2 m wide and hosts the mosaic mirrors. A lightweight aluminium tube, connected to the vacuum tank, passes centrally through the vessel. A mosaic of 20 spherical mirrors is used to reflect the Cherenkov light on the two arrays of photomultipliers located upstream. The mirrors are divided into two spherical surfaces: the former with

the center of curvature pointing to the left flange and latter to the right flange. This is done to avoid the absorption of the reflected light by the beam pipe. The RICH is capable of measuring the pion crossing time with a resolution of about 100 ps, for that reason is used by the L0 Trigger Processor as reference time (see section 2.4.3).

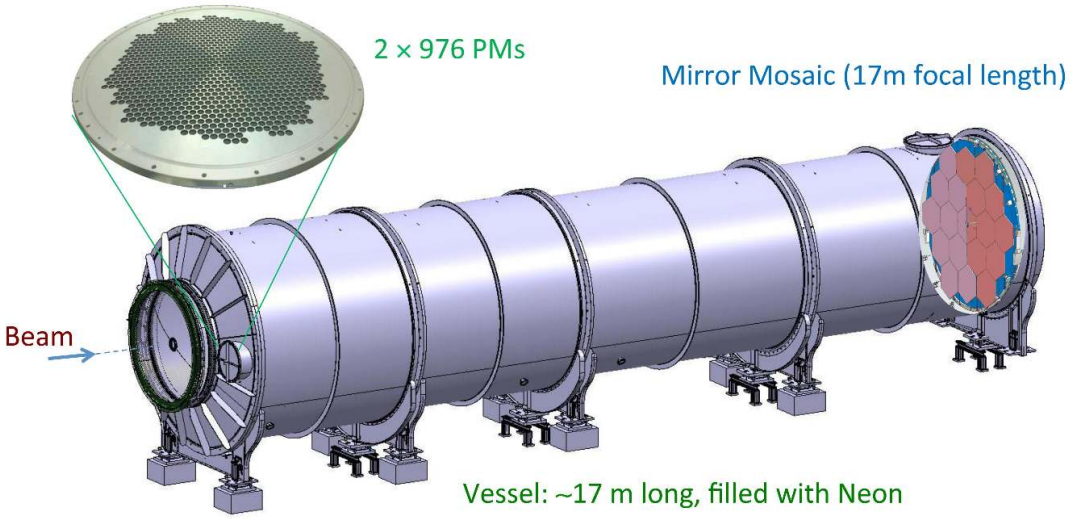

Figure 2.8: Schematic view of the RICH detector: the hadron beam enters from the left and travels throughout the length of the detector in an evacuated beam pipe. A zoom on one of the two flanges, accommodating the photomultipliers, is shown on the left; the mosaic mirror is made visible through the vessel on the right.

2.2.7 Liquid Krypton calorimeter (LKr)

The liquid Krypton calorimeter, previously used in the NA48[21] experiment, is a quasi-homogeneous calorimeter filled with 9000 L of liquid Krypton at 120 K. The shape of the calorimeter is a truncated pyramid with an octagonal base. The active octagonal front surface is inscribed into a circle of 128 cm of radius. The beam pipe (radius 8 cm)

crosses the calorimeter in the center of the octagon and allows the un-decayed beam to pass through without interact with the active volume. The LKr depth is 127 cm that corresponds to 27 X_0, this ensure the full (>99 % containment) development of electromagnetic showers. The internal sensitive area is divided into 13248 longitudinal cells with cross section of about 2 cm × 2 cm and 127 cm of length (see figure 2.9). The cells are formed by Cu−Be electrodes and have a zig-zag shape to avoid inefficiencies when a particle shower is very close to the anode. At the downstream end, the anodes are connected to the preamplifier and to the high voltage (3000 V) which produced the drift field for the ionisation. The electrode structure, together with the attached preamplifiers, is housed in a vacuum-insulated cryostat consisting of a horizontal cylinder. The electron showers produced by the particles crossing the active region are collected by the electrodes and amplified. A cluster is defined as the sum of energies in all the cells in an area around the biggest energy deposit in time and space. The position of the center of the cluster is computed using the position of the cluster cell weighted with the energy deposited in it. The spatial resolution is measured in 3 × 3 box can be parameterised as:

$$\sigma_y = \sigma_x = (\frac{4.2}{\sqrt{E[GeV]}} \oplus 0.6)\text{mm}, \tag{2.2}$$

where the first term is given by the statistical fluctuation of the particles in the shower the second is due to the size of the cell. The energy resolution for an 11 × 11 box is:

$$\frac{\sigma(E)}{E} = \frac{4.8\%}{\sqrt{E}} \oplus \frac{11\%}{E} \oplus 0.9\% \tag{2.3}$$

with the parameterisation containing the statistical term.

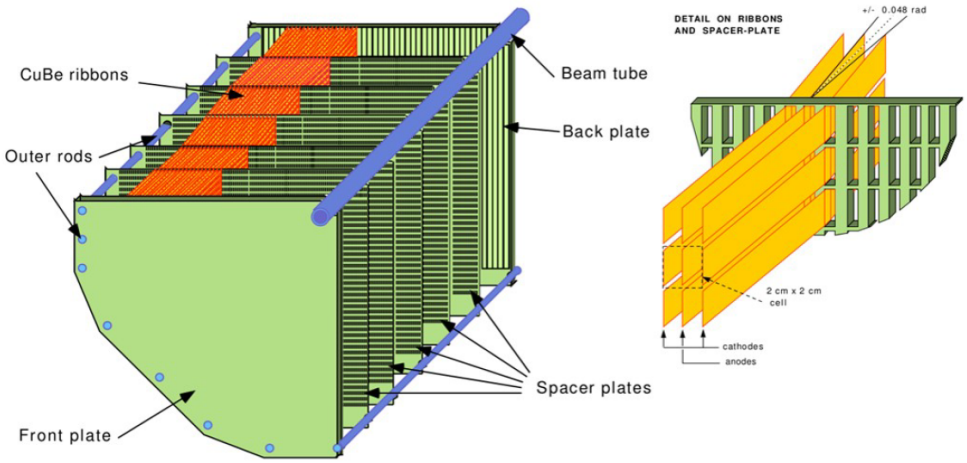

Figure 2.9: On the left a schematic of the LKr structure, one out of the four quadrants is shown. On the right: a detail of the LKr cells.

2.2.8 Muon veto (MUV3)

The fast muon veto aims at identifying muons that cross the entire calorimetric system. Its main purpose is to provide π/μ identification in addition to the RICH. It is located at 246 m downstream of the target after a 80 cm thick iron wall. The MUV3 is composed by 148 50 mm thick scintillator tiles, 140 of them with a squared regular shape of $20 \times 220\,\mathrm{mm}^2$ and 8 of them with irregular shape in order to accommodate the beam pipe in the center of the detector (see figure 4.1). The front and the laterals side of each tile are wrapped with aluminised Mylar$^{\mathrm{TM}}$ foil. The back surface instead faces a light-tight box that embeds two photomultipliers. The MUV3 identification efficiency, measured with a sample of beam halo, exceeds 99.5 % for muons with momentum above $15\,\mathrm{GeV}/c$.

2.3 Trigger and data acquisition system (TDAQ)

2.3.1 NA62 trigger system

In figure 2.10 is shown the NA62 trigger system, it is made of multiple reduction stages: the Level-0 (L0), the Level-1 (L1) and the Level-2 (L2). The two latter trigger levels are also called High Level Triggers (HLT). The L0 is a hardware trigger, based on the input of a subset of detectors: CHOD, NA48-CHOD, RICH, MUV3 and from the LKr calorimeter. The HLT are a collection of software algorithms implemented into the data acquisition code, they use the information of the following detectors: KTAG, Straw and LAV.

During the design process of NA62, the maximum L0 and L1 trigger input rates have been estimated to be $\sim$1 MHz and $\sim$100 kHz respectively. A further reduction of factor 10 should be achieved by the L2 trigger in order to have the final rate of events of the order of 10 kHz. With those values in mind, the DAQ was estimated to produce at most 3 GB per second.

The SPS beam rate is expected to be roughly uniform for few seconds along machine spill; each burst is separated from the next one by a variable time which can be as long as a minute. Inside the spill, the readout runs in a fully synchronised way and outside the spill it resets and recovers the initial state. This leads the machine spill to be the unit of data-taking in NA62.

A high-accuracy time distribution system syncs the clocks of the TDAQ components: the readout boards, dedicated subsystem like the Calo-L0 that generate the L0 trigger

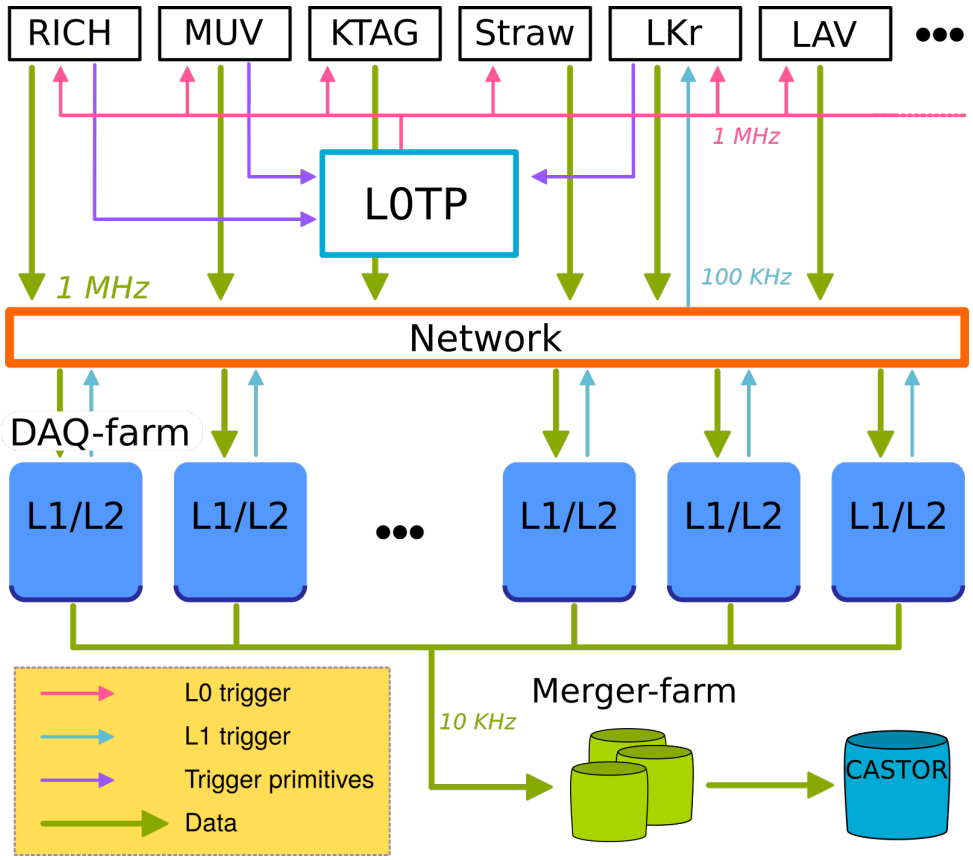

Figure 2.10: Overview of the NA62 Trigger and Data Acquisition system (TDAQ). For sake simplicity, only few detectors are displayed.

primitives, and the Level-0 Trigger Processor. In this section, the NA62 trigger system is described, a more detailed overview is reported in the NA62 low-level trigger and readout paper[22].

2.3.2 Clock and signal distribution

The Timing Trigger and Control (TTC)[23] system is a unidirectional optical fibre based transmission system. The TTC has two channels that are multiplexed, encoded using 40 MHz clock and transmitted at 160 MHz rate. One channel is used to carry the L0 trigger signal, while the other carries encoded information concerning synchronous signal and trigger types. All the synchronous elements of the NA62 TDAQ system rely on the centrally distributed TTC clock and on the start and the end of burst signals. The synchronous Start Of Burst signal (SOB) is sent to all sub-systems through the TTC link before the arrival of the beam, the signal also defines the origin of the time measurements for the current burst. An analogous synchronous End Of Burst (EOB) signal is sent in

the same way about 1 s after the end of the burst, defining the largest possible timestamp.

2.3.3 NA62 readout systems

The data exchange between readout boards and DAQ servers occurs over the User Datagram Protocol (UDP). The UDP protocol has been chosen over the Transmission Control Protocol (TCP) one due to the simplicity of implementation in the front-end FPGAs. UDP, contrary to TCP, does not implement a flow control and just needs a source and a destination port for the packets, without any acknowledgement or handshake: this eliminates all issues of communication establishment, at the cost of having to deal with data loss in case of network congestion.

The NA62 detectors are equipped with the following readout systems:

- **TEL62 readout system** The TEL62[24] is an integrated trigger and data acquisition board used by the largest part of the detectors: KTAG, LAV, NA48-CHOD, CHOD and MUV3, it is a major redesign of the TELL1[25] a board developed by LHCb. The TEL62 can host up to four high-performance TDC Boards (TDCB)[26]. Each TDCB is a mezzanine card and can digitise leading and trailing edge time of 128 channels; the measured time has 100 ps resolution. The TEL62 is equipped with 4 GbE ports used to send the primitives to L0TP and to send data to the DAQ-farm.
- **GTK readout system** The GTK readout system can be divided into two parts: the first one is located in the experimental cavern near the GTK stations, it is usually referred to as on-detector readout. The on-detector readout uses custom made ASICs called TDCPix[27], those are connected to the off-detector, which is the second part of the system. The off-detector is made of custom build modules known as GTK-RO boards, it interfaces the on-detector with the clock and the L0 trigger distribution performed with the TTC[23]. The data are temporarily stored in the TDCPix large onboard memory and then are sent, upon receiving the L0 trigger, via four 200 m long cables to the GTK-RO boards located in the server room outside the experimental area. Finally, those data are transmitted to the GTK-farm, a cluster composed of 6 servers, that is capable of communicating to the DAQ-farm.
- **Straw readout system** The Straw FE board, also know as Cover, can read out up to 16 straw tubes. A Cover hosts two analogue CARIOCA chips[28] and a Time to Digit Converter (TDC). The CARIOCA chip was originally developed by LHCb for the muon chamber, it contains pre-amplifier and shaper. The Covers are connected

to the Straw Readout Board (SRB) with Ethernet cables. The SRB collects all the data from the Cover and sent them to the DAQ-farm upon the receiving of the L0 trigger. One Straw chamber (4 views) is served by 8 SRBs.

- **Calorimeter readout system** The Calorimeter REadout Module (CREAM)[29] was specifically developed for the LKr and the others calorimeter by CAEN[30], a private company specialised in nuclear and particle instruments. The readout board has large DDR3 memories that store the entire data produced during the SPS spill; an FPGA provides the data handling and sent them out to DAQ-farm if the trigger conditions are satisfied. Each CREAM can host up to 32 analogue channels from the calorimeters. The analogue signals are shaped and digitised using the TTC distributed clock.

2.4 Level-0 trigger

The L0 trigger is meant to filter the events based on the Level-0 primitives, a fast input of a subset of detectors. The L0 trigger is fired by the L0 trigger processor a FPGA based board that takes the trigger decision. By design the maximum amount of L0 trigger that can be generated is 1 MHz.

2.4.1 Level-0 primitives

A L0 trigger primitive consists of a 32 bit data block containing the time information and an identifier that indicates which conditions are satisfied at that time. The leading and the trailing pulses produced by the TDC are received by the TEL62 and buffered in the memory. To generate the primitive the TEL62 readout board have to identify a group of hits belonging to the same event. This operation requires hits time sorting, which is an expensive operation, that scales with the number of hits. For that reason, trigger primitives are generated asynchronously, and their computation algorithm must not exceed 100 µs. The dispatching of the L0 primitives to L0TP occur over dedicated links from the TEL62 boards.

2.4.2 Calorimeter Level-0 trigger system (Cal-L0)

The CREAMs information can not be fully exploited to take a L0 trigger decision, because the bandwidth required to move those data would be too large. On the other hand, the

calorimetric information are essential to obtain the rejection power required by the NA62 at the L0 trigger level. For that reason the sums of the digitised signals are computed by the CREAM firmware every 25 ns and sent to the Cal-L0 processor. The Cal-L0 aims at identifying cluster in the electromagnetic (LKr, IRC and SAC) and hadronic (MUV1 and MUV2) calorimeters. It is composed of 37 TEL62 boards that implement those three stages to generates the trigger primitives: receives the trigger sums from the CREAM modules, reconstructs the cluster merging together trigger sums, calculates the cluster energy and possibly generates the trigger primitives.

2.4.3 The Level-0 Trigger Processor (L0TP)

The main function of the Level-0 Trigger Processor[31] (L0TP) is to acquire the trigger primitives, to sort them and to search time aligned matches.

The L0TP performs trigger primitive processing entirely in hardware; it receives UDP packets with multiple primitives via Ethernet links, unpacks and stores the data in the FPGA memory for the time alignment. The L0 Trigger Processor can receive data coming from a maximum of seven different sources and sustain a primitive rate up to 10 MHz per detector.

The time alignment is based on the information contained in the primitive data: a 25 ns timestamp and a 100 ps precision fine time. The trigger processor verifies the relevant matching condition, called trigger condition. A trigger condition defines the set of rules that must be satisfied in order to fire a trigger. If at least one trigger condition is achieved, a L0 trigger is fired to all the readout board, sending a synchronised TTC signal with 25 ns time precision. The L0 trigger and other information are packed and sent to the DAQ-farm. The L0TP, in standard data-taking conditions and beam intensity, generates about $2.3 \cdot 10^6$ triggers per burst.

2.5 The High Level Triggers (HLT)

The L1 and L2 HLT are meant to reduce the rate of events further. The algorithms are part of the data acquisition software and are described in section 3.7.

- The L1 trigger algorithms reduce the L0 data rate of a factor 10. A subset of the detector is involved in this decision.

- The L2 trigger can exploit the information of the full event; it is supposed to reduce the data rate by another 10 factor. The infrastructure to host and execute L2 algorithms is in place but no algorithm has been deployed so far.

3

The NA62 Data Acquisition system

The Data AcQuisition system (DAQ) collects, aggregates and stores the data produced by the detectors on disk. In this chapter, the NA62 Data acquisition infrastructure will be presented: in particular, some emphasis will be put on the work done in view of the 2017 data-taking. Some information reported in this chapter are taken from the paper: "The data acquisition system of the NA62 experiment at CERN"[32] written after the DAQ renovation in 2017.

3.1 NA62 DAQ infrastructure

The main components of the NA62 DAQ are the detector readout boards, the L0 trigger processor, a cluster of servers and the network that interconnects all elements (see figure 3.1). The servers and the network form the so-called DAQ infrastructure.

3.1.1 Servers hardware characteristics

The servers, hosted in a dedicated room away from the experimental cavern, are divided into two clusters: the first one is made of 30 computers, and it is called DAQ-farm, the

second it is composed of 3 servers, and it is called Merger-farm. An additional server called `na62farmdev3` is used to compile, deploy the software and host auxiliary services for the DAQ.

The division of the two clusters comes from the different functions that they have to accomplish.

A DAQ-farm node has two CPU sockets with eight double-threaded cores (2.7 GHz) and 64 GB of RAM. The cluster has a considerable amount of computational power to run the HLT, while the volatile memory is used to cache the events until the final trigger marks them to be stored or discarded. Every node of this cluster is equipped with 2 Network Interface Cards (NIC): a 10 GbE interface, used to receive data from the detectors and a 1 GbE NIC, used to send the selected data to the Merger-farm; the need for having two network interfaces will be explained in section 3.3.1. The output interface has a smaller throughput capacity because the HLT selects only the events satisfying the requested conditions.

The Merger-farm consists of storage servers, which record data on disk before transferring to the CERN permanent storage. Each of them has ∼15 TB `RAID 5` storage and 2 CPU sockets with eight double-threaded cores (2.9 GHz). The Mergers are connected to the network with a 10 GbE link and their 44 TB total storage capacity is capable of storing the raw data up to 2.5 days.

3.1.2 The network

The components of the NA62 network can be grouped into 3 units: Aggregator Switches, Core Network and DAQ-farm Aggregation Network. All the network components are configured to support Jumbo frames, the Maximum Transfer Unit (MTU) is set on 9000 B: it allows to reduce the overhead in the transmission of the packets.

The Aggregator Switches are the first element of the network chain: they collect the output sent by the detectors on the 1 GbE links and route it to the Core Network through 10 GbE optical uplinks. This part of the network, as the name indicates, acts as an aggregator for links from the readout boards and is located in the NA62 experimental cavern. The number of Aggregator Switches per detector depends on the number of sources to read.

The main task of the Core Network is to route the traffic from the detectors to the DAQ-farm cluster. Internally the Core Network is composed by five routers: four 10-40 GbE routers and one 40 GbE router (see figure 3.2). The routers are built and optimised

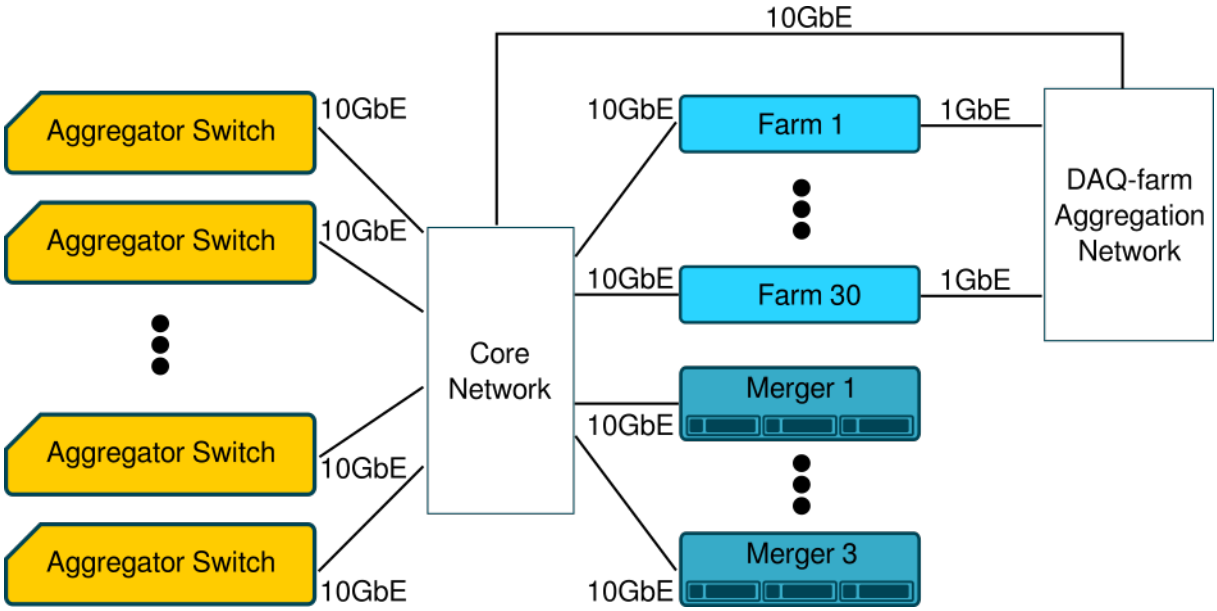

Figure 3.1: The scheme of the NA62 DAQ infrastructure. The Aggregator Switches distribute the data generated by the detectors during a burst to the entire DAQ-farm cluster. The output of the DAQ-farm is then conveyed by the DAQ-farm Aggregation Network and then routed to one of the 3 Mergers.

to accommodate enterprise network needs, which have continuous and constant traffic arriving randomly from each link. NA62 has an opposite use case: the majority of the produced traffic is unidirectional, as it comes from the detectors. Furthermore, it is also pulsed following the SPS spill cycle. For that reason the DAQ-farm and detector connections are distributed on different 10-40 GbE routers. With that configuration some traffic can already be routed locally, the rest has to be sent to the 40 GbE router and dispatched to the proper destination. The four routers are connected to the main one using a trunk link made of 6 redundant 40 GbE links. The Core Network can host up to 192×10 GbE links; it has been designed and commissioned in view of the 2017 data-taking with the help of the CERN IT network team. The core network replaced the legacy network router enhancing the network connectivity and increasing the number of spare ports.

The DAQ-farm Aggregation Network is composed of a 1-10 GbE switch that collects the output from the 30 DAQ-farm 1 GbE NICs. The 10 GbE switch link is then connected to the Core Network.

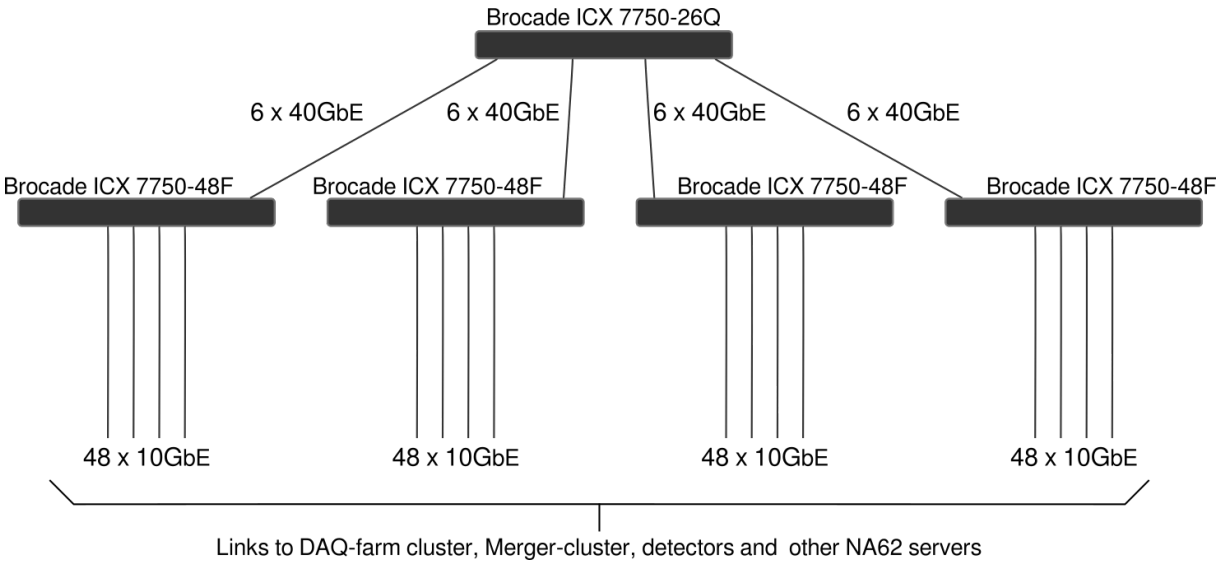

Figure 3.2: The scheme of the NA62 Core Network. The DAQ-farm and detectors are connected to the four Brocade ICX 7750-48F (10-40 GbE routers) which in turn are connected to the Brocade ICX 7750-26Q router (40 GbE)[33].

3.1.3 Configuration management

In case of software or hardware failure, a server can be excluded from the data acquisition. The events are distributed homogeneously among the servers of the DAQ-farm. Therefore, excluding a server simply requires to change the round-robin policy used for events dispatching. This allows the data-acquisition to continue while experts recover the problem. Most of the time, the issue is related to a software or kernel failure and can be recovered with a reboot, but is not always the case. Major hardware failures may need to exchange the hard drive and reinstall from scratch the Operating System (OS); such interventions can last long and be error prone if there are no well established procedures to recreate the complex runtime environments. Those issues are well-known in the IT industry that often needs to quickly scale up resources; for this reason, the OS configuration and the service provisioning have been automated with Ansible[34] for NA62. Ansible is an open-source automation tool used for IT tasks such as configuration management and application deployment. The smallest Ansible component is called role and consists of a list of tasks that have to be executed in order to deploy a service and its configuration files. It can be seen as a recipe that can be repeated every time a service needs to be deployed on a new machine. This tool, if properly used, can drastically decrease the time needed to recover a server or can be used to deploying new services at scale on the cluster. In preparation for the 2017 data-taking this tool was introduced, and along with that the server OS was migrated from SLC6[35] to CC7[36].

Operating system migration

SLC6 and CC7 are two Linux distributions based on Red Hat Enterprise Linux 6[37] and CentOS 7[38] respectively. The former was released on November 2010 and the latter in June 2014. When the NA62 data acquisition system was installed, SLC6 was the most recent Linux distribution supported by CERN. The decision of migrating the cluster to CC7 was driven by two main factors: CC7 is the natural successor of SLC6 and will be supported for a longer time; furthermore CC7 provides natively the 4.8 GCC[39] compiler series that supports the C++11[40] standard. The installation of the OS is made via the `AIMS2` client, a tool developed by CERN that allows a user to interact with the Linux Automated Installation Management System (AIMS)[41]. The client allows to register and de-register a device for the OS installation; furthermore, it is possible to specify a RedHat Kickstart file. A Kickstart file contains the answers to the questions that would normally be asked during a typical installation, allowing the system administrator to automate that process. In a Kickstart file, it is also possible to configure the partition scheme, the network configurations and the package selections.

After the OS installation, the Ansible roles with the configuration prepared for the NA62 cluster can be executed to create the correct software environment. The roles developed for the OS migration are stored in a Gitlab repository[42]. The DAQ software mostly relies on libraries provided with official software packages, but there are some other specific components that are not included. The missing components are compiled, packed into RPM[43] and distributed through a repository hosted on a virtual machine.

3.2 Online software

The online software is written in C++11[40] and it is organised in five git repositories: two of them produce the DAQ software libraries while the other generate the DAQ executables[44, 45, 46]. The DAQ libraries are:

- `na62-farm-lib`[47] It contains data format structs and shared code among the executable. All the executables depend on this library.

- `na62-trigger-algorithms`[48] It contains the HLT algorithms functions used to evaluate the L1 decision, it depends on `na62-farm-lib`.

3.2.1 Farm DIM interface software

The Farm DIM interface[44], often shortened as DIM interface, is a software that spawns the DAQ processes and is the intermediary of the communication between the process itself, the NA62 Run Control[49] and other monitoring tools. This software is deployed on all the NA62 servers and is written in C++ 11.

The name comes from the fact that it exploits the DIM library[50] for external communication. DIM stands for Distributed Information Management; it provides a transparent and distributed communication to all the processes involved in the different hosts of the DAQ system. It is used to:

- Publish information. A value published on a DIM server can be read elsewhere by a DIM client.
- Listen to Run Control commands. A DIM command interface continuously listens to messages from the Run Control: **start**, **stop**, **start of burst** and **end of burst**.

When the DIM interface receives the start command, it forks itself and initiates a new DAQ process with the parameters provided by the Run Control. While the DAQ process is running, a continuous bidirectional communication between the DIM interface and the DAQ software is established. The DIM Interface forwards the information received from the Run Control to DAQ process: **start of burst** and **end of burst**; while the process sends back statistics of the internal functioning. The latter functionality is used to study the performances of the DAQ-farm (see section 3.6).

3.3 DAQ-farm

In this section, the NA62 DAQ-farm and its software will be described.

After a positive response from L0 trigger, the data are read out from the 61 DAQ boards (see table 3.1) and sent to the DAQ-farm using the UDP protocol. All detectors must reply with some data to every L0 trigger received, thus providing a tight coupling of all readout system which allows a strict checking of data acquisition integrity. The NA62 readout packs together up to 8 events before sending a UDP packet to the DAQ-farm, this is called MEP (Multi Event Packet see image 3.3). The packing factor can be programmed at will, its value has been chosen to minimise the number of packets on the network and in the meantime to avoid IP fragmentation as much as possible. To distribute the

MEPs generated by each detector, a round-robin scheduling on all the DAQ-farm nodes is performed.

3.3.1 DAQ software

The DAQ software[45] is the software deployed on the DAQ-farm cluster, it largely exploits multi-threading and is responsible of the following functions:

- Build the L1 events
- Execute the HLT algorithms
- Send the L1 requests to complete the L2 events
- Build the L2 events
- Serialise the complete events

During the DAQ software start-up an Event Pool of pre-allocated events is initialised, capable of accommodating up to $200 \cdot 10^3$ events. An event is uniquely identified by the timestamp and the event number, associated with each L0 trigger. Each DAQ farm application, thanks to the round-robin scheduling of events, has to handle 1/30 of the MEPs generated during a burst. The DAQ-farm cluster has to be able to collect all the $\sim 2.3 \cdot 10^6$ events triggered by the L0. This corresponds to $\sim 120 \cdot 10^3$ MEPs per second per node.

To achieve the highest efficiency in collecting the UDP packets the DAQ software exploits `PF_RING`[51], a library able to access the received packets directly from the NIC. To that aim, the kernel network driver is replaced by the `PF_RING` one. `PF_RING` scatters the incoming packets on many buffers in order to deliver them to different consumers on the application side. A pool composed of 6 threads is continuously collecting the packets from the 10 GbE NIC on the six `PF_RING` buffers. Using the `PF_RING` non-standard network stack means that many operations, usually handled by the kernel, need to be managed on the application side. For that reason, the DAQ-farm software is also taking care of responding to ARP requests and reassembling packets subjected to IP fragmentation. Furthermore, the DAQ-farm software equipped with `PF_RING` has exclusive usage of the 10 GbE NIC: any other service that exploits the network connectivity must use the 1 GbE NIC.

The packets received are aggregated and delivered to a task manager which, after some checksum controls, assigns each fragment carried by the MEP to the corresponding event

in the Event Pool; this process is called event building. There are two kinds of event building:

- The L1 event building produces the so-called L1 Event composed by the L0 detectors.
- The L2 event building produces the so-called L2 Event that adds the L1 fragments to the L1 Event.

The L1 Event for a specific event is considered complete once all the L0 sources have been received by the DAQ software. At this point, the HLT algorithms can run and the trigger decision evaluated. Each algorithm exploits information from individual detector. The following HLT algorithms were deployed in 2017 and 2018 (a more detailed description is reported in section 3.7):

- The KTAG L1 algorithm uses the KTAG sector-multiplicity to positively identify a kaon and reject non-related accidental L0 triggers.
- The LAV L1 algorithm uses a hit-multiplicity cut in ten of the twelve LAV stations. It aims to reduce the background by identifying photons emitted at large angles.
- The Straw L1 algorithm reconstructs particle tracks by performing a two-dimensional Hough transform and a crude momentum evaluation. The number of tracks and the momentum are used to evaluate the trigger decision.

If the verdict from the L1 trigger algorithms is positive, the missing part of the event has to be requested from all the L1 sources. Among the L1 sources (see table 3.2), the calorimeters: LKr, MUV1 and MUV2 carry a significant fraction of the event size; for that reason, their information is fetched only when the L1 algorithm verdict is positive. The typical amount of events passing the L1 algorithms is $250 \cdot 10^3$ per burst.

The event IDs to be requested are packed together in a Multiple Request Packet (MRP) and sent via a UDP packet through the 10 GbE interface. It is important to mention that this is the only traffic directed from the DAQ-farm to the detectors. Each MRP can contain up to 100 L1 trigger requests, each of them specifies the event number and also the ip address of the server that evaluate the trigger. Each event is uniquely identified by the timestamp and the event number, associated with each L0 trigger. The L1 sources reply to the requested event number with a Sub Detector Event (SDE), which is very similar to the MEP packet. The SDE like the MEP can carry a configurable number of event, but because of some firmware limitations, only one event in shipped in a SDE payload. The data produced are collected by the Aggregator Switches which routes SDE packets

Table 3.1: Number of DAQ boards per L0 detector.

Detector	# DAQ boards
KTAG	6
CHANTI	2
LAV	12
STRAW	32
CHOD	1
RICH	5
IRC	1
MUV3	1
HASC	1
TOT	61

Table 3.2: Number of DAQ boards per L1 detector.

Detector	# DAQ boards
GTK	6
LKr	432
MUV1	6
MUV2	4
TOT	448

to the Core Network and distributes them to the DAQ node that made the L1 request. It is estimated that $23 \cdot 10^6$ UDP packets per second are generated to complete all the L2 Events. To collect UDP packets generated from L0 and L1 detectors, each DAQ-farm node has to handle a packet rate of about $\sim$900 kHz.

The acquisition process of the L1 sources in the DAQ-farm software is the same described for building the L1 Event. With the entire event, it is possible to execute the L2 algorithms to reduce the DAQ-farm output further. The software is set up to host them, although no algorithms were applied so far. The L2 algorithms that combine information from several detectors are foreseen to be deployed in the future.

Once the L2 Event is completed, it is serialised and sent to one server of the Merger cluster across a ZMQ[52] socket. The mean size of the L2 Event is about $\sim$14 kB. The event in the Event Pool is reset in order to be re-used in the next burst. The L0 UDP packets allocated in memory can not be freed right away, other event fragments carried by the MEP may be still needed to complete other events. The DAQ-farm serialised event is sent through the 1 GbE NIC with TCP packets to the DAQ-farm Aggregation Network that routes the packets back to the Core Network. The DAQ cluster receives the notification of the end of burst from the DIM interface propagating the signal from the Run Control. After six seconds from reception of this command the DAQ-farm software performs a cleanup of the Event Pool; any incomplete events is deleted. After the cleanup, the DAQ-farm cluster is ready to receive the subsequent burst.

3.3.2 End Of Burst information

The Start Of Burst (SOB) and the End Of Burst (EOB) are special events, they are the first and the last event of a burst respectively. The readout boards generate and send the SOB and the EOB packets to the DAQ-farm; the EOB payload is used to store the counters with the burst statistics of the readout boards.

The EOB can be recognised from the DAQ software because of a specific bit present in the fragment header (see image 3.3). If that bit is high, the event is considered an EOB and has particular treatment: it can be serialised and sent to the Merger even with missing event fragments. This may occur if a packet is lost or if an outage of the readout board prevents its generation. Pushing the incomplete event to the Mergers allows saving the EOB information coming from the other boards. This operation is done during the Event Pool cleanup: when the DAQ software goes through the entire Event Pool to free the memory of incomplete events; if the event is marked as EOB it is serialised. Also the DAQ-farm is supposed to save the cluster statistics into the EOB special event. Since this information is scattered on all the cluster hosts is very complicated to add them in the EOB packet which resides in one of the 30 nodes. For that reason, a different mechanism has been developed; the statistics are sent to the Farm DIM interface software which publishes them on a DIM service. In this way, the Merger can collect and store them along with the events collected. For example, the quantities saved are the number of L1 Input Events and the number of Physics Events.

3.4 Merger-farm

The Merger-farm aggregates the data from the DAQ-farm and stores them temporally until the successful transfer to the CERN tape storage. This section will describe the old and the new Merger software which has been renovated after the observation of some bugs during the 2017 data-taking. The section will conclude with the description of the CDR system that replaced the legacy software to transfer the raw data; it has been developed from scratch in view of the 2017 data-taking with the help of the IT-storage CERN team.

3.4.1 Merger software

The NA62 Merger software[46] is responsible for the following functions:

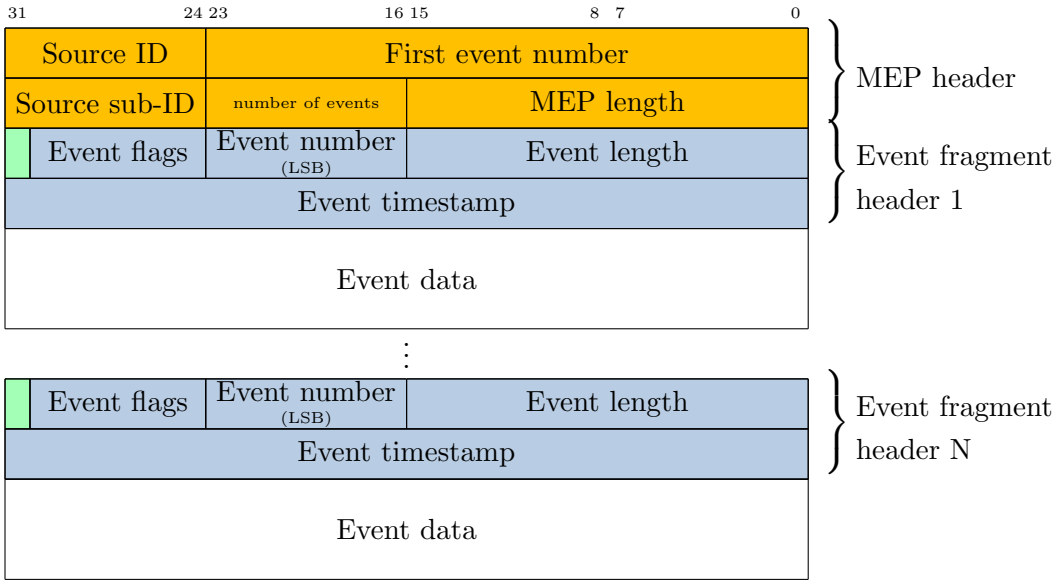

Figure 3.3: Data format of the Multiple Event Packet (MEP) used to transmit the data from the readout boards after a L0 trigger. The MEP has been designed to carry multiple event fragments, typically 8. The MEP header, coloured in orange, contains common information for all the event fragments. In light blue is highlighted the Event fragment header. The last bit of the event flags field (highlighted in green) is set to 1 if it is the special EOB event.

- Collects the events from the DAQ-farm
- Collects additional metrics from the NA62 detectors
- Writes the events and other end of burst information in a file

The Merger software is multi-threaded and written in C++11. It has been designed to be decoupled from the SPS burst periodicity and can handle more than one burst at the time.

The fully reconstructed events collected during a burst are sent from the DAQ-farm nodes to one Merger. The distribution on the three Merger machines is achieved with a round-robin algorithm; all the data collected within a burst are sent the one Merger.

The events collected from the Merger 10 GbE interface are organised in memory according to their *burst number* and *event id*. To this purpose C++ `std::map` objects are used, which are associative container that store elements formed by a combination of a key value and a mapped value[53]. The key values are used to sort and uniquely identify the elements, while the mapped values store the content associated with key. In order to handle multiple bursts concurrently a two-dimensional map is needed, the events have to be organised with

two indeces: the *burst number* and the *event id*. Internally, the elements in a map are always sorted by the key, the events arrive randomly from the DAQ cluster and the map allows to order them chronologically using the *event id*. A burst is considered complete when the size of the corresponding map does not change in an interval of 10 s. The events and the extra end of burst information, fetched from the Farm DIM interfaces, are written to file; the events are stored ordered by their *event id* thanks to the map classification.

The old Merger software was designed like a simple producer-consumer pattern (see figure 3.4). The producer thread polled the events from a ZMQ socket and placed them into a `std::map`. On the consumer side, a new thread was created for every new burst. The consumer thread job consisted of waiting for the complete collection of events and writing them to disk; the thread was destroyed after the operation accomplishment. This design

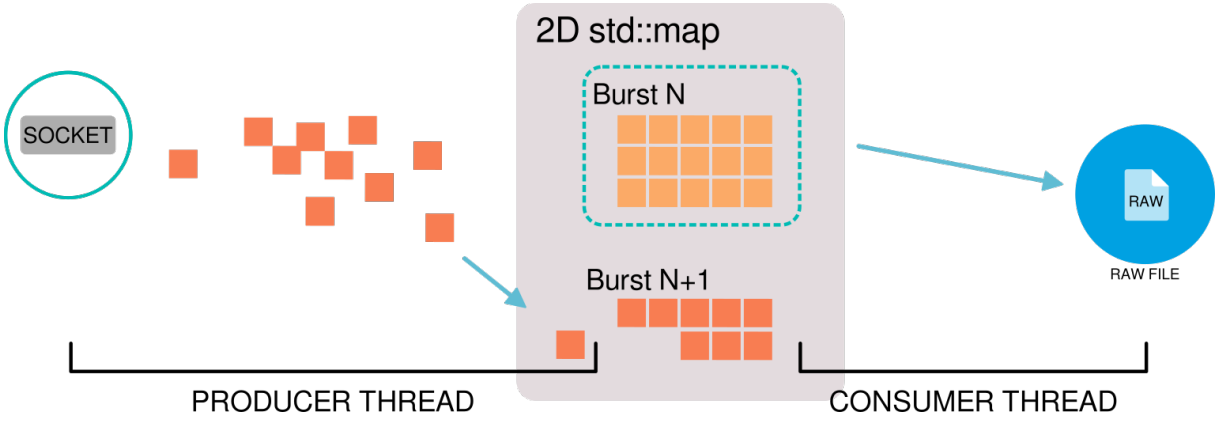

Figure 3.4: In the schema is represented the old Merger software. The main thread polls the data from the socket and places them into the map. Every burst is written on a a file by a thread generated at runtime.

had some disadvantages, and was not bug free:

- The producer was responsible for polling the data and placing them into the map. The insertion into the map may require some time and as a consequence can cause back-pressure in the network queue.
- Creating and destroying threads is an expensive operation and does not allow to have the number of threads under control.
- The `std::maps` are not thread-safe, the access to this shared structure must be controlled by a mutex. Without synchronisation, the consumer thread can write the raw file while the producer can add events to the map; this might lead to unintended interaction and behaviour of the software.

During the 2017 data-taking, several crashes of the Merger software were observed, in particular, the last point of the list above was identified as the cause.

Merger software renovation

The new Merger software was designed to fix the software crashes and to overcome all the limitations explained in the previous section. In figure 3.5, the current Merger flow schema is shown; in order to remove the dynamic thread creation a pool of thread is initialised during the software startup. The thread pool is made of a configurable amount of threads, typically four. A `std::condition_variable`[54] is used to awake one sleeping thread in the pool, the notification is done when a new burst key is created in the map. When the thread is woken up, it retrieves the corresponding burst number that has to process, and waits until the number of events in the burst map is constant. After the timer expiration, the thread locks a mutex to access that specific burst section in the maps and writes all the content into a file. During the writing operation is not possible to add events belonging to that burst, this can potentially create back-pressure in the socket queue. To avoid that, the work done by the producer thread has been divided between two threads: the main and the Merger thread. The main thread exclusively polls the ZMQ socket and pushes the data into `tbb::concurrent_queue`, while the Merger thread polls the queue and allocate the events in the correct point of the map. The new internal pipeline design has improved the Merger stability, the synchronisation in the shared map guarantees the thread-safety of the code. The thread pool is capable of writing on disk four files concurrently, in principle this allows to carry out the data-taking only with one Merger.

3.4.2 CDR system

The task of the CDR system is to transfer the raw data from the NA62 DAQ infrastructure to the CERN Advanced STORage manager[55] (CASTOR); it has been developed around the File Transfer Service (FTS)[56], a data movement service developed at CERN to transfer the data on the GRID. The CDR system is composed of:

- a book-keeping system;
- the *globus-gridftp-server*[57];
- the FTS proxy server; and

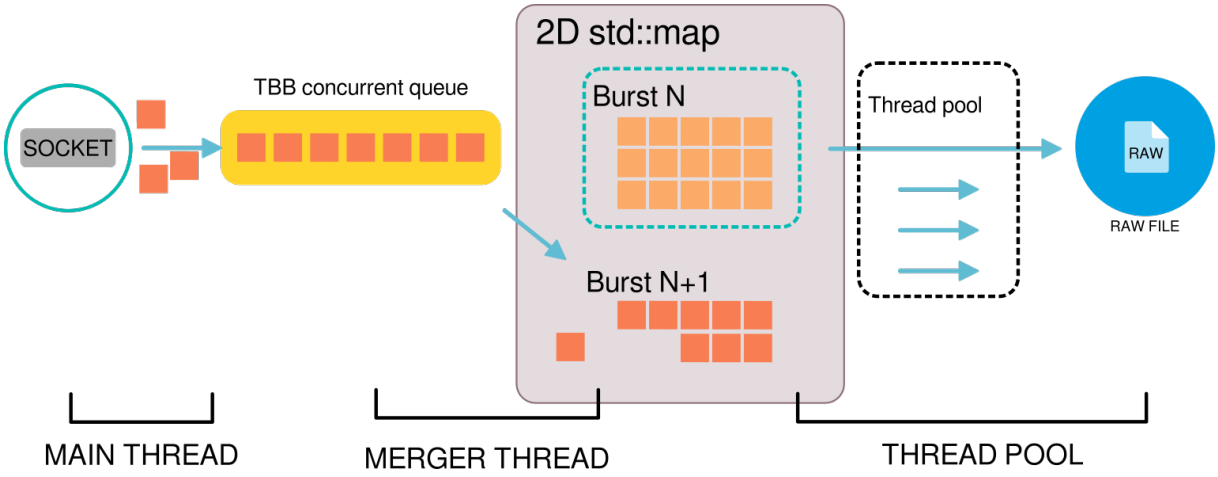

Figure 3.5: Current Merger data flow. The data coming from the socket are moved into a concurrent queue by the main thread. A second thread takes care of reading the queue and placing the data into the map. A pool of four threads waits until the burst is completed in the map and writes it to file. The thread pool is synchronised with the Merger thread and can write on disk up to four files concurrently.

- the CDR software.

The book-keeping system consists of a MariaDB[58] database and its Master-Slave replica. The Master and the Slave are hosted on two different Merger hosts. In the database are listed the files produced by the Merger software along with their transfer status: transferred, transferring and other information. The *globus-gridftp-server* is a storage element deployed on the Merger-cluster, it has access to the Merger file-system and can copy the files to CASTOR over the `gsiftp://` protocol. The *globus-gridftp-server* receives the transfer instruction from the FTS proxy (*fts3-daq.cern.ch*), a virtual machine located in the CERN data center.

The CDR software[59] is a single-threaded software written in Python, it is deployed on all the Mergers and has the following main functions:

- Continuously seek new files generated by the Merger software
- Update the file status on the database
- Submit and re-submit the file transfer requests

The CDR main loop checks continuously for new files produced by the Merger DAQ process. The files are registered in the database and then submitted for transfer. The

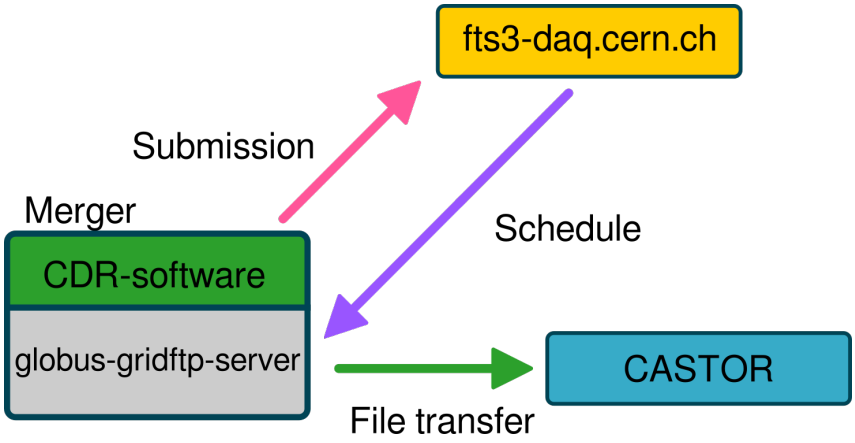

Figure 3.6: In the schema are represented: a Merger host, the FTS proxy and CASTOR. The CDR software submits the request to transfer a file to the FTS proxy; the FTS proxy notifies the *globus-gridftp-server* that transfers the file on CASTOR. Once the transfer is completed the corresponding status can be fetched by the CDR and saved in the database.

transfers are forwarded to the FTS proxy server using the Python `fts3-rest-API`[60], after that FTS takes care to instruct the storage element to move the files. The CDR continuously checks the status of the submitted files and updates the database accordingly. The FTS proxy is not only forwarding the transfer requests to the storage element, it also offers a handy web interface to monitor the transfers and the Merger-farm throughput. The figure 3.6 summarises the CDR flow from the transfer submission to the transfer on CASTOR.

All the files registered in the database must be transferred correctly to CASTOR. A raw file transfer is considered successful if the checksum of source and the destination match, this condition is checked automatically by FTS. In the event of an unsuccessful transfer, the FTS service retries it three times automatically; the file transfer is rescheduled by the CDR software in the rare cases where the automatic-retry fails.

Before deleting a file on the Merger, other two conditions must be met: the file has to be migrated on tape and 24 hours must have passed since the file was created. Waiting for the migration to tape ensures that the file is archived permanently on CASTOR, while waiting 24 hours allows the monitoring software to give a prompt feedback on the quality of the data collected. On average a file is correctly transferred in $\sim$1.5 min.

3.5 Monitoring tools

The 33 DAQ servers run about 70 software applications that continuously produce logs. The logs are stored on the machine and are rotated and deleted after 14 days; they contain information about the data acquisition such as missing detectors or events drop caused by inconsistencies in the received packets. This information is beneficial during the data-taking, it allows experts and operators to quickly assess any issues. For that reason, an error reporting system has been configured and deployed. The main goal of this system is to aggregate in real-time the logs from the 33 servers and make sure that they are available and easily accessible. There are many tools suitable for this job; after a brief survey, the choice fell on the Elastic Stack. The Elastic Stack is a group of open source products from Elastic[61] designed to help users to take data from any type of source or format and search, analyse and visualise that data in real-time. The choice was driven by two main reasons: the Elastic Stack is open-source, there is no need for licences and the CERN IT can provide the storage and visualisation components.

In the schema 3.7 the flow of the logs implemented in the NA62 DAQ is shown. On each

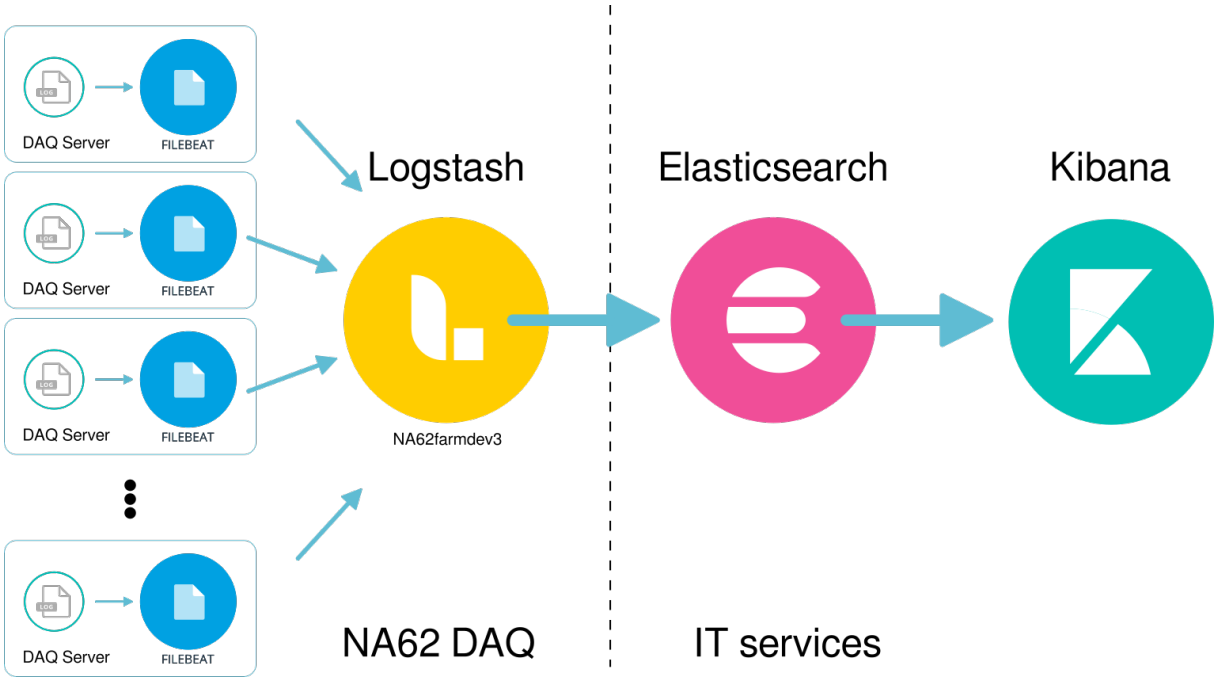

Figure 3.7: Overview of the NA62 log flow. The logs are produced on multiple servers; each log line is sent to the `na62farmdev3` host where is prepared to be saved in the database. The Elasticsearch database and the Kibana visualisation service are hosted and managed by the CERN IT.

server the Filebeat[62] daemon, a lightweight log shipper, is installed. It takes care of reading and sending the logs outside the server; it continuously checks for new log files and forwards each new line. Filebeat is capable of remembering the last lines read; it can recover in case of software interruption. The Filebeat instances send the information to `na62farmdev3`. The `na62farmdev3` server hosts the Logstash[63] daemon; the service role is to centralise and transform the data. Logstash parses every log line and extracts metadata from the raw text; the raw line, along with the metadata, is saved to the Elasticsearch[64] database. Elasticsearch is a NoSQL database and is located outside the NA62 experiment, it is provided by the CERN IT. Once the data are stored, they can be visualised with the Kibana[65] web interface (see picture 3.8). The logs produced take some seconds to be processed by Filebeat and Logstash and be viewable on Kibana. This monitoring system has been deployed during the 2017 data-taking.

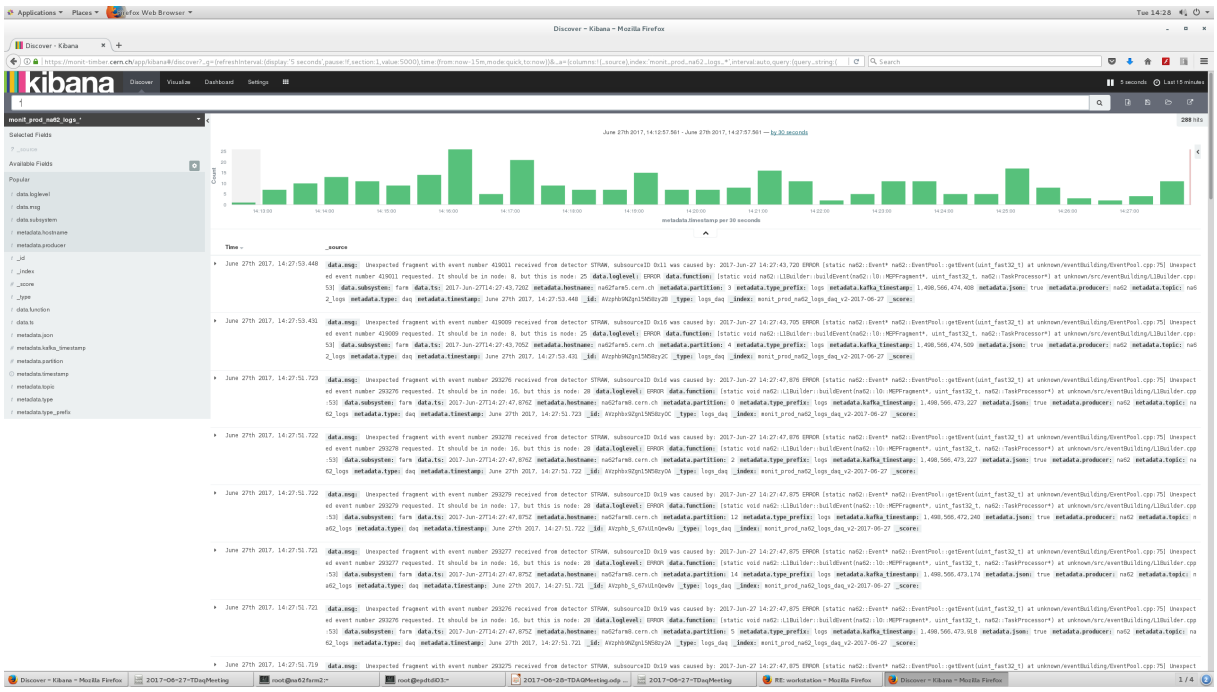

Figure 3.8: The Kibana web interface, provided by the CERN IT. The histogram on the top shows the number of logs as a function of the time while in the bottom part, the latest records collected from the NA62 cluster are displayed. The interface can be consulted by the shifters from the Run Control station.

3.6 DAQ-farm performance statistics

The performance statistics are information generated from the DAQ software (see section 3.3.1) collected during the data-taking. The information is sent to the Farm DIM interface (see section 3.2.1) that publish them on DIM services. The statistics produced the DAQ-cluster are collected burst per burst from a C++ program deployed on `na62farmdev3`. The program looks for the relevant DIM services and saves the retrieved information. The four quantities studied from the DAQ-farm cluster are listed here:

- **L0 Building Time**: It is the time taken for collecting all the 61 L0 fragments of a specific event (see table 3.1). The timer that performs this measurement starts when the first L0 fragment is associated with the corresponding event in the Event Pool; it is stopped once the last L0 fragment complete the event. This quantity is influenced by several factors: readout throughput and also network congestion.
- **L1 Processing Time**: The processing time measures the running time of the L1 algorithms. The time needed to run the algorithms depends on the computing power of the server and also on the trigger conditions associated to that event: not all the trigger conditions require to run on the entire set of L1 algorithms. The execution of the algorithms starts as soon as the last fragment is added to the event; in the same moment, the timer starts and it stops at the end of the execution of the HLT algorithms.
- **L1 Building Time**: It is analogous of the L0 Building Time for the L1 fragments (see table 3.2). The timer associated with this measurement starts upon the completion of the L1 algorithms and ends when the 448 fragments are collected. This measurement, like the L0 Building Time, depends on network congestion and the readout throughput.

In this section, the L0 Building Time, the L1 Processing Time and the L1 Building Time are studied, and their evolution as a function of the beam intensity is discussed.

Standard data-taking condition

During the 2018 data-taking the typical beam intensity provided to the NA62 detector was about $\sim$60 % of the nominal beam intensity, which corresponds to $20 \cdot 10^{11}$ protons on T10. With those conditions, the number of L0 trigger produced is $\sim 2.2 \cdot 10^6$ while the number of L1 trigger is $\sim 230 \cdot 10^3$.

The performance plots show on the x coordinate the quantity studied while on the y-axis it is plotted the evolution as a function of the time. The time corresponds to the `event_timestamp`, assigned to each event by the L0 Trigger Processor when the L0 trigger conditions are met. The `event_timestamp` is reset at the beginning of each burst. In the left figure in caption 3.9 the L0 Building Time as a function of the time is plotted. In the first second after the start of burst, a small structure is visible where the building time does not exceed the 50 ms, those events are called periodics and are generated by the L0 Trigger Processor before the arrival of the burst. The start of the physics triggers is visible after one second, where the majority of the events have a L0 Building Time between 50 ms and 150 ms. In the histogram legend the integral coincides with the number of L0 trigger produced in that burst: $\sim 2.189 \cdot 10^6$. On the left the analogous histogram for the L1 Building Time is reported. The time to collect the L1 fragments, which are ~ 7 times more, is longer and the mean value is 250 ms. In this case the integral in the legend counted $\sim 225.2 \cdot 10^3$ L1 triggers.

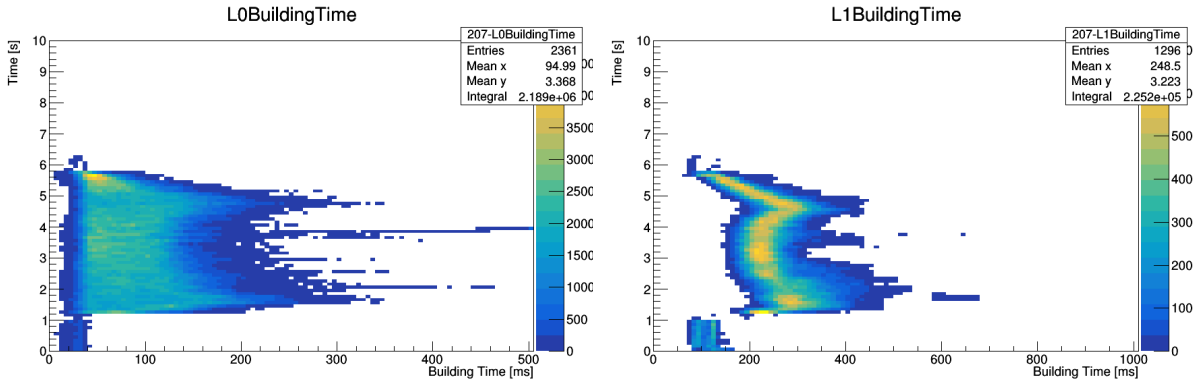

Figure 3.9: On the left the L0 Building Time as a function of the time, on the right L1 Building Time as a function of the time. The plots show the events collected in a burst during the run 9253 at standard data-taking conditions: 60 % of the nominal intensity. Between 0 and 1 s it is possible to observe the periodic triggers. On average the L0 Building Time to build $2.2 \cdot 10^6$ events is 100 ms. The average L1 building Time to build $2.2 \cdot 10^5$ events is 250 ms.

In figure 3.10 is reported the L1 Processing Time as a function of the time, please notice that is a cumulative histogram between all the trigger conditions, which can run different combinations of algorithms. Almost the totality of the events takes less that 25 µs to be processed while a small fraction can run for a much variable time between 25 µs to 1 ms.

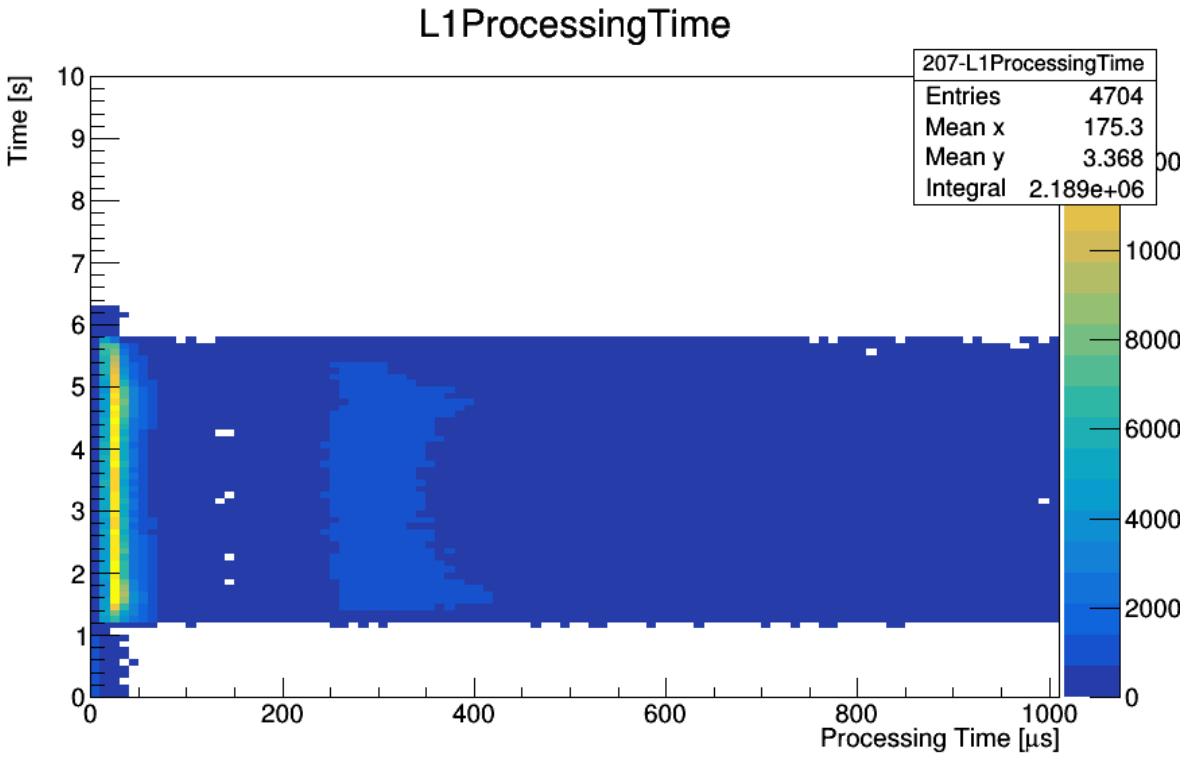

Figure 3.10: The plot shows the L1 Processing Time as a function of the time of a full burst during the run 9253 at standard data-taking conditions. From 0 to 1 s it is possible to observe the periodic triggers, the time needed to process them is very small, because any algorithms is executed on the periodic triggers. The majority of the physics event is executed in less than 200 µs, with tails up to 1 ms.

High intensity

During the high intensity tests, the beam intensity was increased up to $28 \cdot 10^{11}$ protons on T10 ($\sim$100 % of the nominal beam intensity). The corresponding number of L0 trigger was $\sim 3 \cdot 10^6$ while the number of L1 trigger was $\sim 400 \cdot 10^3$.

The study on the L1 Processing Time gives results similar to the one in the standard data-taking conditions (see figure 3.10), for that reason is not reported. Instead, the building time histograms reveal interesting insight concerning the packets collection. The figure 3.11 shows the L0 Building Time and the L1 Building Time as a function of the time. The behaviour is very different from the standard data-taking conditions. The L0 Building Time has very long tails, in particular, the last bin of the histogram, near the coloured scale, is meant to count the overflow events that exceed the histogram range (500 ms). The histogram shows that the L0 Building Time is distributed evenly between

50 to 500 µs and beyond. Concerning the L1 Building Time, the situation seems more serious: the system seems to cope with the rate of events at the beginning of the burst, but after a second the situation diverges and all the events take more than a second to be built (see overflow column in the histogram). With those conditions some data losses at L1 were observed.

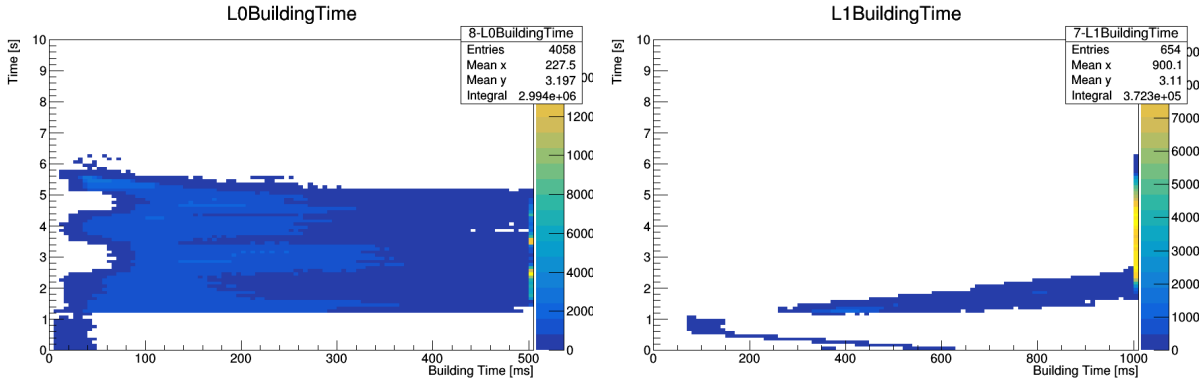

Figure 3.11: On the left the L0 Building Time as a function of the time, on the right L1 Building Time as a function of the time. The plots were made during the run 9283 at $28 \cdot 10^{11}$ pps on T10: about the 100 % of the nominal intensity. The L0 Building Time vary in a wide range that starts at about 100 ms and exceed the histogram range. A significant event fraction resides in the overflow bin column which is the last column on the x-axis. As well the L1 Building Time has overflowed.

3.7 L1 trigger algorithms

The HLT algorithms are written in C++ and run in the DAQ-farm software once the L1 event is collected. The algorithms are gathered in a dedicated repository, as described in section 3.2, which is separated from the core part of the DAQ software. An algorithm decodes the detector content and reconstructs the corresponding quantities on which the trigger decision is then calculated. The three HLT algorithms used to achieve the L1 reduction are:

- **KTAG algorithm** The KTAG L1 algorithm uses the KTAG sector-multiplicity to positively identify a kaon and reject non-related accidental L0 triggers. The selection requires a minimum of five out of eight KTAG sectors in coincidence and in time with the L0 trigger. The online time window is configurable during the algorithm start-up: and it is typically set to ± 5 ns.
- **LAV algorithm** The LAV L1 algorithm exploits a hit-multiplicity cut, aiming at further reduction of the $K^+ \to \pi^+\pi^0$ background by identifying photons emitted at large angles. The cut requires no more than two hits in ten out of the twelve LAV stations. The online time window is configurable during the algorithm start-up: and it is typically set to ± 5 ns.
- **STRAW algorithm** The Straw spectrometer algorithm is the most complicated one; for each track, the following quantities have to be reconstructed to evaluate the cut:
  - the z component of the momentum: p_z
  - the Closest Distance of Approach: CDA; which is the minimum distance between the track and the nominal beam line
  - the vertex z coordinate (Zvtx)

  To work properly, the algorithm requires all the station time offsets and channel T0s that are loaded from a configuration file. The quantities are computed with a simplified detector reconstruction that includes: clustering inside the Straw view, clustering inside the Straw chamber, point selection and finally tracks reconstruction using a two-dimensional Hough transform. The Straw algorithm can work in two different configurations: Straw$_{PNN}$ and Straw$_{exotics}$. Both configurations share the reconstruction part while different requirements are requested to evaluate the trigger response.

  The Straw$_{PNN}$ trigger aims at the rejection of multi-track events and one-track events reconstructed either outside the fiducial decay region or outside the track

momentum range required in the $K^+ \to \pi^+\nu\bar{\nu}$ event selection. The following conditions are applied:

- p_z <50 GeV/c
- CDA <200 mm
- Zvtx <180 m

To minimise the reconstruction of fake tracks, a minimal p_z of 3 GeV/c is required and the absolute values of the track slopes in the X-Z and Y-Z planes are required to be both smaller than 20 mrad. Multi-track events are identified by the reconstruction of a pair of tracks with a CDA smaller than 30 mm.

The Straw$_{exotics}$ trigger aims at positively identifying decay channels with a negative charge particle in the final state. The trigger algorithm shares the same particle track reconstruction of the Straw$_{PNN}$ trigger while adding the additional requirement of negative charge for at least one of the reconstructed tracks. The online event selection requires at least one track with:

- 3 GeV/c <p_z <100 GeV/c
- CDA <200 mm
- Zvtx <180 m, i.e upstream of STRAW chamber 1
- $SlopeY$ <20 mrad
- $SlopeX_{BeforeMagnet}$ <20 mrad
- Negative track ($slopeX_{BeforeMagnet}$ - $slopeX_{AfterMagnet}$ <0)

3.7.1 L1 packet and autopass events

A L1 trigger condition can be configured to run a combination of the algorithms presented. When the event is accepted the quantities computed with the corresponding algorithms (such as number of sectors, number of tracks), are stored with the event. They are packed in a specific container called L1 packet.

A fraction of about ∼2 % of the events not satisfying the L1 conditions is kept to evaluate the L1 trigger efficiencies. Those events are called autopass.

3.7.2 HLT integration into the reconstruction software

The HLT algorithms development has been driven by studies done on the NA62 offline framework but the code was specifically written and refined to work in the online soft-

ware environment. The possibility to study the algorithms was implemented as a special software separated from the NA62 offline software: this was not very practical and maintainable. As a consequence, the HLT algorithms are a bit detached from the main offline framework. The two main ways to monitor the online HLT performance were the autopass events, which are also used to calculate the trigger efficiencies, and the output of the algorithms stored in the L1 packet. There are some cases in which the HLT response is not saved in the L1 packet, for example:

- No HLT algorithm is executed on the data collected with the L0 minimum bias trigger (also called Control).
- A trigger condition can run a subset of the three algorithms, and as a consequence, the L1 packet will contain only the information of the algorithms executed.

Incorporating the HLT library in the offline framework allows recovering this information during the data processing.

To recover the information listed above, the integration of the HLT algorithms in the offline NA62 framework has been addressed.

There are also other reasons in support of this integration: having the HLT algorithms integrated into the reconstruction framework is very beneficial also for the development and debugging of the algorithms themselves. The response of an algorithm might be evaluated and tested directly in the reconstruction framework using the raw data. Last but not least, the trigger response can be evaluated on the events generated with the Monte Carlo; this is crucial especially for rare decay analysis where the effect of the HLT can be important for example in data over MC comparison.

In figure 3.12 is represented how the HLT algorithms have been integrated into the NA62 reconstruction software. The integration has been designed to process the raw data with the reconstruction code and with the HLT algorithms; the two outputs are then stored together in the reconstruction output file.

To achieve the integration, the two online libraries (na62-farm-lib and na62-trigger-algorithms introduced in section 3.2) are cloned along with the offline software. The online event class has been re-implemented in order to be compatible with the offline code. To do so, the references to the DAQ software components have been removed, and the possibility to load raw event fragments from the reconstruction has been introduced. The offline version of the online event class is compiled when the pre-processor variable: `-D ONLINE_HLT` is specified. That was sufficient to plug the HLT algorithm to the recon-

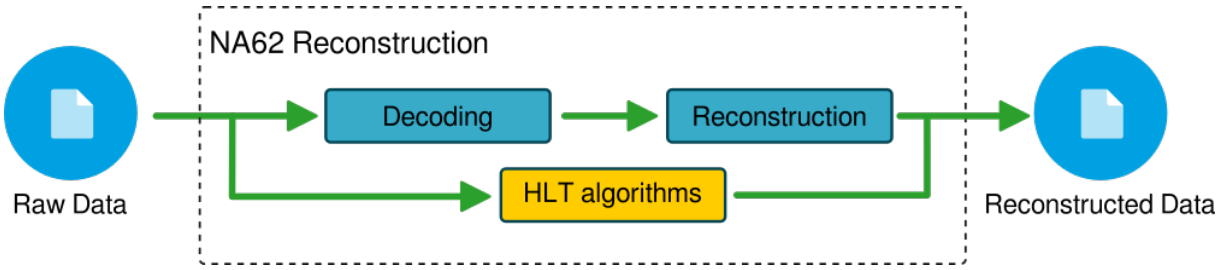

Figure 3.12: The NA62 reconstruction flow. The HLT algorithms use as input the raw data; the algorithms quantities are saved along with the NA62 reconstruction output. The HLT algorithms execute internally the decoding of the raw data.

struction input; the results produced after the execution are organised into a columnar dataset called trees along with the other quantities produced by the reconstruction. The HLT algorithms exist in two different versions: 2017 and 2018 that have been used in different data-taking periods. The algorithms version have to be taken into account while processing the raw data, otherwise it would not have been obvious to match the same results stored in the L1 packet. The capability to change the HLT version as a function of the data sample has been addressed with the usage of shared libraries loaded at runtime. For each `na62-trigger-algorithms` version is produced a shared library that stores the corresponding functions like: `hlt-2017.so`, `hlt-2018.so` etc. At runtime, the correct HLT library is loaded by the Condition Service, a reconstruction component that takes also care to provide the configuration files for the algorithms.

3.7.3 HLT validation

The integration of the algorithms was an iterative process. The execution of the HLT on the L0 minimum bias events allowed to find bugs in the algorithms decoder. After several bug-fixes, the integration of the algorithms was stable enough to process the full data sample. In this section, the information produced by the HLT library are compared with the one stored in the L1 packet. The data used in the comparison are from the sample 2018B run 8636 and refers to the PNN trigger condition. The validation plots (3.13, 3.14 and 3.15) compare the response from the re-processed HLT versus the the one stored in the L1 packet, for the following quantities:

- Number of KTAG sectors
- Number of LAV hits
- Number of Straw tracks

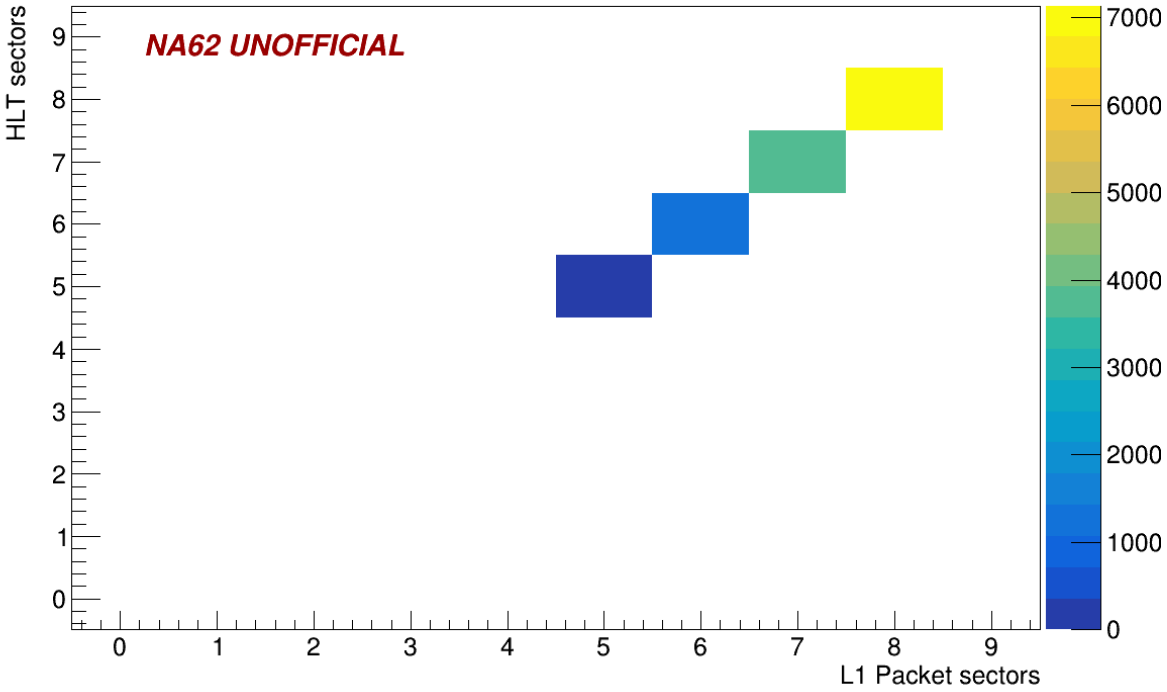

Figure 3.13: Number of KTAG sectors calculated offline with the HLT libraries versus the value stored in the L1 packet.

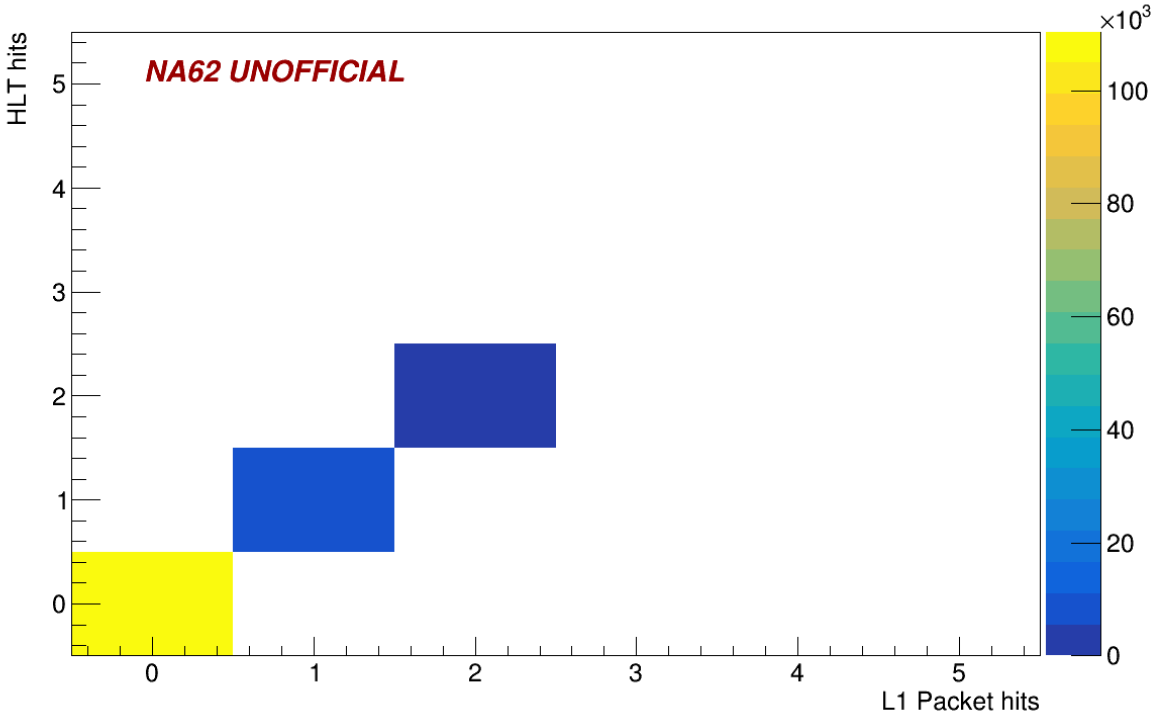

Figure 3.14: Number of LAV hits calculated offline with the HLT libraries versus the value stored in the L1 packet.

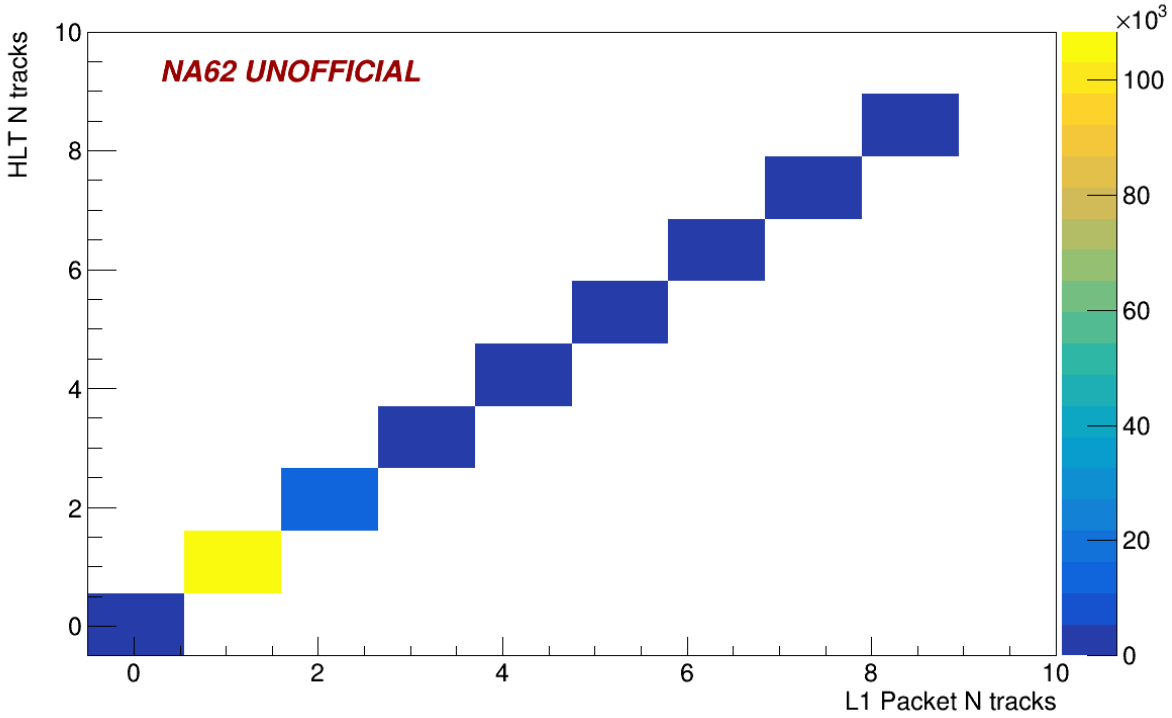

Figure 3.15: Number of Straw tracks calculated offline with the HLT libraries versus the value stored in the L1 packet.

3.8 Conclusions and prospects

This chapter described the NA62 DAQ system and the renovation done in the 2017 and 2018 data-taking.

The Core Network has been successfully commissioned and has enhanced the network connectivity, upgrading the Mergers links from 1 GbE to 10 GbE and increased the number of spare ports. The DAQ-farm cluster equipped with `PF_RING` has demonstrated to be capable of sustaining the packets rate from the experimental apparatus. During the DAQ-farm software initial development process, `PF_RING` was the only solution available to achieve high network throughput. In a possible upgrade of the DAQ-farm software, it would be interesting to explore a standard network solution in order to exploit the 10 GbE NIC for the output traffic. This will allow the removal of the DAQ-farm Aggregation Network from the DAQ chain and also to have an easier and more maintainable code.

In 2017 the L1 data reduction achieved was $\sim$9, however, the L1 rate includes also the Control trigger stream. The L1 reduction factor taking into account just the physics trigger streams is $\sim$14. With the described DAQ configuration the average data rate on disk, including the physics and control streams, was 0.8 GB/s. Due to the small event size and thanks to a high reduction factor at L1, it was possible to run the system even without the reduction from the L2 trigger. Possible upgrades of the system include the deployment of L2 trigger algorithms to further reduce the number of events written on disk.

In order to increase further the rate from the experimental apparatus, the UDP packet rate must be contained. This will be possible if the L1 detectors will group together multiple events in a single UDP packet, like the L0 detectors.

The CDR software described has replaced the previous legacy one. It has successfully transferred the files produced in 2017 and 2018 to CASTOR, 90 % of them in less than a minute. This is the first instance where the FTS technology is used to transfer the data produced from a high energy physics experiment directly on the GRID.

The integration of the HLT algorithms developed in the offline code recovered the HLT decision verdict for all the events. The integration process allowed for an in depth debugging of the HLT algorithms; thanks to that, the DAQ software is expected to be more stable in the next data-taking. The NA62 collaboration is now working to evaluate the algorithms response for Monte Carlo events reusing the same technology developed for the reconstruction.

4

$K^+ \to \mu^+\nu_\mu\mu^+\mu^-$ analysis

4.1 Introduction

The NA62 detector has been built and designed to study the $K^+ \to \pi^+\nu\bar{\nu}$ Branching Ratio. Along with this measurement, the NA62 detector has the sensitivity to study the charged kaon decays up to the $K^+ \to \pi^+\nu\bar{\nu}$.

This chapter shows the

$$K^+ \to \mu^+\nu_\mu\mu^+\mu^- \tag{4.1}$$

selection and the Branching Ratio measurement performed on the full 2017 data sample.

The $K^+ \to \mu^+\nu_\mu\mu^+\mu^-$, indicated for brevity as $K_{\mu\nu\mu\mu}$, has never been measured, a limit on his branching ratio was set in 1989 at Brookhaven National Laboratory[11]:

$$BR(K^+ \to \mu^+\nu_\mu\mu^+\mu^-) < 4.1 \times 10^{-7}\ CL = 90\% \tag{4.2}$$

4.1.1 Main background sources

The $K_{\mu\nu\mu\mu}$ fingerprint consists of a three-track event with all the tracks compatible with the muon hypothesis. Given an event of that kind, it is not obvious to assert that the

three muons are generated from the kaon rather than another process that happened in the fiducial volume.

The $K_{\pi\mu\mu}$ is a very well-known kaon decay:

$$K^+ \to \pi^+\mu^+\mu^-; \tag{4.3}$$

two out of the three decay products are muons while the third one is a pion. The pion converts into a muon neutrino couple with a very high probability[2]:

$$BR(\pi^+ \to \mu^+\nu_\mu) = (99.98770 \pm 0.00004)\%. \tag{4.4}$$

If by chance, the conversion takes place before the Straw spectrometer, a genuine muon will be tracked and detected in the MUV3. As a result, the $K_{\pi\mu\mu}$ will be recognised as a $K_{\mu\nu\mu\mu}$. This is not a sporadic occurrence, the probability for a pion to decay into a 65 m fiducial volume can be estimated as follow:

$$\begin{aligned} c \cdot \tau_{\pi^+} &= 7.8045\,\mathrm{m} \\ \gamma = \frac{\overline{E}_\pi}{m_{\pi^+}} &= \frac{24.5\,\mathrm{GeV}}{139.57\,\mathrm{MeV}} \simeq 175.5 \end{aligned} \tag{4.5}$$

Where the average pion energy $\overline{E}_\pi$ has been taken from the plot 4.20. The average length travelled by the pion: $\bar{l}$, can be calculated as follow:

$$\bar{l} = \gamma \cdot c \cdot \tau_{\pi^+} = 175.5 \cdot 7.8045\,\mathrm{m} = 1370\,\mathrm{m} \tag{4.6}$$

Assuming the probability to decay uniform we can estimate f, the fraction of pions that decays into the fiducial volume:

$$f = \frac{65\,\mathrm{m}}{1370\,\mathrm{m}} \simeq 0.05 \tag{4.7}$$

With this approximate calculation, it is possible to conclude that 5 % of $K_{\pi\mu\mu}$ has an early pion decay into the fiducial volume.

The previous example showed how an early decay can mimic the signal, in particular, hadronic and semi-leptonic kaon decays, with muons and pions in the final state, are a possible source of such background. In table 4.1 those channels are highlighted, their capability to contribute as a background event depends on the number of pions in the final state and by their Branching Ratio. Along this chapter will be shown that the $K_{3\pi}$ decay with three early decay

$$K^+ \to \pi^+\pi^+\pi^- \to \mu^+\nu_\mu\mu^+\nu_\mu\mu^-\bar{\nu}_\mu, \tag{4.8}$$

Table 4.1: List of kaon decays and their Branching Ratio relevant for the $K_{\mu\nu\mu\mu}$ analysis. The main sources of background that can mimic the $K_{\mu\nu\mu\mu}$ signal are highlighted. The $K_{\pi\mu\mu}$ Branching Ratio reported has been measured in 2011 by the NA48 collaboration[66]. It is the most precise and up-to-date result, this value will be used in the analysis.

Process	Short name	BR
$K^+ \to \mu^+\nu_\mu$	$K_{\mu 2}$	$(63.56 \pm 0.11)\%$
$K^+ \to \pi^+\pi^+\pi^-$	$K_{3\pi}$	$(5.583 \pm 0.024)\%$
$K^+ \to \pi^+\pi^-e^+\nu_e$	K_{e4}	$(4.247 \pm 0.024) \cdot 10^{-5}$
$K^+ \to \pi^+\pi^-\mu^+\nu$	$K_{\mu 4}$	$(1.4 \pm 0.9) \cdot 10^{-5}$
$K^+ \to \pi^+\mu^+\mu^-$	$K_{\pi\mu\mu}$	$(9.62 \pm 0.25) \cdot 10^{-8}$[66]
$K^+ \to e^+\nu\mu^+\mu^-$	$K_{e\nu\mu\mu}$	$(1.7 \pm 0.5) \cdot 10^{-8}$

is the most significant source of background. The $K_{\pi\mu\mu}$ Branching Ratio reported in table 4.1 has been measured in 2011 by the NA48 collaboration[66]:

$$BR(K^+ \to \pi^+\mu^+\mu^-) = (9.62 \pm 0.21_{stat.} \pm 0.11_{syst.} \pm 0.07_{ext.}) \cdot 10^{-8}, \tag{4.9}$$

it is the most updated and precise measurement done on this channel; that will be used in the analysis instead of the one reported by the Particle Data Group.

4.1.2 NA62 offline software framework

The NA62 framework[67, 68] is the software developed by the NA62 collaboration to simulate, reconstruct and analyse the data. The framework is written in several languages: C++, Fortran and Python, it also exploits well-known libraries widely adopted by the physics community: ROOT[69] and Geant4[70]. The framework is composed by three main modules: NA62MC, NA62Reco and NA62Analysis. The NA62MC provides the executables to simulate the detector and to produce the raw Monte Carlo (MC) samples. The NA62Reco produces the executable to reconstruct the raw data, this process is typically called reconstruction or data processing. The reconstruction can accept as input the raw data and the raw MC samples; the output quantities are organised into columnar dataset called trees. The NA62Analysis differs from the other two modules, it is a collection of analysers and algorithms. The structure of the analysis framework has been designed to encourage the software re-use: a collaboration member can write his analyser on top of the NA62Analysis and can exploit any analyser and algorithm present in the module at will. The NA62 software is released regularly and is labelled with a version that identifies it uniquely. Each software version is compiled centrally and it is used in Monte Carlo production and data processing.

The code developed to carry out the $K_{\mu\nu\mu\mu}$ analysis is an analyser build on top of the NA62Analysis module and it exploits many official framework functionalities that will be briefly described in section 4.2.5.

4.1.3 Monte Carlo samples

The Monte Carlo samples used in the $K_{\mu\nu\mu\mu}$ analysis are described in this section. They are used to: evaluate the signal and the normalisation channel acceptances and also to estimate the background contamination in the signal region. All the MC samples are generated centrally and are produced with different characteristics that are described in this section.

There are three main flavours of Monte Carlo:

- **Standard MC** The so-called Standard MC is the most used kind of Monte Carlo, it contains the simulations of all the NA62 detectors.
- **Fast MC** The Fast MC simulates the information of a subset of the detectors. For example, the calorimetric information about LKr, MUV1-2-3 are not generated during the production. Also the simulation of the Cherenkov radiation in KTAG is switched off. This MC flavour takes less time to be generated with respect to the Standard one, furthermore, the lack of information allows to have a smaller occupancy on the disk and to have much more events in the same amount of storage. Some of the unsimulated quantities can be recovered during the execution of the analyser using specific pre-analyser, see section 4.2.5.
- **Fast Capped MC** The Fast Capped MC, also indicated as Capped, has all the characteristics described for the Fast MC and on top of that is also biased. Those samples have been created to increase the statistics of rare processes. For example, the $K_{3\pi}$ Capped MC is exploited to evaluate the background coming from $K_{3\pi}$ early decay. This sample contains only the $K_{3\pi}$ decays with 2 or 3 pions early decay:

$$\begin{aligned} K \to 3\pi \to 2\mu + 2\nu + \pi \\ K \to 3\pi \to 3\mu + 3\nu \end{aligned} \tag{4.10}$$

  These events have a weight proportional to the probability of the process. The weight is used during the generation of the histograms; in this way, the MC samples can be normalised and plotted with Standard MC samples.

The kaons generated in the MC samples can be forced to decay in different regions of the detector:

- **Standard region** [102.425 m, 180.0 m] The Standard decay region starts after the third GTK station and ends after LAV8. The subtended volume corresponds to the vacuum tank; the events considered in any selection must have a vertex reconstructed within those limits.

- **Near-upstream region** [96.950 m, 102.425 m] The Near-upstream decay region starts after the second station of the GTK and ends after the third GTK station. A Monte Carlo produced in this region is meant to study the selection acceptance to early kaon decays. Typically the kaon is not reconstructed properly because of the missing information from the third GTK station: it is unlikely that events like that enter the selection. To normalise the Near-upstream region along with the Standard one is essential to calculate the number of kaon decays in the Standard region and then scale the number with the following factor:

$$r = \frac{\int_{NR_{x1}}^{NR_{x2}} N \cdot e^{-x/\beta\gamma c\tau} dx}{\int_{SR_{x1}}^{SR_{x2}} N \cdot e^{-x/\beta\gamma c\tau} dx} = \frac{e^{-NR_{x1}/\beta\gamma c\tau} - e^{-NR_{x2}/\beta\gamma c\tau}}{e^{-SR_{x1}/\beta\gamma c\tau} - e^{-SR_{x2}/\beta\gamma c\tau}} = 0.075 \tag{4.11}$$

  The equation shows how to calculate the number of kaon decays ratio between Near-upstream and Standard region (NR and SR indicate the borders of the regions), where a kaon of the beam has the following characteristic: $\gamma \simeq 150$ and $c\tau = 3.711$ m.

In section 4.1.1 the primary background sources have been introduced, among all of them, the one that contributes the most to the background is the $K_{3\pi}$ decay. Neither the $K_{3\pi}$ Standard MC nor the $K_{3\pi}$ Fast MC come with a sufficient statistic to observe that specific background entering in the $K_{\mu\nu\mu\mu}$ selection: it is mandatory to exploit the biased Fast Capped MC.

The list of all the MC samples relevant to the analysis and their main characteristics is shown in table 4.2. The $K_{3\pi}$ Standard MC will be used for the acceptance calculation for the normalisation channel while the $K_{3\pi}$ Fast capped MC will be needed to describe the $K_{\mu\nu\mu\mu}$ background. Those two MC samples will never be mixed because of their different nature. The choice of using the Fast MC does not come for free: the calorimetric information are not simulated, this led to exclude the LKr, MUV1 and MUV2 from the analysis; also the RICH detector can not be used for the same reason.

The main kinematic difference between the $K_{\mu\nu\mu\mu}$ and the $K_{3\pi}$ is the transverse momentum indicated with p_T. The $K_{3\pi}$ decay is kinematically close: all the particle in the final state are detected and p_T is expected to be zero. Instead, in the $K_{\mu\nu\mu\mu}$ decay a part of the energy is carried away from the neutrino, as a consequence p_T is distributed between 0 and a maximum value that depends on the energy retained by the neutrino. To achieve

Table 4.2: The MC sample used in the $K_{\mu\nu\mu\mu}$ analysis. The events in the Capped Fast samples come with a weight that represents the probability for that particular process to happen. In the table the weight is not taken into account, for that reason the quantities marked with the asterisk, have to be interpreted as the number of elements in the sample.

MC	Type	Region	MC version	Events
$K^+ \to \pi^+\pi^+\pi^-$	Standard MC	Standard	v0.11.2	$\sim 1.1 \cdot 10^6$
$K^+ \to \pi^+\pi^+\pi^-$	Standard MC	Standard	v0.11.3	$\sim 1.0 \cdot 10^6$
$K^+ \to \pi^+\pi^+\pi^-$	Standard MC	Standard	v1.0.0	$\sim 1.0 \cdot 10^6$
$K^+ \to \pi^+\pi^+\pi^-$	Standard MC	Standard	v1.0.2	$\sim 1.0 \cdot 10^6$
$K^+ \to \pi^+\pi^+\pi^-$	Standard MC	Standard	v1.0.4	$\sim 1.3 \cdot 10^6$
$K^+ \to \pi^+\pi^+\pi^-$	Standard MC	Standard	v1.1.3	$\sim 1.2 \cdot 10^6$
$K^+ \to \pi^+\pi^+\pi^-$	Standard MC	Standard	v1.1.4	$\sim 44.0 \cdot 10^6$
Total $K^+ \to \pi^+\pi^+\pi^-$				$\sim 50.6 \cdot 10^6$
$K^+ \to \pi^+\mu^+\mu^-$	Standard MC	Standard	v0.11.2	$\sim 2.6 \cdot 10^6$
$K^+ \to \pi^+\mu^+\mu^-$	Standard MC	Standard	v1.1.5	$\sim 3.8 \cdot 10^6$
Total $K^+ \to \pi^+\mu^+\mu^-$				$\sim 6.4 \cdot 10^6$
$K^+ \to \mu^+\nu\mu^+\mu^-$	Standard MC	Standard	v0.11.3	$\sim 5.4 \cdot 10^6$
$K^+ \to e^+\nu\mu^+\mu^-$	Standard MC	Standard	v0.11.3	$\sim 0.85 \cdot 10^6$
$K^+ \to \pi^+\pi^-\mu^+\nu$	Standard MC	Standard	v0.11.3	$\sim 75.8 \cdot 10^6$
$K^+ \to \pi^+\pi^+\pi^-$	Fast Capped MC	Standard	v1.0.1	$\sim 400 \cdot 10^6 *$
$K^+ \to \pi^+\pi^+\pi^-$	Fast Capped MC	Near-upstream	v1.0.3	$\sim 3400 \cdot 10^6 *$

Table 4.3: The four data samples used in the analysis shown in acquisition order. The corresponding version used in the reconstruction and the number of bursts per sample is reported.

Data Sample	Run [start, end]	Processing version	Bursts
2017D	[7615-7721]	v1.0.2	$\sim$ 22887
2017C	[7847-7873]	v1.0.3	$\sim$ 21050
2017B	[7876-8107]	v1.0.3	$\sim$ 147590
2017A	[8134-8282]	v1.0.3	$\sim$ 68804

the highest possible resolution on the transverse momentum, the GTK spectrometer must be used.

4.1.4 Data samples

The 2017 data are divided into 4 sub-samples A, B, C and D see table 4.3. In 2017A a new component has been added in the beamline, it consists of a plug inserted in the last GTK magnet. The need for this new component originates from the $K^+ \to \pi^+\nu\bar{\nu}$ analysis: the plug shields the decay region from upstream accidental tracks. Please note that this element is not simulated in the MC, and the effect on multi-track decays is negligible.

4.2 Analysis strategy

The strategy to select $K^+ \to \mu^+\nu_\mu\mu^+\mu^-$ events will be described in this section. The software written for the $K_{\mu\nu\mu\mu}$ analysis is built on top of the NA62 analysis framework and it is stored on a CERN Gitlab repository[71]. The software version used to present the results in this thesis corresponds to: `1.0.6`. The code is compiled with the NA62 software version `v1.1.6`, the latest available when the thesis went to press.

In order to compute the Branching Ratio is essential to measure the number of kaon decays in the fiducial volume using a reference channel. To this end, two independent normalisation channels are used: the $K^+ \to \pi^+\pi^+\pi^-$ and the $K^+ \to \pi^+\mu^+\mu^-$.

The signal and the normalisation selections are implemented in the same analyser code; this allows to use the initial part of the selection for all the channels, that part is named Common selection. After the common part, the events are branched into specific selections according to the characteristics of the events, those are named: $K_{3\pi}$, $K_{\pi\mu\mu}$ and $K_{\mu\nu\mu\mu}$ selections.

4.2.1 Trigger conditions

The $K_{\mu\nu\mu\mu}$ analysis relies on two different trigger conditions that are acquired simultaneously by the DAQ system. A trigger condition is made of the Level-0 and the Level-1 conditions.

4.2.2 Multi-track

The *Multi-track* trigger condition corresponds to the mask-id 5, it is meant to recognise events with more than a track. The data flagged with this condition are used to select the $K_{3\pi}$ events.

- The *Multi-track* L0 condition is

$$(\text{RICH} \times \text{Qx})/D_{Multi\text{-}track}, \tag{4.12}$$

  where $D_{Multi\text{-}track}$ is the downscale that might be different from run to run (75 or 100). The RICH condition consists in at least two hits registered within a 6.25 ns (12.5 ns for sample 2017D) window in the RICH. The Qx condition is fired by the CHOD detector and is met when two candidates are found in two diagonally-opposite CHOD quadrants (see image 4.1).

- The *Multi-track* L1 condition corresponds to

$$\text{KTAG} \times \text{Straw}_{exotics}. \tag{4.13}$$

  The KTAG and the $\text{Straw}_{exotics}$ trigger has been already described in section 3.7. There is no downscale applied at L1.

4.2.3 Di-muon

The *Di-muon* L0 condition corresponds to the mask-id 6, is made for collecting multi-track events with at least two muons in the final state. This trigger has been specifically created to trigger on the $K_{\pi\mu\mu}$ events, it is used in the $K_{\mu\nu\mu\mu}$ and the $K_{\pi\mu\mu}$ selections.

- The *Di-muon* L0 condition is

$$(\text{RICH} \times \text{Qx} \times \text{MO2})/D_{Di\text{-}muon}, \tag{4.14}$$

it can be divided in two components: the first one RICH × Qx is the same as the *Multi-track* trigger. The second part, MO2, requires at least two candidates in the outer tile of the MUV3 (see figure 4.1). The downscale $D_{Di\text{-}muon}$ depends on the run and can be 2 or 3.

- The *Di-muon* L1 condition is the same as the *Multi-track* one

$$\text{KTAG} \times \text{Straw}_{exotics}. \tag{4.15}$$

4.2.4 Control

The *Control* is a minimum-bias trigger, it is used to measure the efficiencies of L0 triggers.

- The *Control* L0 condition is

$$\text{Control}/D_{Control}. \tag{4.16}$$

The condition aims to select events with at least one charged decay product. It requires a coincidence of signals (within 6.25 ns) coming from at least one pair of overlapping vertical and horizontal slabs of the NA48-CHOD detector. The downscale $D_{Control}$ is always 400.

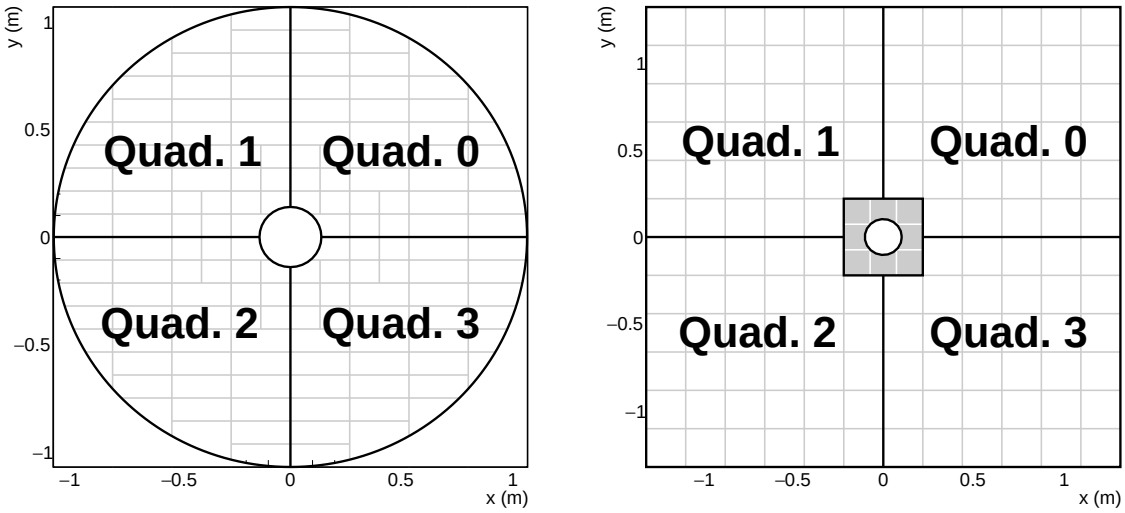

Figure 4.1: Arrangement of the quadrants of CHOD (on the left) and MUV3 (on the right) detectors. The inner region of MUV3 is indicated by the smaller, grey tiles close to the beam-pipe hole. The MO2 trigger condition exploits only the MUV3 outer tiles shown in white.

The efficiency of L1 algorithms is measured using the autopass events (about ∼2 %). When an event is marked as autopass is not rejected and it is saved regardless the response of

Table 4.4: The four $K_{\mu\nu\mu\mu}$ analysis selections and their respective trigger conditions used.

Selections	*Multi-track*	*Di-muon*	*Control*
Common selection	✓	✓	✓
$K_{\pi\mu\mu}$ selection		✓	✓
$K_{3\pi}$ selection	✓		✓
$K_{\mu\nu\mu\mu}$ selection		✓	✓

the L1 algorithms. The selections and the trigger conditions used in each selection are reported in table 4.4 .

4.2.5 Auxiliary tools

A pre-analyser is special analyser that is executed before all the analysers. The output produced by the pre-analyser can be used into an analyser code; this is very advantageous because common operations on the data can be isolated in different pre-analyser and used at will in the analysis. The pre-analysers used in the $K_{\mu\nu\mu\mu}$ selection are introduced in this section.

Fast MC Handler The Fast MC Handler pre-analyser recovers at run time some detector information not simulated in the Fast Monte Carlo samples (see section 4.1.3). The candidates of the following detectors are generated: KTAG, CHOD and MUV3. Having the MUV3 candidates is fundamental to take into account the background due to muons coming from pion early decays. For that reason the MUV3 candidates position is evaluated projecting the tracks at the MUV3 plane. This analyser is always activated while analysing Fast and Capped MC samples.

Upstream pileup generator The upstream pileup generator is a pre-analyser that generates accidental KTAG and GTK hits into the MC event. The accidental hits can generate fake GTK tracks and KTAG candidates. The random generation is based on an intensity spectrum measured from the data. This analyser is always activated while analysing any MC sample.

Downstream pileup generator The downstream pileup generator is a pre-analyser that takes care of simulating the response to pileup particles and the beam halo in the downstream detectors. The pileup components are handled separately and are propagated to

the following detectors: Straw spectrometer, CHOD, LAV, LKr and MUV3. The beam particles can decay in the 6 kaon main modes. This analyser is always activated while analysing any MC sample.

Spectrometer Vertex builder This analyser, often abbreviated as Vertex Builder, uses a Kalman filter to build the vertices starting from the reconstructed Straw tracks. The Kalman filter is implemented in a class named: VertexLSF tool. The tool is meant to fit tracks in the presence of non-uniform magnetic field[72]. The VertexLSF algorithm can be used with an arbitrary number of Straw spectrometer tracks and allows the possibility to add one GTK track to evaluate the decay vertex also exploiting the information from the beam spectrometer.

Straw spectrometer associations All the data selections that will be presented need to associate the detector candidates to a corresponding track. The association is done by specialised analysers provided by the NA62Analysis software. Each of those analysers loop over the reconstructed tracks in a given event and look for the associations that are geometrically compatible with the track projection. As a result, a track can have many associations and a candidate might be associated with more than a track. The following detector associations are obtained with the association tools: NA48-CHOD, CHOD and MUV3.

4.2.6 Data processing and filtering

The raw data collected are reconstructed centrally with the NA62Reco software. After this operation, the reconstructed events are written in different streams according to their physics characteristic. This process is called filtering and aggregates events with similar characteristics. As a consequence, it reduces the time to analyse the full data sample, it is in fact a pre-analysis that rejects events with very simple and broad cuts. The $K_{\mu\nu\mu\mu}$ selection exploits the filter: **Di-muon Three Track Vertex** abbreviated as 2MU3TV. In the 2MU3TV filter, the events are selected if the following conditions are met:

1. The event is associated with at least one of the following trigger conditions: *Control*, *Multi-track* or *Di-muon*.

2. The vertices are computed using the standard Spectrometer Vertex Builder and have to:

   (a) be composed by 3 tracks in acceptance with all the 4 Straw spectrometer chambers;

   (b) χ^2 of the fitted vertex >40;

   (c) position of the fitted vertex Z coordinate >102 m; and

   (d) vertex total momentum <90 GeV/c

3. The event flagged with the *Di-muon* trigger is requested to have at least two tracks associated with the MUV3

In general, many vertices can be found by the Vertex Builder, the event is accepted by the filter in case at least one of them satisfy the conditions above.

4.2.7 Event quality

During the reconstruction process, it is possible that the raw detector data can not be decoded, are not time-aligned or the measured efficiency is inadequate. In those cases, the reconstruction process marks that specific detector event as **bad** reconstructed. Therefore each event can have a certain amount of detectors not properly reconstructed. The default behaviour of an analyser consists of skipping any event that does not meet all the quality standard. In the $K_{\mu\nu\mu\mu}$ analysis, only a subset of the detectors is used: KTAG, GTK, Straw, NA48-CHOD, CHOD and MUV3. This means that the bad events associated with the excluded detectors can be used to increase the events statistic without affecting the quality.

The following detectors must satisfy all the data quality standards:

- **KTAG** used for identifying the kaon
- **GTK** used to determine momentum and direction of the kaon
- **Straw** used to determine the downstream tracks momentum and position
- **CHOD** used to evaluate the downstream tracks times and position
- **NA48-CHOD** used to evaluate downstream tracks time and position
- **MUV3** used for identify muons

4.3 Common event selection

The Common selection is the analysis part shared by signal and normalisations. It is intended to select events with three charged particles and to match them with kaon parent. Every event has a L0 reference time associated: $t_{trigger}$, provided by the RICH detector. The selection starts using the information from the downstream detectors: Straw, CHOD, NA48-CHOD and MUV3; which are the one meant to detect the kaon decay products. The information coming from the downstream detectors constitute the so-called **downstream event**. After a successful downstream event reconstruction, it is possible to continue the selection and analyse the information of the upstream detectors: KTAG and GTK. Those detectors provide the information of the kaon and constitute the **upstream event**. The upstream and the downstream event together reconstruct all the kinematic quantities to carry out the specialised channel selections. In this section, the selection steps are reported.

4.3.1 Three tracks vertex

The particles trajectories and charges are determined by the Straw spectrometer. The first part of the event selection consists of selecting the suitable vertices reconstructed into the Standard decay region. The vertex quantities are provided by the Spectrometer Vertex Builder (see section 4.2.5). The following characteristics are requested:

1. the vertex has to be composed by 3 tracks;
2. the sum over the tracks charges must be equal to 1; and
3. the vertex Z coordinate must be within 105.0 m and 180.0 m

Afterwards, the tracks are required to lay inside the acceptance of the 4 Straw chambers, NA48-CHOD, CHOD and MUV3. Each track also has to satisfy the following characteristics:

1. the track momentum must be within 10 GeV/c and 60 GeV/c; finally
2. the χ^2 of the track fit have to be smaller than 25.

4.3.2 Downstream Time evaluation

In order to match the GTK candidate that generated the decay, a precise event time evaluation is required. The charged hodoscope detectors, NA48-CHOD and CHOD, provide the timing information with a better resolution compared to the Straw spectrometer. For that reason, those detectors are used to provide the Downstream Time, which is calculated as follow:

$$t_{Downstream} = \frac{\sum_{n=1}^{3} track\text{-}time_n}{3} \tag{4.17}$$

The Downstream Time is calculated as the average of the candidates found in association with a track in CHOD or NA48-CHOD. To find the corresponding candidates two analysers are used: Spectrometer CHOD association and Spectrometer NA48-CHOD association (see section 4.2.5). They provide a list of candidates compatible with the track, the closest in time, respect to the trigger time, is selected.

To find the three candidates, three different approaches can be used in the analyser (see also figure 4.2):

- **CHOD and NA48-CHOD**. In this mode, each track has to be associated with a NA48-CHOD and CHOD candidate. The Downstream Time is then evaluated using the mean of the three NA48-CHOD candidates. The NA48-CHOD detector gives the most precise time information, but at reconstruction level, especially for multi-track events, the candidate position can be wrong, this is due to the internal structure of the NA48-CHOD. For that reason, the NA48-CHOD is used in conjunction with the CHOD. The CHOD has a bigger time resolution but is not suffering the misreconstruction issue. This configuration allows the best possible time precision but will also reduce the overall acceptance because of the further request of the CHOD to confirm the NA48-CHOD candidates.
- **Only CHOD**. This mode locks out the NA48-CHOD and involves the use of CHOD only. The Downstream Time is then evaluated using the mean of the three CHOD candidates. This configuration achieves a less precise time resolution but has the benefit to increase the acceptance.
- **CHOD or NA48-CHOD**. Choosing this configuration, each track must find an association in CHOD or NA48-CHOD. **This option gives the maximum acceptance and it is used by default in the analyser**.

The Downstream Time is requested to lay inside a 10 ns window around $t_{trigger}$, otherwise it is rejected.

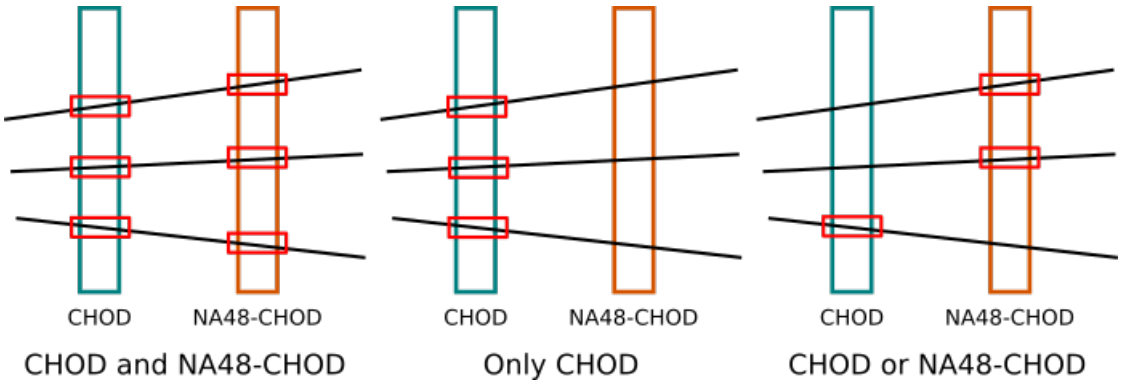

Figure 4.2: Three ways to match at the tracks association in CHOD and NA48-CHOD.

- $\left|t_{Downstream} - t_{trigger}\right| < 5\,\text{ns}$

4.3.3 Tracks separation

A minimum separation from track to track is requested in order to analyse a more clean sample of events. The Straw tracks are projected to the NA48-CHOD plane and on the first Straw chamber. The points obtained with the intersection of the plane have to have a distance of at least:

- 1 cm in the first Straw chamber plane
- 20 cm in the NA48-CHOD plane.

4.3.4 KTAG candidate selection

The KTAG candidate selection is made using the Downstream Time as input. The KTAG candidate is required to have more than four firing sectors. The candidate closer to the Downstream Time is choose when more that a candidate is found in association.

- KTAG sectors >4
- $|t_{KTAG} - t_{Downstream}| < 0.75\,\text{ns}$

4.3.5 GTK candidate selection

The match between the 3 downstream tracks and the correct GTK candidate is critical in order to evaluate correctly the transverse momentum. To that end, the KTAG candidate time, t_{KTAG}, is used to seek among the GTK candidates within a 1.4 ns window. For each GTK candidate a four-track vertex, three Straw tracks and one GTK track, fit is performed using the VertexLSF tool. The four tracks χ^2 is requested to be smaller that 25 (see figures 4.28, 4.29) and the GTK candidate that gives the best χ^2 value is selected. After a successful match between upstream and downstream event the kaon momentum p_K is known and all the kinematic quantities, such as p_T and missing mass, can be calculated.

4.3.6 Particle identification

At this stage of the selection, the MUV3 associations with the tracks are searched. A MUV3 candidate is considered associated to the track if its occurrence time is inside a 10 ns window centred on $t_{Downstream}$:

- $|t_{MUV3} - t_{Downstream}| < 5\,\text{ns}$

In case there are multiple candidates, the one with the closest time is chosen. If at least an association is found the tracks is considered a muon. The candidates are sought between the outer tiles of the MUV3 (see image 4.1), which are the one used to evaluate the MO2 L0 trigger decision.

4.3.7 Linear cut

The linear cut is the branching point of the Common selection: based on the cut result the events deviate to the $K_{3\pi}$, the $K_{\pi\mu\mu}$ or the $K_{\mu\nu\mu\mu}$ selection. The linear cut is a two dimensional cut made on p_T and ΔM_K; the latter quantity is calculated as follow:

$$\begin{aligned} M_{3\pi} &= \sqrt{\Big(\sum_{i=1}^{3} p_i(\pi)\Big)^2} \\ \Delta M_K &= M_{3\pi} - M_{K_{pdg}} \end{aligned} \tag{4.18}$$

The kaon mass evaluation, indicated with $M_{3\pi}$, is done using the three spectrometer tracks momentum in the pion assumption, as a consequence ΔM_K is expected to be zero

for $K_{3\pi}$ events. The left figure in caption 4.3 shows the effect of the linear cut on the $K_{\mu\nu\mu\mu}$ MC sample, the blue distribution, and the $K_{3\pi}$ Standard MC sample, the red distribution. The kinematic quantities, p_T and ΔM_K, constrain the $K_{3\pi}$ in the lower part of the plane. The $K_{\mu\nu\mu\mu}$ events are mainly distributed above the $K_{3\pi}$. In the histogram has been drawn in red the linear cut to separate the two distributions, it corresponds to the following equation:

$$p_T = -10^6\, c \cdot \Delta M_K + 20\,\mathrm{MeV}/c \tag{4.19}$$

The events above the linear cut line enter into the $K_{\mu\nu\mu\mu}$ selection, while the one below into the $K_{3\pi}$ and the $K_{\pi\mu\mu}$ selections. In correspondence of $\Delta M_K = 0$, it is possible to see that some $K_{3\pi}$ events have big p_T values, this anomaly in the transverse momentum is a sign of a wrong match of the downstream event with the upstream GTK candidate. The similar histogram, using $K_{\mu\nu\mu\mu}$ and $K_{\pi\mu\mu}$ MC samples, is shown in the right figure in caption 4.3. It is important to notice that the $K_{\pi\mu\mu}$ events, like the $K_{3\pi}$ one have small p_T and are concentrated in the lower part of the histogram. The $K_{\pi\mu\mu}$ events spread across the red linear cut line; because of that is expected contamination of $K_{\pi\mu\mu}$ in the $K_{\mu\nu\mu\mu}$ selection and a reduced acceptance for the normalisation on that channel.

In figure 4.4, the histogram p_T versus ΔM_K is shown for the 2017 data. Many events are visible in the region above the green line. This upper region, looking at the MC histograms, is not populated at all, those events are therefore rejected, this cut is called upper linear cut. As for the $K_{3\pi}$ MC is possible to see a feature in coincidence with $\Delta M_K = 0$. The corresponding equation of the upper linear cut is reported:

$$p_T = -10^6\, c \cdot \Delta M_K + 80\,\mathrm{MeV}/c \tag{4.20}$$

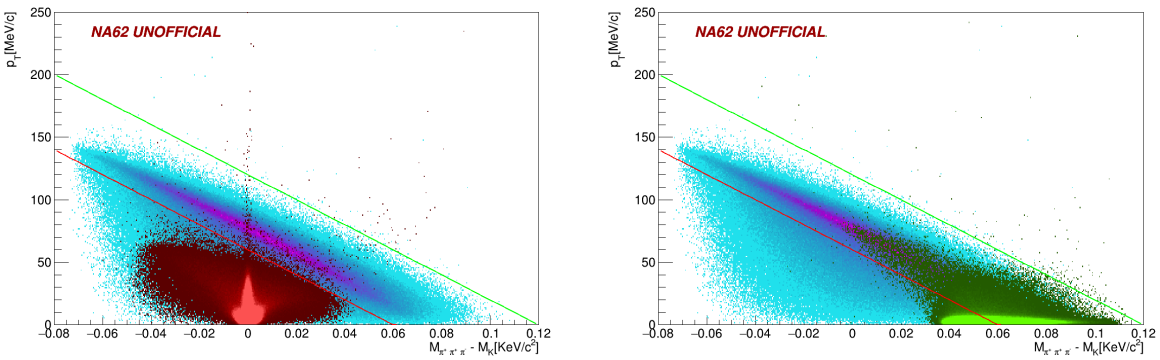

Figure 4.3: GTK transverse momentum (p_T) as a function of ΔM_K reconstructed from the three tracks, assuming three pions in the final state. The plot on the left shows the overlap the un-normalised $K_{\mu\nu\mu\mu}$ and $K_{3\pi}$ Standard MC. The plot on the right shows the overlap the un-normalised $K_{\mu\nu\mu\mu}$ and $K_{\pi\mu\mu}$ MC.

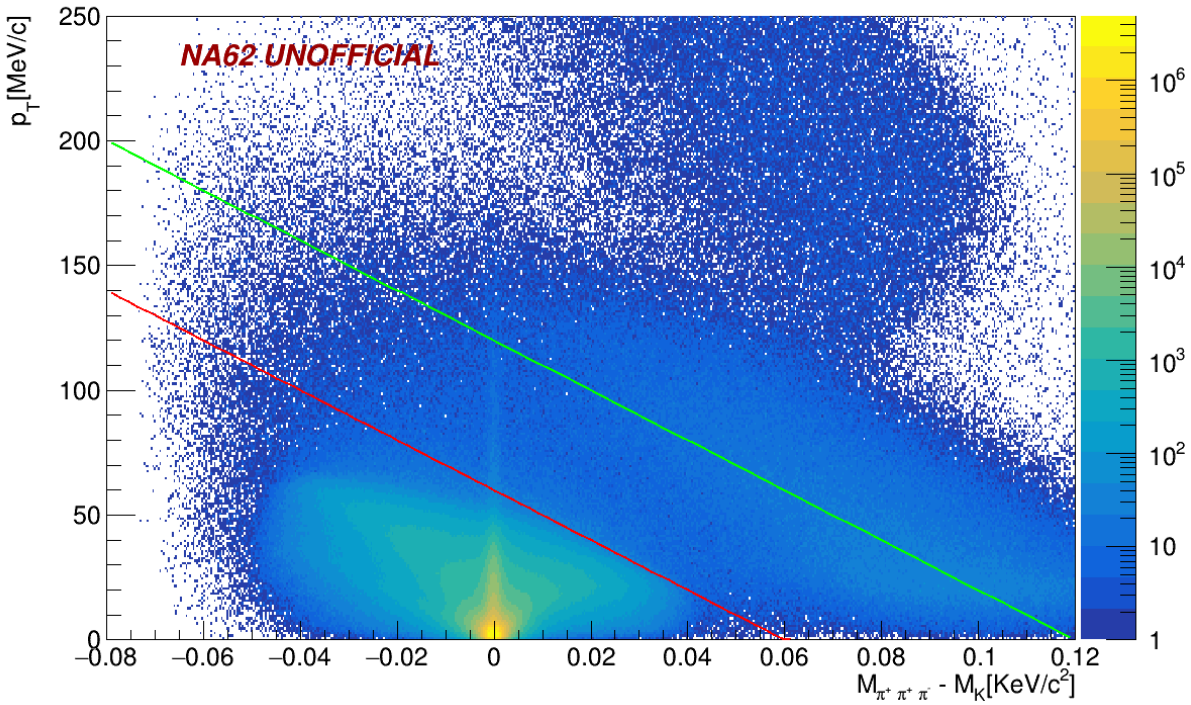

Figure 4.4: GTK transverse momentum (p_T) as a function of ΔM_K reconstructed from the three tracks assuming three a pions in the final state. The plot shows the 2017 data in logarithmic scale.

4.4 $K_{3\pi}$ event selection

The $K_{3\pi}$ selection aims at select a $K^+ \to \pi^+\pi^+\pi^-$ sample and use it for the estimation of the number of kaons. This selection follows the Common one which has been fully described in the previous section. The events selected are the ones that did not pass the linear cut, that means that are below the linear cut line (see histogram 4.4).

The last conditions that an event has to satisfy in order to be considered as a $K_{3\pi}$ event are reported:

1. the event must be located below the linear cut (not passed),
2. the number of tracks with MUV3 association have to be 0 or 1, and
3. the reconstructed kaon mass has to be within the following interval: $\left|M_{3\pi} - M_{K_{pdg}}\right| < 0.1 \cdot M_{K_{pdg}}$

Using all the $K_{3\pi}$ samples listed in table 4.2 the acceptance found for the $K_{3\pi}$ Standard MCs to the $K_{3\pi}$ selection is:

$$A_{K_{3\pi}}(K_{3\pi}) = (0.102 \pm 0.001) \qquad err\% = 1\% \tag{4.21}$$

where the error reported has been evaluated using the partial dispersion between the minimum and the maximum acceptance calculated among the different $K_{3\pi}$ Standard MC samples (see table 6.1).

The reconstructed 3π mass before the final cut is reported in figure 4.5, the contamination from other decay modes is negligible. The number of $K_{3\pi}$ events observed in the full 2017 sample is:

$$n_{K_{3\pi}} \sim 1.18 \cdot 10^8, \tag{4.22}$$

the exact value is reported in table 4.6.

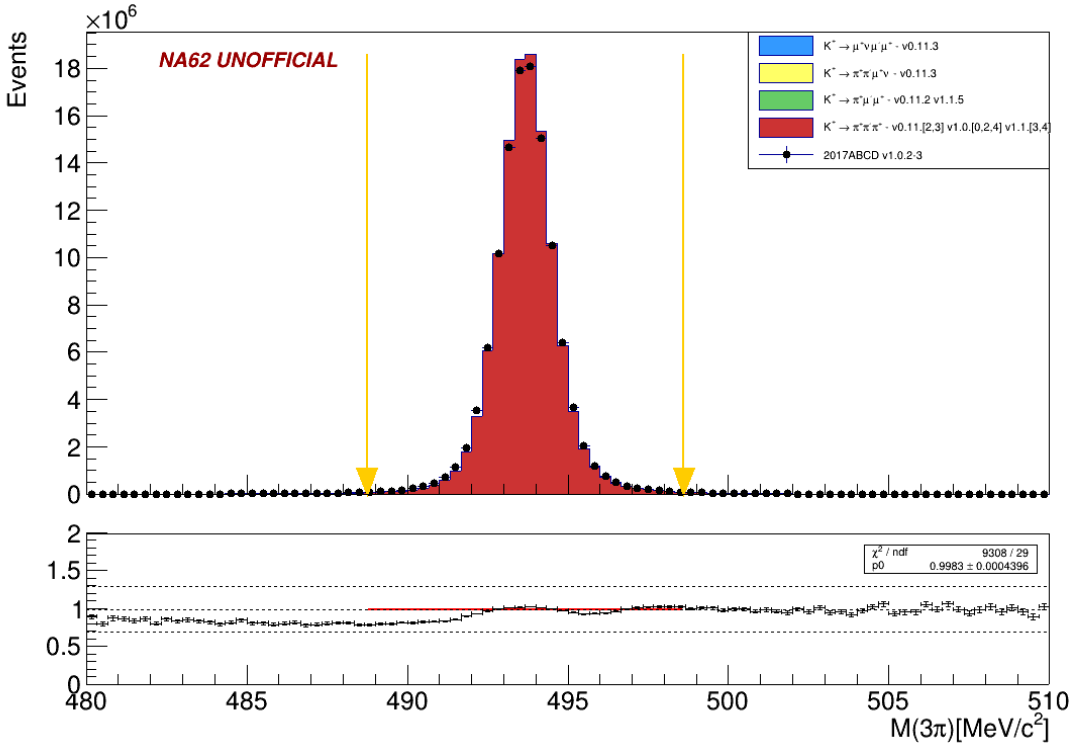

Figure 4.5: $M_{3\pi}$ spectrum for data and MC normalised on $K_{3\pi}$. The two orange arrows border the signal region: $[0.9 \cdot M_{K_{pdg}}, 1.1 \cdot M_{K_{pdg}}]$ MeV/c^2.

Table 4.5: Trigger efficiency calculated on $K_{3\pi}$ events.

Trigger condition	Trigger level	$\mathcal{E}$
RICH	L0	(0.998834±0.000007)
Qx	L0	(0.980818±0.000028)
KTAG	L1	(0.998389±0.000025)
Straw	L1	(0.94536±0.00014)
RICH × Qx × KTAG × Straw	L0-L1	(0.92465 ± 0.00015)

4.4.1 $K_{3\pi}$ trigger efficiencies

The study of the L0 and the L1 trigger efficiencies carry out on the events that passed the $K_{3\pi}$ selection is reported in this section. As already mentioned, the trigger efficiencies are measured on *Control* or L1 autopass events. The L0 trigger efficiency are always measured with respect to another detector; the RICH efficiency is measured on *Control* events with a CHOD primitive in time with the trigger time, while the Qx condition is measured with *Control* events with a RICH primitive in time. The efficiency for the four single components is reported in table 4.5, the corresponding error is evaluated with the binomial error:

$$\sigma(\mathcal{E}) = \sqrt{\frac{\mathcal{E}(1-\mathcal{E})}{total}} \tag{4.23}$$

where *total* is the number of events found in the reference detector.

The single efficiencies as a function of the negative track momentum are reported in figure 4.6, 4.7, 4.8 and 4.9. The RICH and the KTAG have an efficiency of about ∼99 % and are flat with respect to the momentum. The Qx efficiency, above ∼18 GeV/c, can be considered plane around a value of ∼98 % while it drops at small momentum. The Straw efficiency, with an average value of ∼94 %, is the lowest and also the one that depends the most from the momentum. The total efficiency calculated on the *Multi-track* trigger condition is:

$$\mathcal{E}_{Multi\text{-}track} = \mathcal{E}_{L0_{RICH}}\mathcal{E}_{L0_{Qx}}\mathcal{E}_{L1_{KTAG}}\mathcal{E}_{L1_{Straw}} = (0.92465 \pm 0.00015); \tag{4.24}$$

the biggest contribution to the value and the error comes from the L1 Straw efficiency.

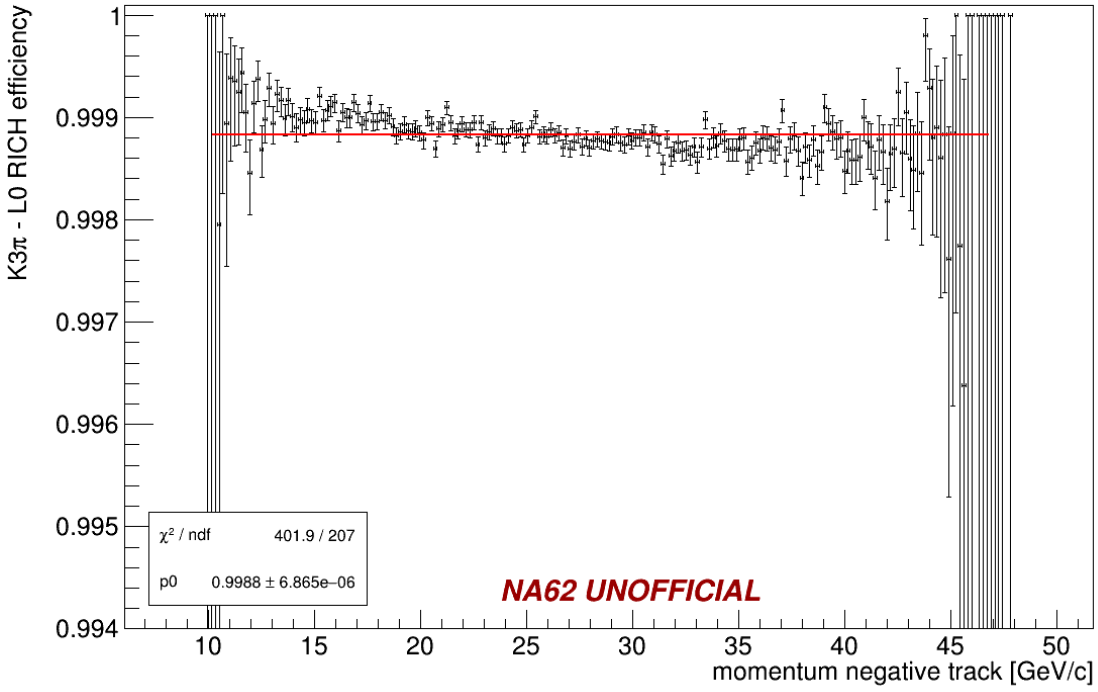

Figure 4.6: $K_{3\pi}$ Level-0 RICH trigger efficiency as a function of the negative track momentum.

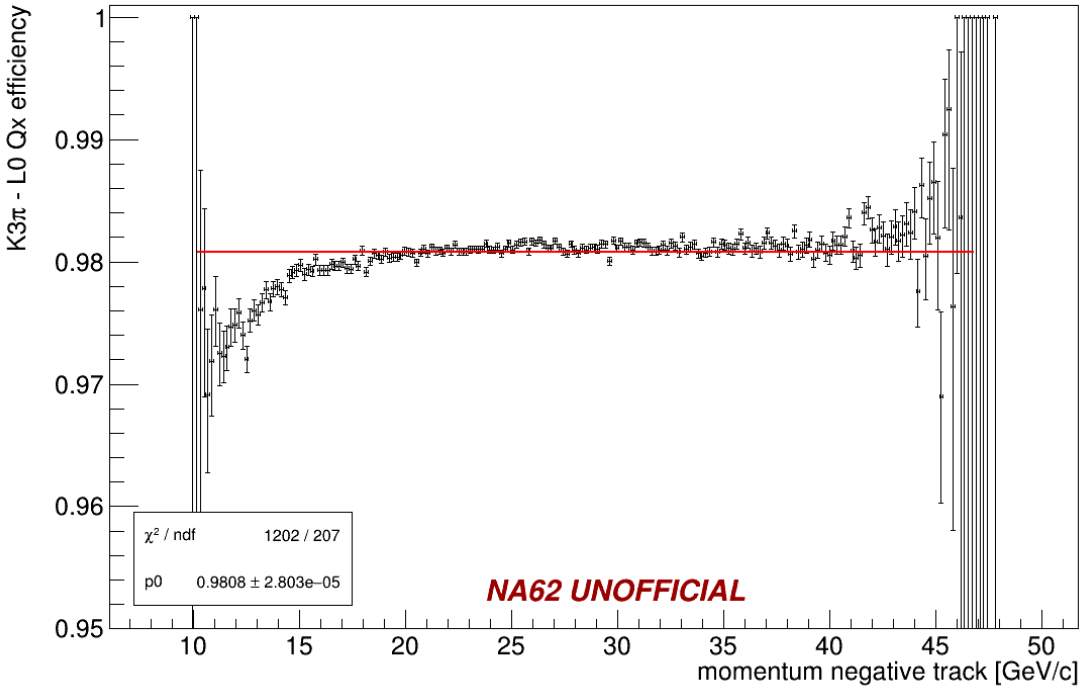

Figure 4.7: $K_{3\pi}$ Level-0 Qx trigger efficiency as a function of the negative track momentum.

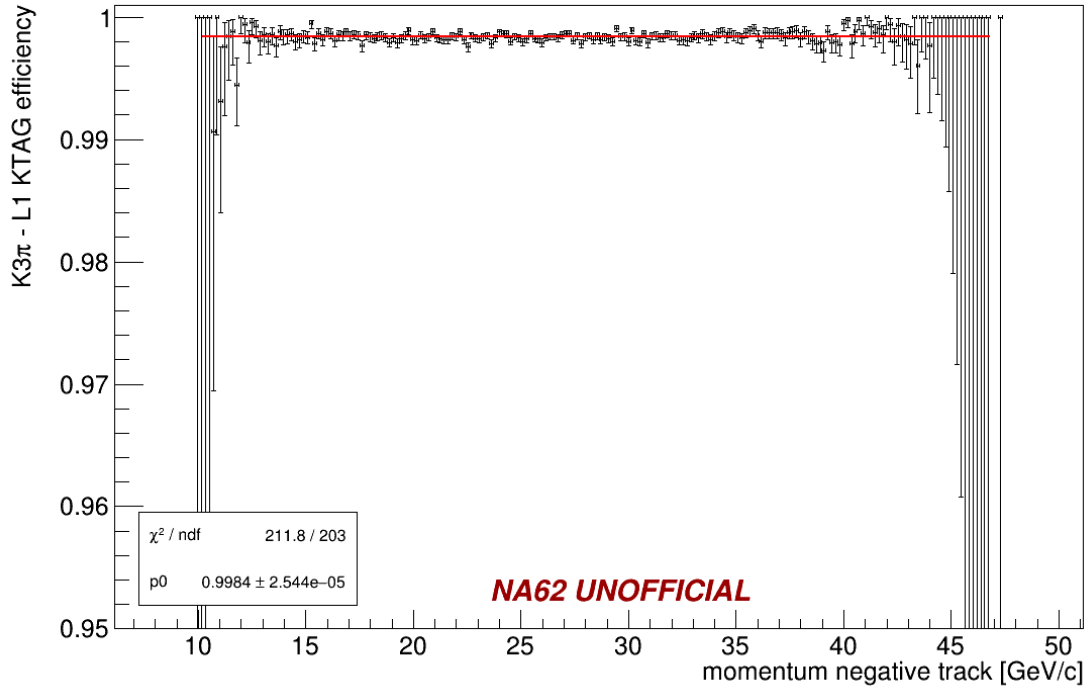

Figure 4.8: $K_{3\pi}$ Level-1 KTAG trigger efficiency as a function of the negative track momentum.

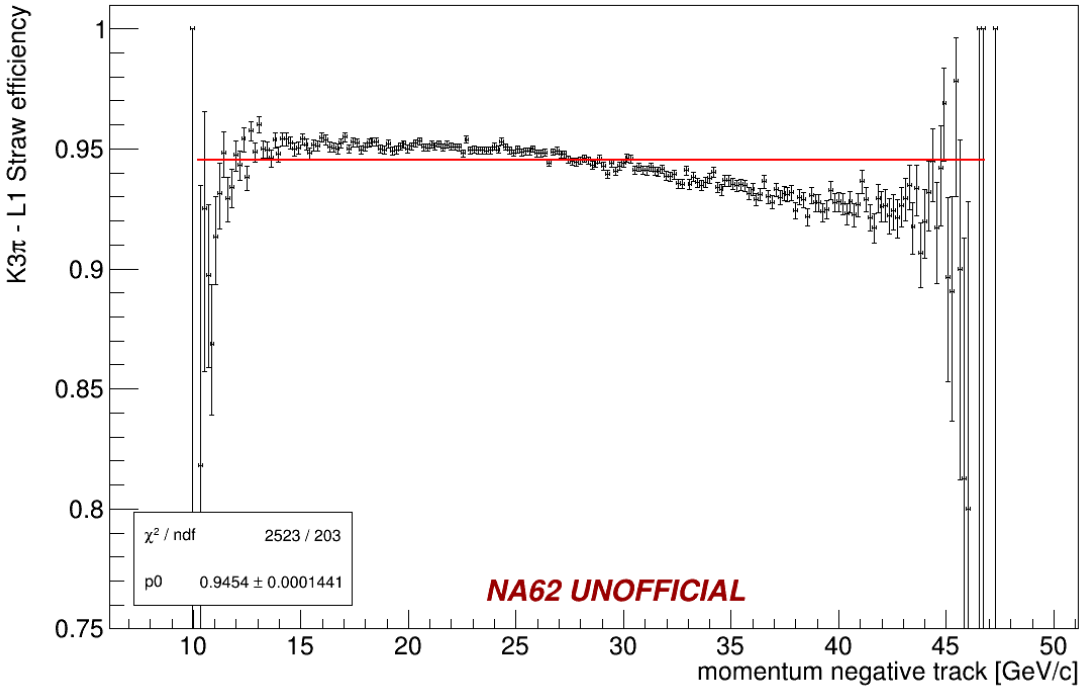

Figure 4.9: $K_{3\pi}$ Level-1 Straw trigger efficiency as a function of the negative track momentum.

4.5 $K_{\pi\mu\mu}$ event selection

As for the $K_{3\pi}$ selection, the $K_{\pi\mu\mu}$ one aims to select a sample of $K^+ \to \pi^+\mu^+\mu^-$ in order to estimate the number of kaons that occurs in the fiducial volume. The kaon mass is reconstructed taking into account the information provided by the particle identification:

$$M_{\pi\mu\mu} = \sqrt{(p_1(\pi) + p_2(\mu) + p_3(\mu))^2} \tag{4.25}$$

An event has to first pass the Common selection which has been already described. The events selected are the one that did not pass the linear cut, that means that are below the linear cut line (see histogram 4.4).

The last conditions that an event has to satisfy to be considered a $K_{\pi\mu\mu}$ event are reported:

1. the event must be located below the linear cut (not passed);
2. the number of tracks with MUV3 association have to be 2; and
3. the reconstructed kaon mass has to be within the following interval: $\left|M_{\pi\mu\mu} - M_{K_{pdg}}\right|$ $<0.1 \cdot M_{K_{pdg}}$.

The $K_{\pi\mu\mu}$ selection acceptance, using all the $K_{\pi\mu\mu}$ MC samples listed in table 4.2, is found to be:

$$A_{K_{\pi\mu\mu}}(K_{\pi\mu\mu}) = (0.0636 \pm 0.0007) \qquad err\% = 1\% \tag{4.26}$$

where the error reported has been evaluated using the partial dispersion between the minimum and the maximum acceptance calculated among the different $K_{\pi\mu\mu}$ MC samples (see table 6.2). The reconstructed $K_{\pi\mu\mu}$ mass before the final cut is shown in figure 4.10. The signal and the background on the left are well separated, and the contamination in the signal region from other decay modes is negligible. The number of $K_{\pi\mu\mu}$ events observed in the full 2017 sample is:

$$n_{K_{\pi\mu\mu}} = 5296. \tag{4.27}$$

4.5.1 $K_{\pi\mu\mu}$ trigger efficiencies

Given the small number of *Control* and autopass events at the end of the $K_{\pi\mu\mu}$ selection (see table 4.6) it is not possible to estimate the trigger efficiency on the *Di-muon* trigger condition ($\mathcal{E}_{Di\text{-}muon}$) using the data.

$$\mathcal{E}_{Di\text{-}muon} = \mathcal{E}_{L0_{RICH}}\mathcal{E}_{L0_{Qx}}\mathcal{E}_{L0_{MO2}}\mathcal{E}_{L1_{KTAG}}\mathcal{E}_{L1_{Straw}} \tag{4.28}$$

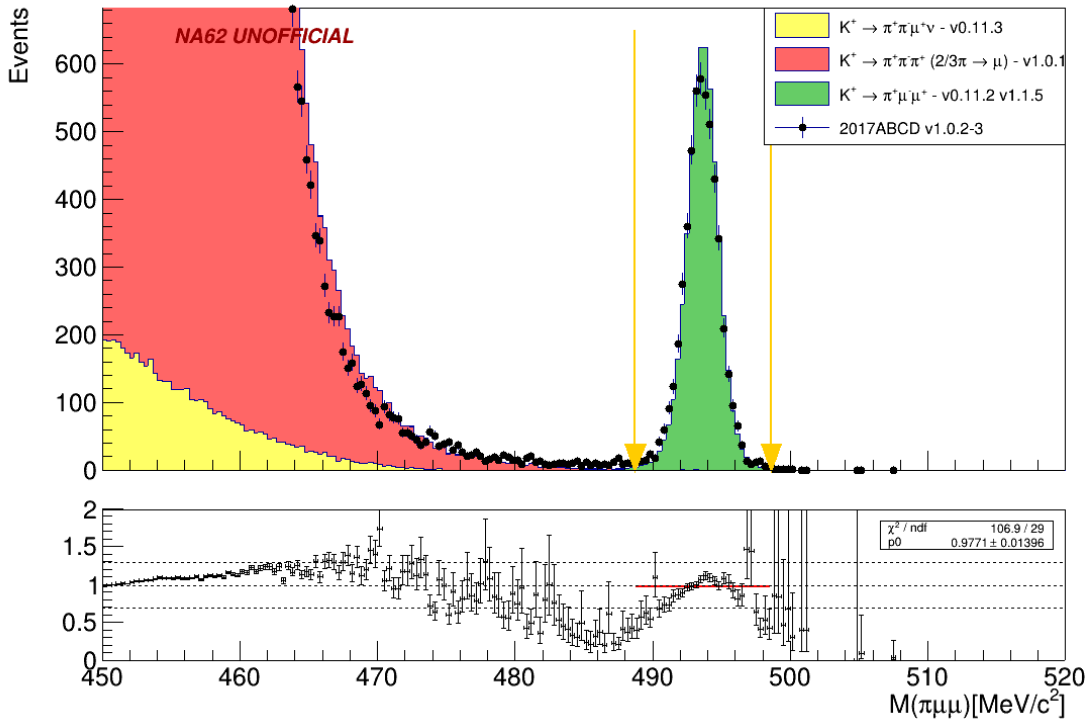

Figure 4.10: $M_{\pi\mu\mu}$ spectrum for data and MC normalised on $K_{\pi\mu\mu}$. The two arrows border the signal region: $[0.9 \cdot M_K,\, 1.1 \cdot M_K]$ MeV/c^2.

4.6 Number of kaons

After the calculation of the $K_{3\pi}$ and $K_{\pi\mu\mu}$ acceptances (4.21 and 4.26 respectively), it is possible to evaluate the number of kaons that occurred in the fiducial volume (n_K). The equation to compute $n_K(K_{3\pi})$, starting from the number of observed $K_{3\pi}$ events ($n_{K_{3\pi}}$), has to take in account the different downscales used along the 2017 data-taking

$$n_K(K_{3\pi}) = \frac{1}{BR(K_{3\pi}) \cdot A_{K_{3\pi}}(K_{3\pi}) \cdot \mathcal{E}_{Multi\text{-}track}} \sum_{run} n_{K_{3\pi}}(run) \cdot D_{Multi\text{-}track}(run). \quad (4.29)$$

where $D_{Multi\text{-}track}$ is the downscale used by the *Multi-track* trigger and $\mathcal{E}_{Multi\text{-}track}$ is the *Multi-track* trigger efficiency calculated in equation 4.24. In order to compute the $\mathrm{BR}(K^+ \to \mu^+\nu\mu^+\mu^-)$ the $n_K(K_{3\pi})$ needs to take in account the $D_{Di\text{-}muon}$ downscale. The number of kaons in the fiducial volume, taking in account the *Di-muon* trigger condition and calculated from the $n_{K_{3\pi}}$, corresponds to the following quantity:

$$\tilde{n}_K(K_{3\pi}) = \frac{1}{BR(K_{3\pi}) \cdot A_{K_{3\pi}}(K_{3\pi}) \cdot \mathcal{E}_{Multi\text{-}track}} \cdot \sum_{run} n_{K_{3\pi}}(run) \frac{D_{Multi\text{-}track}(run)}{D_{Di\text{-}muon}(run)}. \quad (4.30)$$

The similar formula using $n_{K_{\pi\mu\mu}}$ does not rely anymore on the downscale and is simply

$$\tilde{n}_K(K_{\pi\mu\mu}) = \frac{n_{K_{\pi\mu\mu}}}{BR(K_{\pi\mu\mu}) \cdot A_{K_{\pi\mu\mu}}(K_{\pi\mu\mu}) \cdot \mathcal{E}_{Di\text{-}muon}}, \quad (4.31)$$

where $\mathcal{E}_{Di\text{-}muon}$ is the *Di-muon* trigger efficiencies reported in equation 4.28. As stated previously in section 4.5.1, $\mathcal{E}_{Di\text{-}muon}$ can not be calculated from the data. To compare the two kaon estimations, the $\mathcal{E}_{L0_{MO2}}$ term will be neglected, while the remaining terms, shared by the *Multi-track* and the *Di-muon* trigger conditions, will be considered the same.

In table 4.7 is reported $\tilde{n}_K$ calculated from $n_{K_{3\pi}}$ and $n_{K_{\pi\mu\mu}}$. The $\tilde{n}_K$ errors are computed taking in account: BR, acceptance uncertainties and the number of observed events ($n_{K_{3\pi}}$ or $n_{K_{\pi\mu\mu}}$).

The two results can be compared with the statistical test

$$t = \frac{|val_1 - val_2|}{\sqrt{\sigma val_1^2 - \sigma val_2^2}}, \quad (4.32)$$

for $\tilde{n}_K(K_{3\pi})$ and $\tilde{n}_K(K_{\pi\mu\mu})$

$$t = 1.26 < 1.96 \quad \text{significant at 5\% level} \quad (4.33)$$

We can conclude that the two estimations of $\tilde{n}_K$, made independently with different trigger conditions, are compatible.

Table 4.6: Number of observed $n_{K_{3\pi}}$ and $n_{K_{\pi\mu\mu}}$ events in the full 2017 data sample.

Selection	Trigger condition	$n_{K_{3\pi}}$	$n_{K_{\pi\mu\mu}}$
$K_{3\pi}$	*Multi-track*	117730238	-
$K_{3\pi}$	*Control*	30524067	-
$K_{\pi\mu\mu}$	*Di-muon*	-	5296
$K_{\pi\mu\mu}$	*Control*	-	36

4.6.1 Comparison with the Control trigger

In table 4.7 is reported $\tilde{n}_K$ calculated from $n_{K_{3\pi}}$ and $n_{K_{\pi\mu\mu}}$ using the *Control* trigger: $\tilde{n}_K(K_{3\pi}\text{-}Control)$ and $\tilde{n}_K(K_{\pi\mu\mu}\text{-}Control)$. The formula used is similar to 4.30 and does not contain the trigger efficiency term:

$$\tilde{n}_K(K_{3\pi}\text{-}Control) = \frac{1}{BR(K_{3\pi}) \cdot A_{K_{3\pi}}(K_{3\pi})} \cdot \sum_{run} n_{K_{3\pi\text{-}Control}}(run) \frac{D_{Control}(run)}{D_{Di\text{-}muon}(run)}. \quad (4.34)$$

Computing the statistical test, introduced in equation 4.32, between $\tilde{n}_K(K_{3\pi}\text{-}Control)$ and $\tilde{n}_K(K_{3\pi})$ the value found is

$$t = 1.41, \quad (4.35)$$

that states that the two estimations, $\tilde{n}_K(K_{3\pi})$ and $\tilde{n}_K(K_{3\pi}\text{-}Control)$, are compatible.

The $K_{\pi\mu\mu}$ normalisation channel and $K_{\mu\nu\mu\mu}$ mode share the same trigger condition (*Di-muon*), as a consequence, $\mathcal{E}_{Di\text{-}muon}$ is the same; this is advantageous because the $\mathcal{E}_{Di\text{-}muon}$ will cancel during the estimation of the number of background event (see section 4.9.2) and will allow to use the $\tilde{n}_K(K_{\pi\mu\mu})$ value neglecting the trigger efficiency. For the same reason the data over MC plots, that will be presented in the next section, will use the $\tilde{n}_K(K_{\pi\mu\mu})$ kaon estimation as normalisation.

Using the $\tilde{n}_K(K_{3\pi})$ kaon estimation the efficiency do not cancel out and the expected background is proportional to

$$\frac{\mathcal{E}_{Di\text{-}muon}}{\mathcal{E}_{Multi\text{-}track}} \quad (4.36)$$

this will be shown in section 4.9.2.

Table 4.7: Estimation of the number of kaon decays in the fiducial volume taking in account the *Di-muon* trigger condition ($\tilde{n}_K$) using the full 2017 data sample. The estimation from the $K_{\pi\mu\mu}$ selection using the *Control* trigger has the biggest error because of the small number of events observed. The values reported are calculated neglecting the trigger efficiencies.

Selection	Trigger condition	$\tilde{n}_K$	err%
$K_{3\pi}$	*Multi-track*	$(90 \pm 1) \cdot 10^{10}$	1%
$K_{3\pi}$	*Control*	$(96 \pm 1) \cdot 10^{10}$	1%
$K_{\pi\mu\mu}$	*Di-muon*	$(86 \pm 3) \cdot 10^{10}$	3%
$K_{\pi\mu\mu}$	*Control*	$(11 \pm 2) \cdot 10^{11}$	18%

4.7 $K_{\mu\nu\mu\mu}$ event selection

The signal selection requires some additional steps compared to the one used as normalisation. In this section, the conditions to require on top of the Common selection are presented.

The selection starts requiring the two following conditions:

1. The event must be located above the linear cut and below the upper linear cut.

2. The number of tracks with MUV3 association must be equal to 3.

4.7.1 Dalitz plot cut

The right figure in caption 4.11 shows the Dalitz plot for the $K_{\mu\nu\mu\mu}$ MC. Since the signal is a four-body decay is not possible to show all the kinematic variables in a two-dimensional plot. The quantities plotted are the positive muons invariant mass ($I_{mass}(\mu^+\mu^+)$) versus the muon-neutrino invariant mass ($I_{mass}(\mu^-\nu)$); those are calculated as follow:

$$\begin{aligned} I_{mass}(\mu^+\mu^+) &= \sqrt{(p_{\mu^+} + p_{\mu^+})^2} \\ I_{mass}(\mu^-\nu) &= \sqrt{(p_K - p_{\mu^+} - p_{\mu^+})^2} \end{aligned} \tag{4.37}$$

The events are supposed to lay inside the triangle; however, some of them are placed outside. That is an indicator of a wrong GTK track matching, indeed the calculation of the muon-neutrino invariant mass involves the use of the GTK track. The same behaviour is visible also in the analogous Dalitz plots, obtained using the other muons couple permutations: $I_{mass}(\mu_1^+\mu^-)$ versus $I_{mass}(\mu_2^+\nu)$ and $I_{mass}(\mu_2^+\mu^-)$ versus $I_{mass}(\mu_1^+\nu)$. The aim of the Dalitz plot cut is to remove the events outside the triangle; this is achieved requiring the invariant masses muon-neutrino greater than the muon mass:

$$I_{mass}(\mu_i\nu) > m_\mu = 105.66\,\mathrm{MeV}/c \tag{4.38}$$

The right figure in caption 4.11 shows the effect described above in the data, the events rejected by the cut are mostly contributing at negative missing mass values in the $K_{\mu\nu\mu\mu}$ final plot (see plot 4.13).

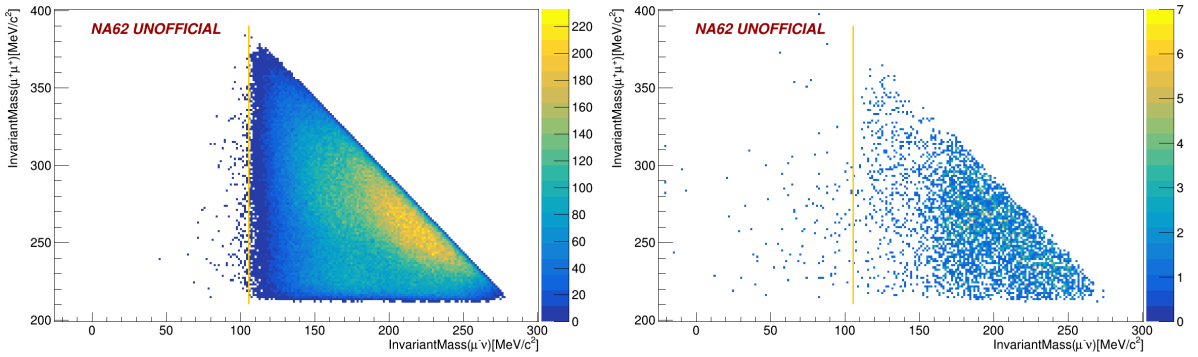

Figure 4.11: $I_{mass}(\mu^+\mu^+)$ versus $I_{mass}(\mu^-\nu)$ for $K_{\mu\nu\mu\mu}$ MC on the right and for 2017 data on the left. The orange vertical lines represent the muon mass (105.66 MeV/c^2), the reconstructed events with $I_{mass}(\mu^-\nu)$ below this threshold are rejected.

4.7.2 Other background sources

Another possible source of background, along with the ones described in section 4.1.1, is taken into account. The following channel:

$$K^+ \to \mu^+\nu_\mu \tag{4.39}$$

has a muon in the final state and is the most abundant kaon decay (see table 4.1). Because of the high intensity, many decays can occur simultaneously, and some of them might overlap developing a fake $K_{\mu\nu\mu\mu}$ signal. For example, a $K_{\pi\mu\mu}$ decay with a lost π mixed with a $K_{\mu 2}$, might trigger that process. In order to study a possible contamination of $K_{\mu 2}$, the following quantity has been investigated:

$$m^2_{miss}(K_{\mu 2}) = (p_K - p(\mu^+_{1,2}))^2 \tag{4.40}$$

The $K_{\mu 2}$ missing mass is computed with the kaon 4-momentum and the track 4-momentum assuming a muon in the final state; for each $K_{\mu\nu\mu\mu}$ candidate event two of those quantities are evaluated: only the positive tracks are used. The $K_{\mu 2}$ squared missing mass distribution is plotted in figure 4.12; in case of a $K_{\mu 2}$ event, is expected to peak at zero. From the histogram, it is possible to observe that the distribution of events is far from zero, the $K_{\mu 2}$ process, even if very abundant, does not enter into the signal selection with the mixing mechanism described above; for that reason no further protection has been developed against it.

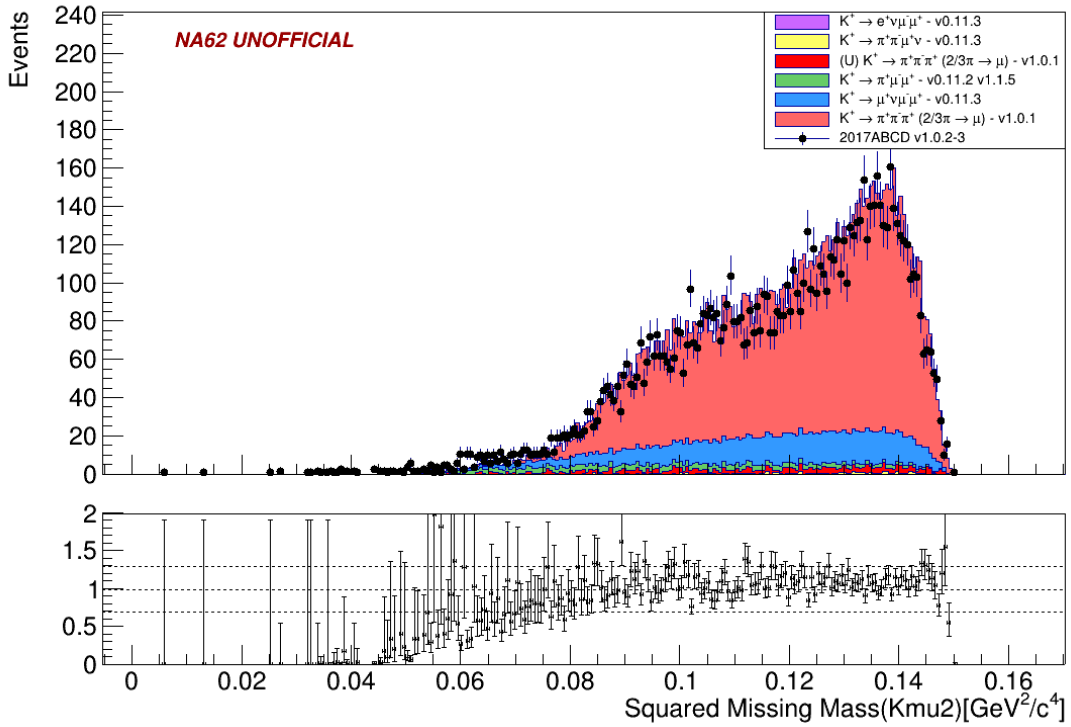

Figure 4.12: The $K_{\mu 2}$ squared missing mass spectrum for data and MC contributions normalised with $K_{\pi\mu\mu}$. The histogram is made before the Dalitz plot cut (see section 4.7.1), there is no trace of $K_{\mu 2}$ contamination.

4.8 $K_{\mu\nu\mu\mu}$ acceptance

The kinematic quantity used to estimate the number of $K_{\mu\nu\mu\mu}$ events is the squared missing mass ($m^2_{miss}(K_{\mu\nu\mu\mu})$ also shortened as m^2_{miss}), which is calculated as follow:

$$m^2_{miss}(K_{\mu\nu\mu\mu}) = \left(p_K - \sum_{i=1}^{3} p_i(\mu)\right)^2 \tag{4.41}$$

assuming as muons the three spectrometer tracks. In appendix 6.2, the $m^2_{miss}(K_{\mu\nu\mu\mu})$ is fully derived; it is possible to observe that all angles, between the kaon and the muons and between the muons couples, contribute to the computation; an error on the GTK candidate selection is propagated to that quantity. The $m^2_{miss}(K_{\mu\nu\mu\mu})$, calculated for the $K_{\mu\nu\mu\mu}$ signal, is expected to peak on the mass of the neutrino.

The $K_{\mu\nu\mu\mu}$ acceptance is evaluated counting the events into a reference interval: $[-0.0009, 0.0009]\,\mathrm{GeV}^2/c^4$. This region has been chosen based on an unsophisticated approach: it is wide enough to catch the majority of the $K_{\mu\nu\mu\mu}$ that arrive at this selection stage,

Table 4.8: The table lists the acceptances of the MC samples to the $K_{\mu\nu\mu\mu}$ selection. The signal region used is the reference one. The errors reported are calculated with the binomial error.

MC	$A_{K_{\mu\nu\mu\mu}}(MC)$	err%
$K_{\mu\nu\mu\mu}$	$(5909 \pm 8) \cdot 10^{-5}$	0.1%
$K_{e\nu\mu\mu}$	$(7 \pm 3) \cdot 10^{-6}$	43%
$K_{\pi\mu\mu}$ all samples	$(201 \pm 2) \cdot 10^{-5}$	1%
$K_{\mu 4}$	$(46 \pm 8) \cdot 10^{-8}$	17%
$K_{3\pi}$ all samples	-	-
$K_{3\pi}$ Capped	$(12 \pm 2) \cdot 10^{-9}$	17%
$K_{3\pi}$ Capped Near	$(10 \pm 5) \cdot 10^{-9}$	50%

Table 4.9: The acceptances for the normalisation selections: $K_{\pi\mu\mu}$ and $K_{3\pi}$. The errors reported are calculated with the binomial error, while the one marked with the asterisk are obtained with the partial dispersion between the minimum and the maximum acceptance reported in table 6.1 and 6.2.

MC	$A_{K_{\pi\mu\mu}}(MC)$	err%	$A_{K_{3\pi}}(MC)$	err%
$K_{\mu\nu\mu\mu}$	$(33 \pm 2) \cdot 10^{-6}$	6%	$(310 \pm 2) \cdot 10^{-5}$	0.6%
$K_{e\nu\mu\mu}$	$(62 \pm 8) \cdot 10^{-6}$	13%	$(53 \pm 7) \cdot 10^{-6}$	13%
$K_{\pi\mu\mu}$ all samples	$(636 \pm 7) \cdot 10^{-4}*$	1%	$(6 \pm 3) \cdot 10^{-7}$	50%
$K_{\mu 4}$	-	-	$(1502 \pm 1) \cdot 10^{-5}$	0.07%
$K_{3\pi}$ all samples	-	-	$(102 \pm 1) \cdot 10^{-3}*$	1%
$K_{3\pi}$ capped	$(3 \pm 3) \cdot 10^{-10}$	100%	$(1582 \pm 2) \cdot 10^{-7}$	0.1%
$K_{3\pi}$ capped Near	$(8 \pm 5) \cdot 10^{-9}$	62%	$(27 \pm 3) \cdot 10^{-8}$	11%

it is supposed to provide the biggest acceptance possible. A more rigorous signal region definition will be introduced in section 4.9.1. Using the reference interval, the $K_{\mu\nu\mu\mu}$ acceptance is found to be:

$$A_{K_{\mu\nu\mu\mu}}(K_{\mu\nu\mu\mu}) = (0.05909 \pm 0.00008) \qquad err\% = 0.1\% \tag{4.42}$$

The error has been evaluated with the binomial error. The MC samples acceptances for the $K_{3\pi}$, $K_{\pi\mu\mu}$ and $K_{\mu\nu\mu\mu}$ selections are reported in table 4.8 and 4.9.

Final plot

The squared missing mass spectrum with data and MCs superimposed is reported in figure 4.13. The image shows two main structures: the first one, coloured in blue, is centred at 0 and corresponds to the signal; the second structure instead, is placed on the signal peak

right and consists in the $K_{3\pi}$ background (coloured in magenta). The $K_{3\pi}$ background deeply enters into the signal region but despite that the two structures are discernible. Below the signal peak, it is observable a green component due to the $K_{\pi\mu\mu}$ events that enter in the selection; the $K_{\pi\mu\mu}$ is the second biggest background component. The other backgrounds considered are present in a small percentage, the only one that deserves to be mentioned is the Near-upstream $K_{3\pi}$ which is coloured in red. The squared missing

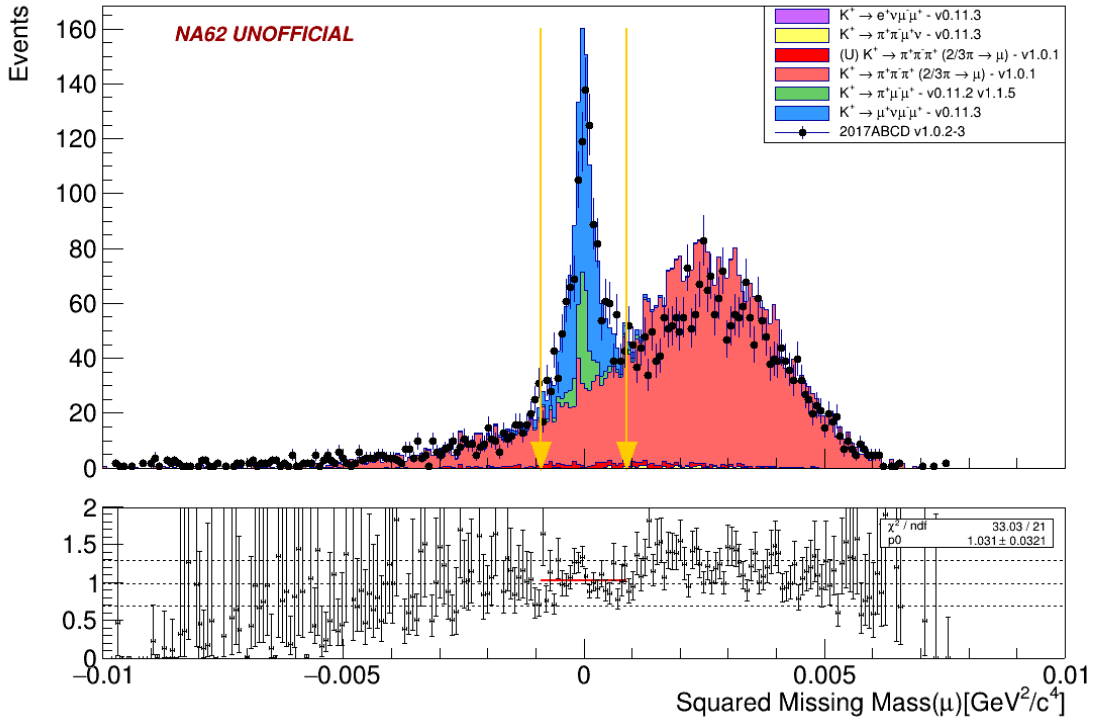

Figure 4.13: The $K_{\mu\nu\mu\mu}$ final plot shows the squared missing mass spectrum for data and MC normalised on $K_{\pi\mu\mu}$. The two arrows border the standard signal region: $[-0.0009\ ,\ 0.0009]\ \mathrm{GeV}^2/c^4$. The $K_{\mu\nu\mu\mu}$ MC has been normalised with the theoretical BR value.

mass spectrum is normalised with $K_{\pi\mu\mu}$ number of kaons estimation. The MC samples overshoot a bit the data, this is visible on the top of the $K_{3\pi}$ peak.

4.8.1 $K_{\mu\nu\mu\mu}$ Capped MC studies

In this section some features of the $K_{3\pi}$ Capped Monte Carlo will be discussed: a study on pion early decays and the effect of the upstream pileup generator.

4.8.2 $K_{3\pi}$ early decay study

In section 4.1.1, the primary background sources have been introduced; furthermore, the main element identified as a cause of background were the pion early decays. Using the Monte Carlo, it is possible to study the early decays that arrive at the end of the $K_{\mu\nu\mu\mu}$ selection. To that end, the $K_{3\pi}$ Fast Capped MC sample has been examined. In figure 4.14, it is plotted the number of early decays as a function of the $m^2_{miss}(K_{\mu\nu\mu\mu})$. There

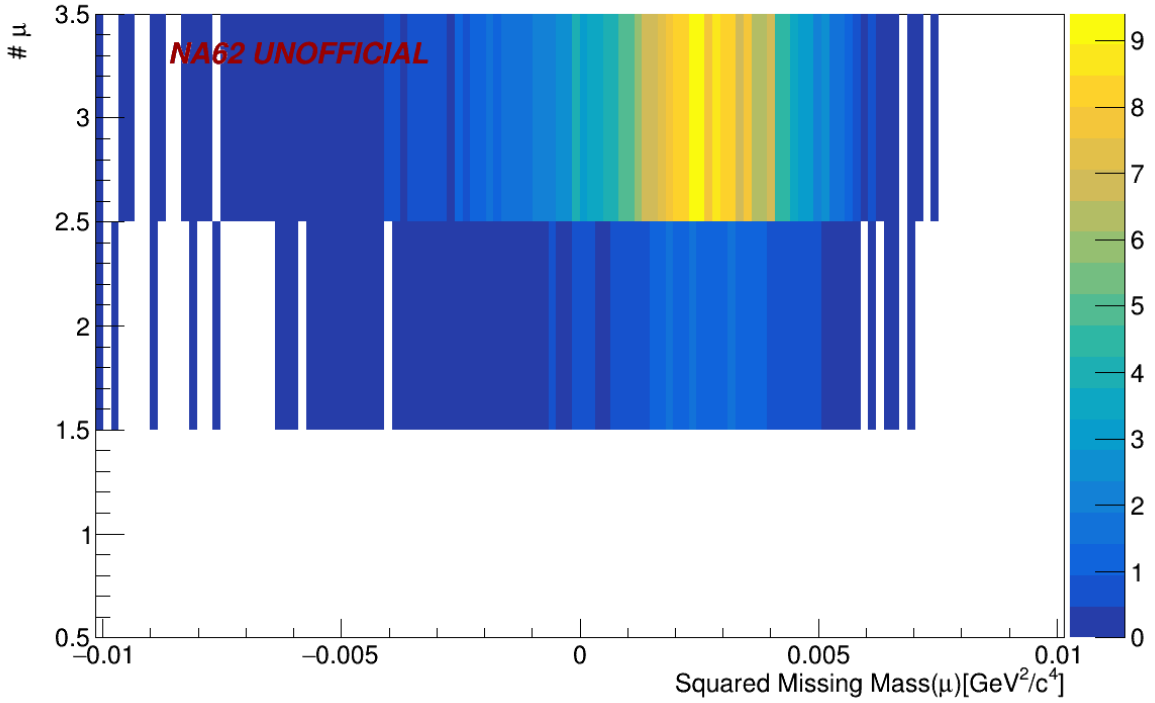

Figure 4.14: Number of muon in final state ($\#\mu$) or number of early decays versus $m^2_{miss}(K_{\mu\nu\mu\mu})$ for the $K_{3\pi}$ Fast Capped MC sample. Each event contributes to the plot with the weight provided by the MC.

are no events with one decay because the Fast Capped sample only contains 2 or 3 early decays. In particular, the majority of them is located in the row that corresponds to 3 early decays: about ∼82 % of the background has 3 early decays while the remaining part

has only 2 early decays.

4.8.3 Upstream pileup generator effect

The plot 4.15 shows the squared missing mass spectrum for data and MC, in particular, the $K_{3\pi}$ Fast Capped MC has been analysed without the upstream pileup generator. Comparing the plot with 4.13 is visible a lack of events below the signal peak. The GTK pileup populates the signal region and as a consequence, will contribute directly to the background estimation.

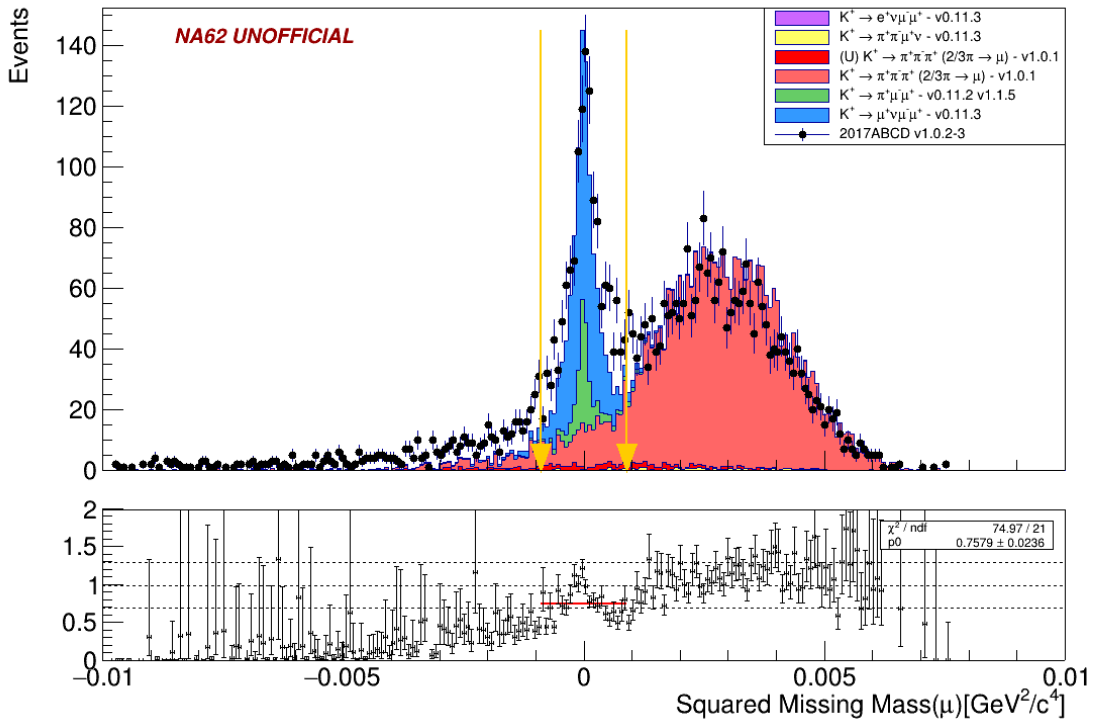

Figure 4.15: The final $K_{\mu\nu\mu\mu}$ plot, the upstream pileup generator for the $K_{3\pi}$ background is switched off.

4.9 BR evaluation

The procedure used to calculate the Branching Ratio of the $K_{\mu\nu\mu\mu}$ mode will be shown, in this section. At first, a more rigorous signal region definition, based on the resolution of the signal peak, will be introduced. The evaluation of the background budget will follow;

Table 4.10: The table shows the $K_{\mu\nu\mu\mu}$ signal regions ordered by window size, the corresponding acceptance and the observed events are reported. The acceptance errors are calculated with the binomial error.

Signal region	Range [GeV$^2/c^4$]	$A_{K_{\mu\nu\mu\mu}}(K_{\mu\nu\mu\mu})$	err%	Observed Events
1σ	[-0.00024, 0.00024]	0.03610 ± 0.00006	0.2%	645
2σ	[-0.00047, 0.00047]	0.05139 ± 0.00007	0.1%	1018
3σ	[-0.00071, 0.00071]	0.05731 ± 0.00008	0.1%	1277
reference	[-0.00090, 0.00090]	0.05909 ± 0.00008	0.1%	1408

the section will conclude with an investigation of the errors that contributes the most to the BR.

4.9.1 Signal region definition

A more rigorous signal region definition can be determined from the data, measuring the resolution of the signal peak. In figure 4.16, the squared missing mass spectrum for the 2017 data is shown. The result of the fit is superimposed to the distribution; the function used to fit is:

$$F(x) = \alpha \cdot e^{(-x^2/(2\sigma^2))} + e^{(\beta+\gamma\cdot x+\epsilon\cdot x^2)} + \eta \tag{4.43}$$

where α, σ, β, γ, ϵ and η are free parameters. The function $F(x)$ is composed by a Gaussian and an exponential function that describes the background. The Gaussian resolution $\sigma_{m^2_{miss}}$ (or simply σ) is found to be:

$$\sigma_{m^2_{miss}} = (23.5 \pm 2.1) \cdot 10^{-5}\text{GeV}^2/c^4 \tag{4.44}$$

The signal regions are defined as integer multiples of the sigma value: $[-n \cdot \sigma, +n \cdot \sigma]$. In table 4.10, the signal regions are summarised along with their relative acceptance and observed events.

4.9.2 Background budget

To make a proper count of the number of $K_{\mu\nu\mu\mu}$, events the background have to be estimated and then subtracted from the observed events. The following background sources are considered to evaluate the contamination in the signal region:

- $K^+ \to e^+\nu_e\mu^+\mu^-$

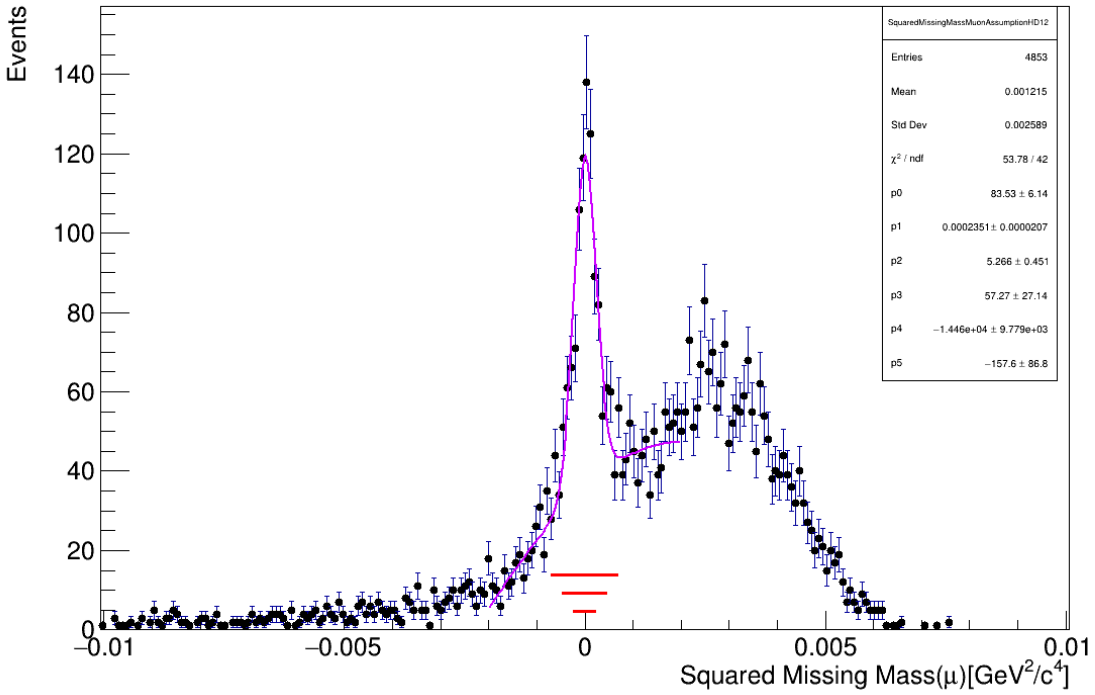

Figure 4.16: $K_{\mu\nu\mu\mu}$ squared missing mass spectrum for 2017 data. The horizontal bars in red below the peak represent the 1σ, 2σ and 3σ signal region according to the value obtained with the fit.

- $K^+ \to \pi^+\mu^+\mu^-$
- $K^+ \to \pi^+\pi^-\mu^+\nu_\mu$
- $K^+ \to \pi^+\pi^+\pi^-$ Fast Capped MC
- $K^+ \to \pi^+\pi^+\pi^-$ Near Fast Capped MC

The number of background events from $K_{3\pi}$ can be evaluated as:

$$nB_{K_{3\pi}} = \tilde{n}_K(K_{3\pi}) \cdot A_{K_{\mu\nu\mu\mu}}(K_{3\pi}) \cdot BR(K_{3\pi}) \cdot \mathcal{E}_{Di\text{-}muon}. \tag{4.45}$$

where $\tilde{n}_K$ is the number the kaon decays taking in account the *Di-muon* trigger condition (see table 4.7). The acceptance of the $K_{\mu\nu\mu\mu}$ selection to the $K_{3\pi}$ events ($A_{K_{\mu\nu\mu\mu}}(K_{3\pi})$), is calculated in the specific signal region interval: 1σ, 2σ, 3σ or reference. Replacing the equation 4.30 into 4.45 the background estimation $nB_{K_{3\pi}}$ becomes

$$nB_{K_{3\pi}} = \frac{\cancel{BR(K_{3\pi})} \cdot A_{K_{\mu\nu\mu\mu}}(K_{3\pi}) \cdot \mathcal{E}_{Di\text{-}muon}}{\cancel{BR(K_{3\pi})} \cdot A_{K_{3\pi}}(K_{3\pi}) \cdot \mathcal{E}_{Multi\text{-}track}} \sum_{run} n_{K_{3\pi}}(run) \frac{D_{Multi\text{-}track}(run)}{D_{Di\text{-}muon}(run)} \tag{4.46}$$

Table 4.11: Expected background events considering the reference signal region.

MC	Background events (nB)	err%
$K_{e\nu\mu\mu}$	<1	-
$K_{\pi\mu\mu}$	167 ± 7	4%
$K_{\mu 4}$	6 ± 4	67%
$K_{3\pi}$ Capped	599 ± 97	16%
$K_{3\pi}$ Capped Near	35 ± 18	51%
Total-Background	(807 ± 99)	12%

The background estimation depends on the following ratio $\mathcal{E}_{Di\text{-}muon}/\mathcal{E}_{Multi\text{-}track}$, where the $\mathcal{E}_{Di\text{-}muon}$ is not known. Using instead the $\tilde{n}_K$ estimation from $K_{\pi\mu\mu}$ the equation 4.45 can be rewritten using 4.31

$$\begin{aligned} nB_{K_{3\pi}} &= \frac{n_{K_{\pi\mu\mu}}}{A_{K_{\pi\mu\mu}}(K_{\pi\mu\mu}) \cdot BR(K_{\pi\mu\mu}) \cdot \cancel{\mathcal{E}_{Di\text{-}muon}}} \cdot BR(K_{3\pi}) \cdot A_{K_{\mu\nu\mu\mu}}(K_{3\pi}) \cdot \cancel{\mathcal{E}_{Di\text{-}muon}} \\ &= \frac{A_{K_{\mu\nu\mu\mu}}(K_{3\pi}) \cdot BR(K_{3\pi})}{A_{K_{\pi\mu\mu}}(K_{\pi\mu\mu}) \cdot BR(K_{\pi\mu\mu})} n_{K_{\pi\mu\mu}} \end{aligned} \tag{4.47}$$

The background estimation does not depend anymore by $\mathcal{E}_{Di\text{-}muon}$ that cancels out in the ratio. As a consequence the $\tilde{n}_K(K_{\pi\mu\mu})$ (provided in table 4.7) can be used for calculating the amount of background events neglecting the trigger efficiencies.

The error on the expected background events takes into account the following terms:

$$\sigma nB_{K_{3\pi}} = nB_{K_{3\pi}} \cdot \sqrt{\left(\frac{\sigma\tilde{n}_K(K_{\pi\mu\mu})}{\tilde{n}_K(K_{\pi\mu\mu})}\right)^2 + \left(\frac{\sigma A_{K_{\mu\nu\mu\mu}}(K_{3\pi})}{A_{K_{\mu\nu\mu\mu}}(K_{3\pi})}\right)^2 + \left(\frac{\sigma BR(K_{3\pi})}{BR(K_{3\pi})}\right)^2} \tag{4.48}$$

Analogous formulas like 4.47 and 4.48 can be written for the other backgrounds. The total amount of background events is calculated with a sum of all the contributions, while the total error is obtained with the quadrature:

$$Total\text{-}Background = \sum_{mode} nB_{K_{mode}} \tag{4.49}$$

$$\sigma Total\text{-}Background = \sqrt{\sum_{mode} \left(\sigma nB_{K_{mode}}\right)^2} \tag{4.50}$$

The expected number of background events, calculated for each mode in the reference signal region, and the Total-Background are tabulated in table 4.11 with relative errors.

4.9.3 BR evaluation

The expected background is subtracted from the observed events as follow:

$$n_{K_{\mu\nu\mu\mu}} = Observed\text{-}Events - Total\text{-}Background \tag{4.51}$$

$$\sigma n_{K_{\mu\nu\mu\mu}} = \sqrt{\sigma Observed\text{-}Events^2 + \sigma Total\text{-}Background^2} \tag{4.52}$$

Combining the observed events, in table 4.10, together with the background estimation provided in table 4.11, the number of $K_{\mu\nu\mu\mu}$ events for the reference signal region is:

$$n_{K_{\mu\nu\mu\mu}} = (601 \pm 106) \quad err\% = 18\% \tag{4.53}$$

Finally, the $K^+ \to \mu^+\nu_\mu\mu^+\mu^-$ Branching Ratio can be calculated using the following formulas:

$$BR(K_{\mu\nu\mu\mu}) = \frac{n_{K_{\mu\nu\mu\mu}}}{A_{K_{\mu\nu\mu\mu}}(K_{\mu\nu\mu\mu}) \cdot \tilde{n}_K(K_{\pi\mu\mu})} \tag{4.54}$$

$$\sigma BR(K_{\mu\nu\mu\mu}) = BR(K_{\mu\nu\mu\mu}) \cdot \sqrt{\left(\frac{\sigma n_{K_{\mu\nu\mu\mu}}}{n_{K_{\mu\nu\mu\mu}}}\right)^2 + \left(\frac{\sigma A_{K_{\mu\nu\mu\mu}}(K_{\mu\nu\mu\mu})}{A_{K_{\mu\nu\mu\mu}}(K_{\mu\nu\mu\mu})}\right)^2 + \left(\frac{\sigma \tilde{n}_K(K_{\pi\mu\mu})}{\tilde{n}_K(K_{\pi\mu\mu})}\right)^2} \tag{4.55}$$

Using the acceptance calculated in equation 4.42 and the kaon flux estimation calculated on $K_{\pi\mu\mu}$, reported in table 4.7, the value found for the reference signal region is:

$$BR(K^+ \to \mu^+\nu_\mu\mu^+\mu^-) = (1.18 \pm 0.21) \cdot 10^{-8} \qquad err\% = 18\% \tag{4.56}$$

The error reported is of the order of $\sim$20 %, considering the terms in equation 4.55, the one that dominates among the other is the expected number signal events:

$$\frac{\sigma n_{K_{\mu\nu\mu\mu}}}{n_{K_{\mu\nu\mu\mu}}} \simeq 18\% \tag{4.57}$$

which in turn is determined by the error on the number of expected background estimated from the $K_{3\pi}$ Capped Fast MC (see table 4.11). The error on the $K_{\mu\nu\mu\mu}$ acceptance to the $K_{3\pi}$ Capped MC ($A_{K_{\mu\nu\mu\mu}}(K_{3\pi Capped})$) is the quantity that drives the uncertainties on the BR (see table 4.8), this is due to the poor MC statistics to describe the background.

4.9.4 BR as a function of the signal regions

In this section the procedure to calculate the $K^+ \to \mu^+\nu_\mu\mu^+\mu^-$ BR will be performed for all the signal regions introduced in section 4.9.1.

The $K_{3\pi}$ background deeply enters in the signal regions from the right; its shape has proven to be dependent on the upstream pileup generator (see section 4.8.3); it is then

essential to understand if the estimation of background events is reliable despite the signal region choice.

In figure 4.17 the BR estimation is plotted for different signal regions. Because of the error associated with the BR, the values found are consistent between them; the BR error hides the systematic effect if present. The red line in the plot reports the theoretical value of the Branching Ratio[10]:

$$BR^{theory}(K^+ \to \mu^+\nu_\mu\mu^+\mu^-) = 1.35 \cdot 10^{-8} \tag{4.58}$$

All the BR values are compatible with the theoretical estimation.

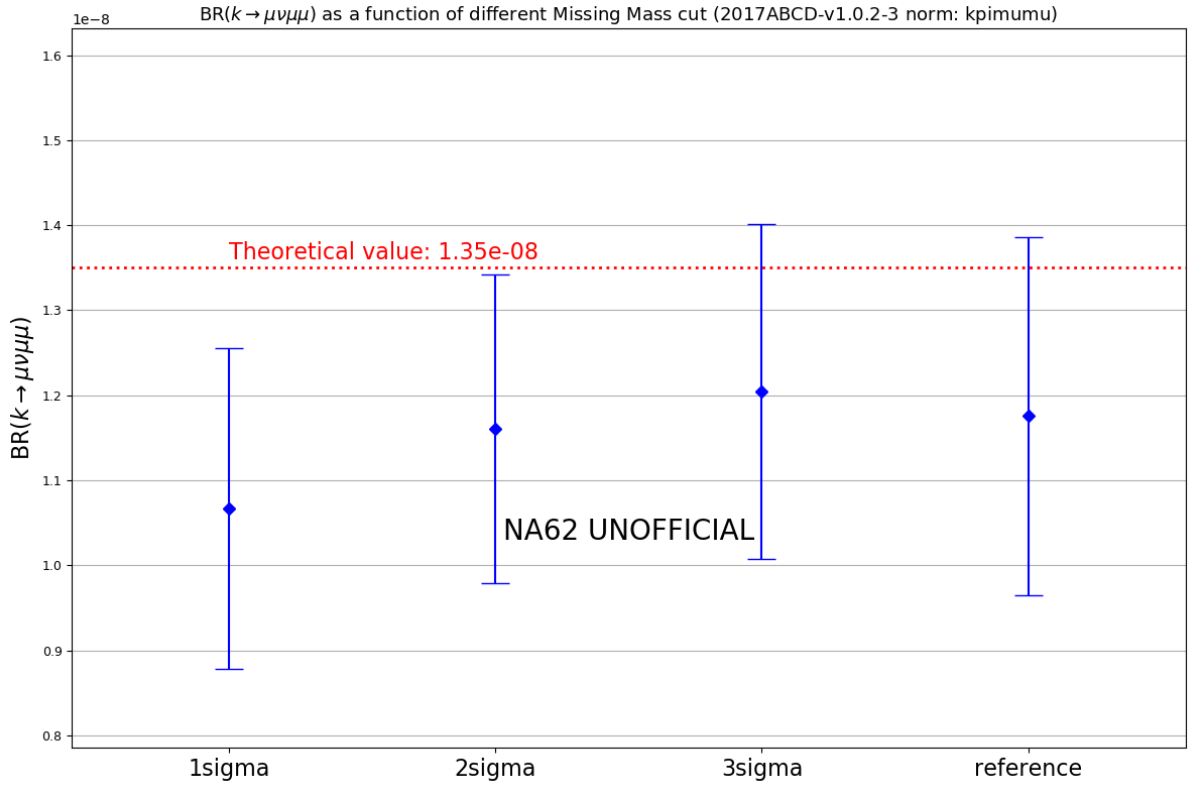

Figure 4.17: The $K^+ \to \mu^+\nu_\mu\mu^+\mu^-$ BR evaluation as a function of the signal regions. The BR theoretical value is indicated with the dotted red line.

4.10 Data over MC comparison

In this section, the data over Monte Carlo plots for the $K_{3\pi}$, $K_{\pi\mu\mu}$ and $K_{\mu\nu\mu\mu}$ selections are showed. In each page it is plotted one quantity, in the top row the distribution of $K_{3\pi}$ and $K_{\pi\mu\mu}$ normalisation channel are paged side-by-side; in the bottom part is shown the quantity for the $K_{\mu\nu\mu\mu}$ selection.

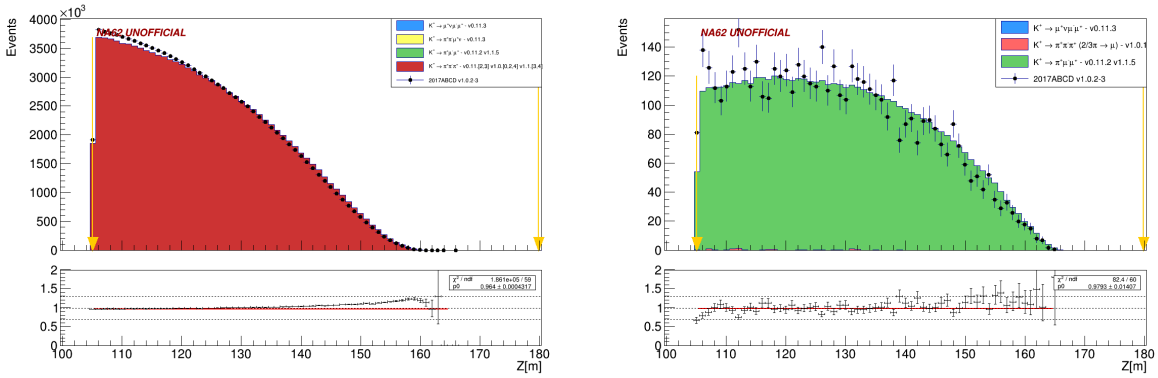

Figure 4.18: Vertex Z position for events passing the $K_{3\pi}$ (left) and $K_{\pi\mu\mu}$ (right) event selections.

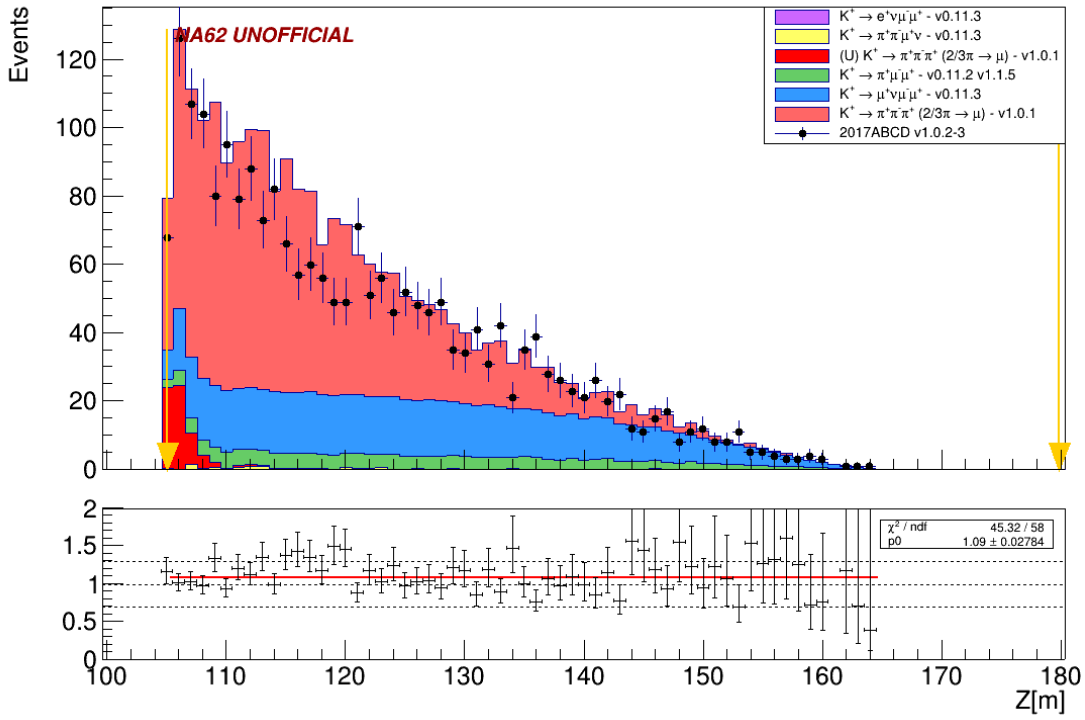

Figure 4.19: Vertex Z position for $K_{\mu\nu\mu\mu}$ events before the final m^2_{miss} cut. The arrows mark the Z coordinate cut applied during the Common selection.

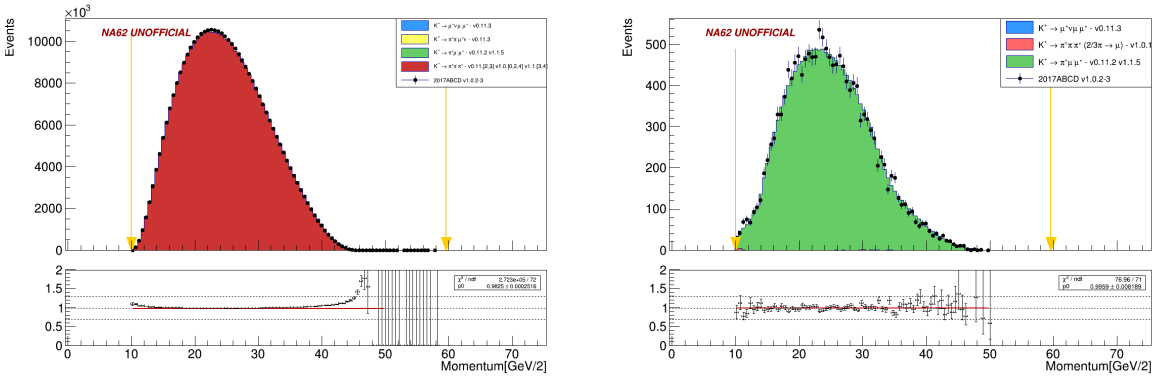

Figure 4.20: Straw tracks momentum for events passing the $K_{3\pi}$ (left) and $K_{\pi\mu\mu}$ (right) event selections.

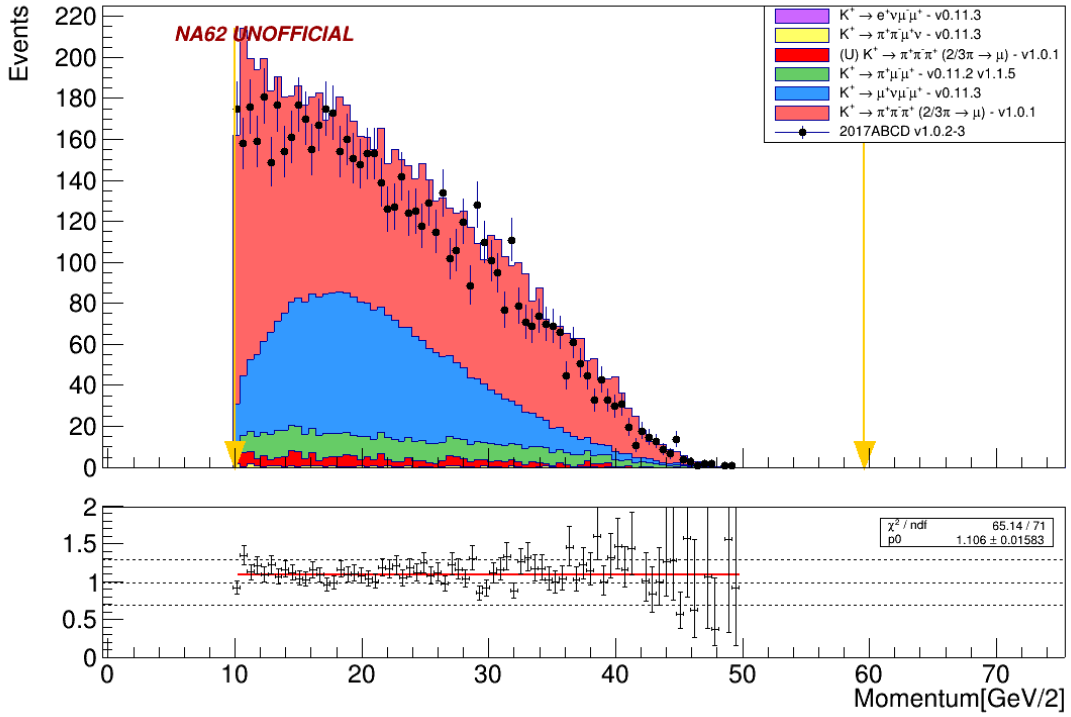

Figure 4.21: Straw tracks momentum for $K_{\mu\nu\mu\mu}$ events before the final m^2_{miss} cut. The arrows mark the momentum cut applied during the Common selection.

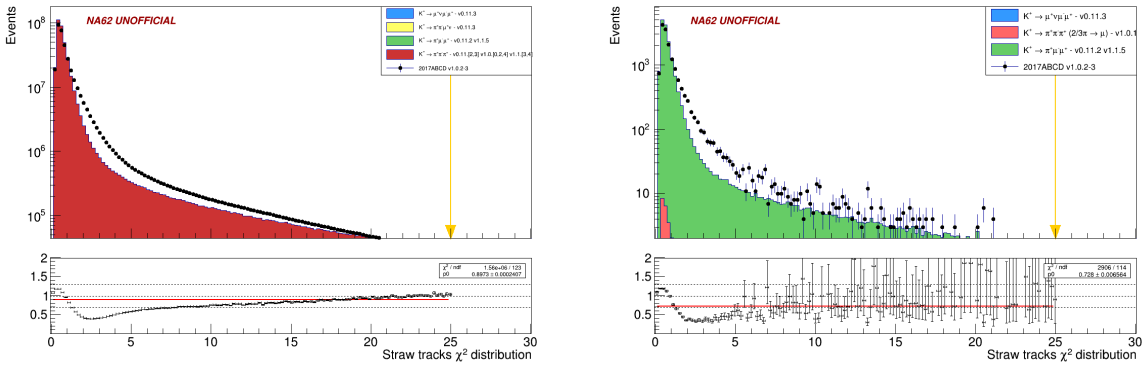

Figure 4.22: Straw tracks χ^2 for events passing the $K_{3\pi}$ (left) and $K_{\pi\mu\mu}$ (right) event selections.

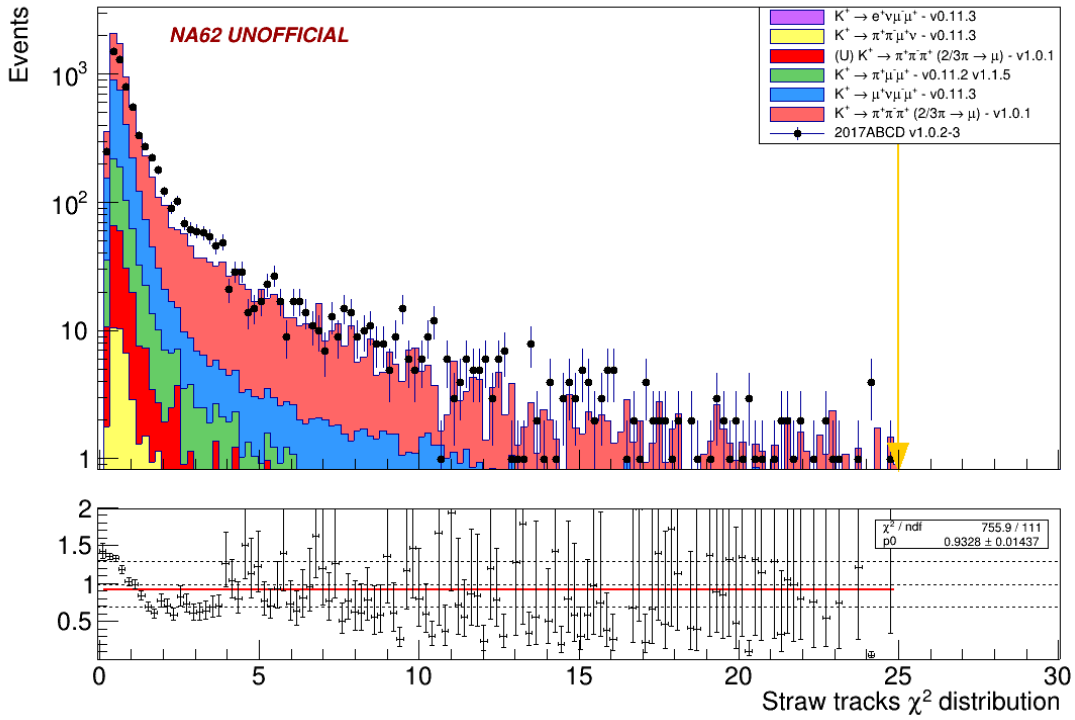

Figure 4.23: Straw tracks χ^2 for $K_{\mu\nu\mu\mu}$ events before the final m^2_{miss} cut. The arrow marks the track χ^2 cut applied during the Common selection.

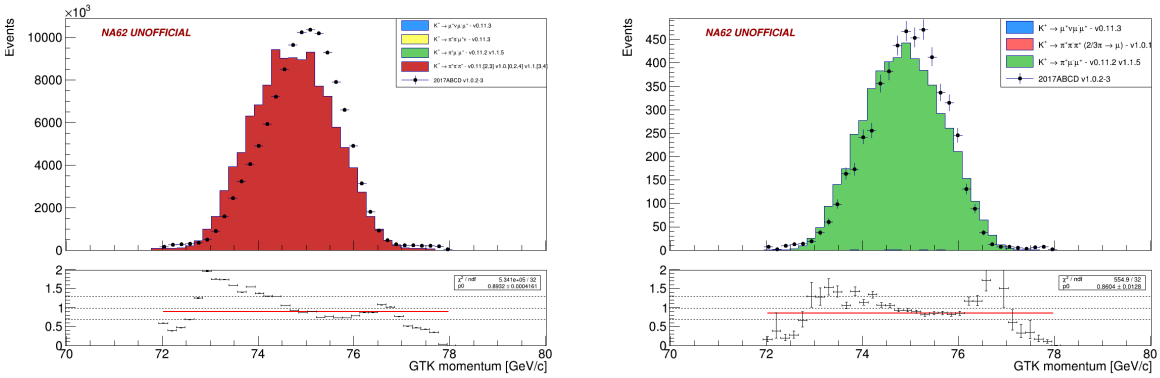

Figure 4.24: GTK tracks momentum for events passing the $K_{3\pi}$ (left) and $K_{\pi\mu\mu}$ (right) event selections.

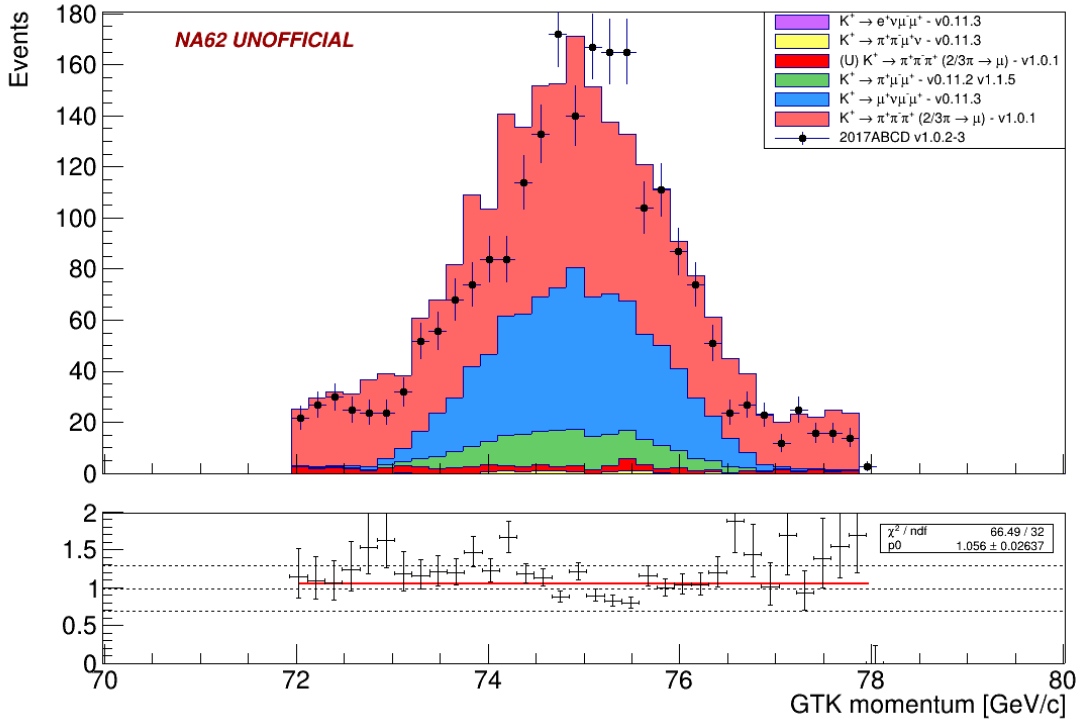

Figure 4.25: GTK track momentum for $K_{\mu\nu\mu\mu}$ events before the final m^2_{miss} cut.

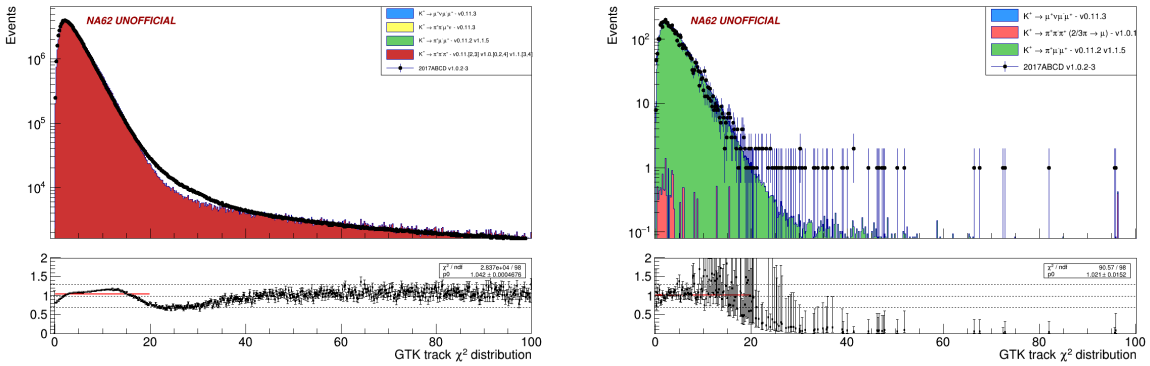

Figure 4.26: GTK track χ^2 for events passing the $K_{3\pi}$ (left) and $K_{\pi\mu\mu}$ (right) event selections.

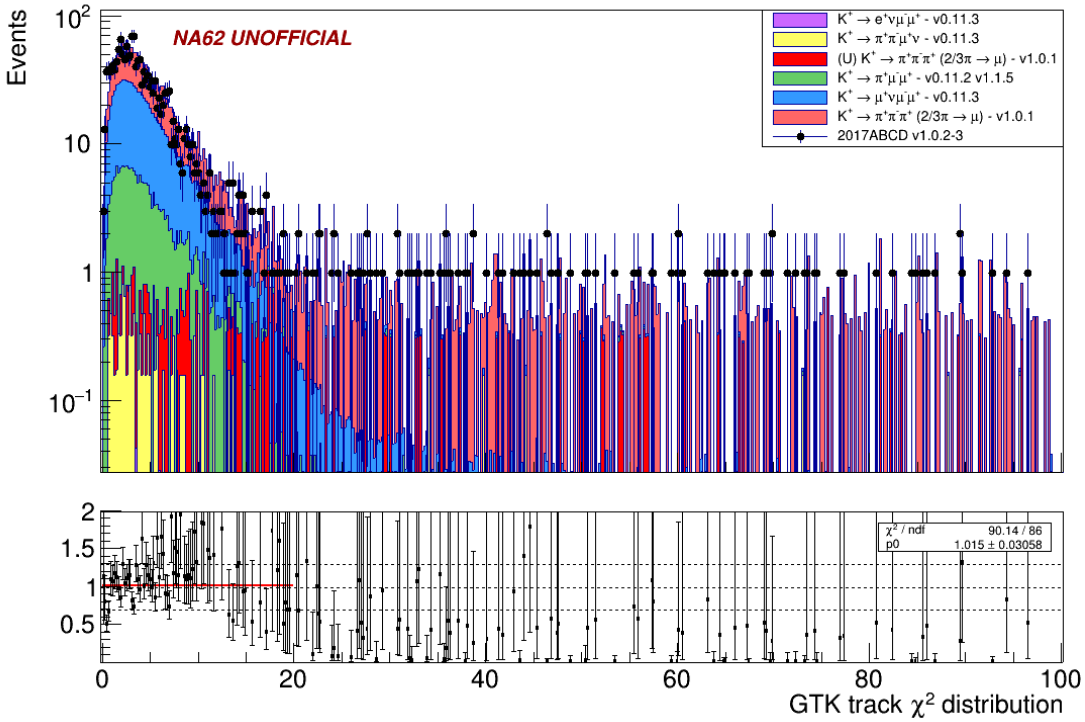

Figure 4.27: GTK track χ^2 for $K_{\mu\nu\mu\mu}$ events before the final m^2_{miss} cut

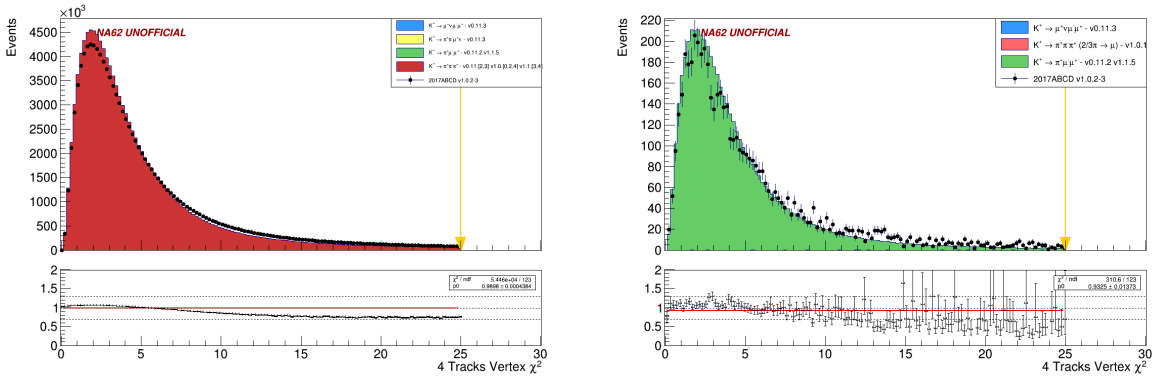

Figure 4.28: Four tracks vertex χ^2 for events passing the $K_{3\pi}$ (left) and $K_{\pi\mu\mu}$ (right) event selections.

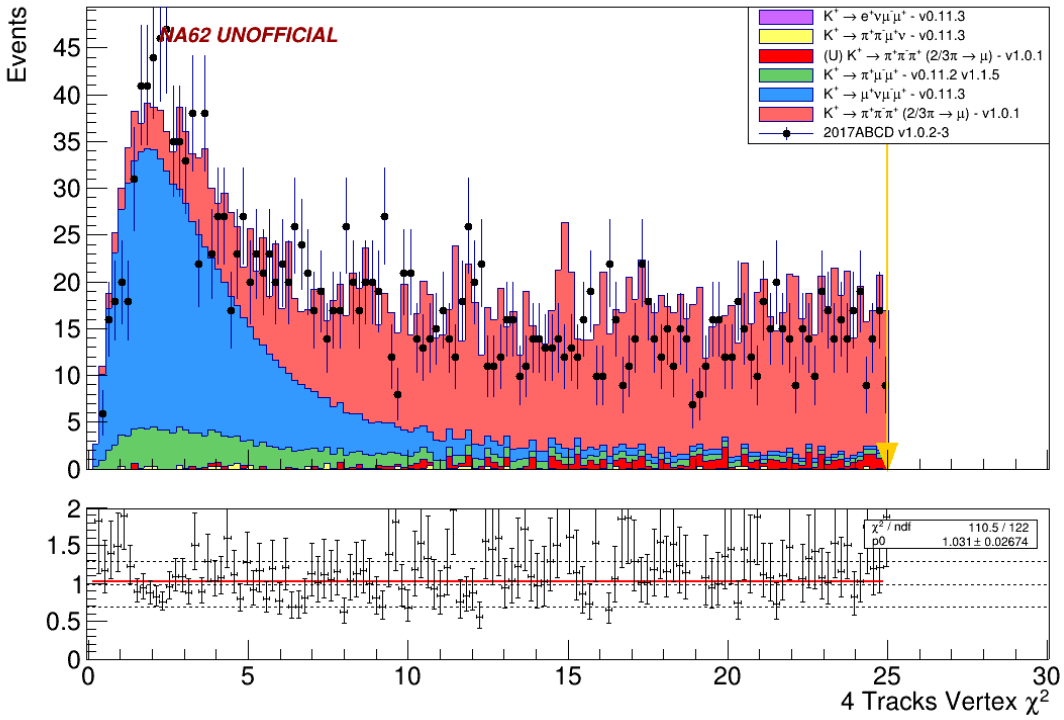

Figure 4.29: Four tracks vertex χ^2 for $K_{\mu\nu\mu\mu}$ events before the final m^2_{miss} cut. The arrow indicates the four tracks vertex χ^2 cut applied during the Common selection.

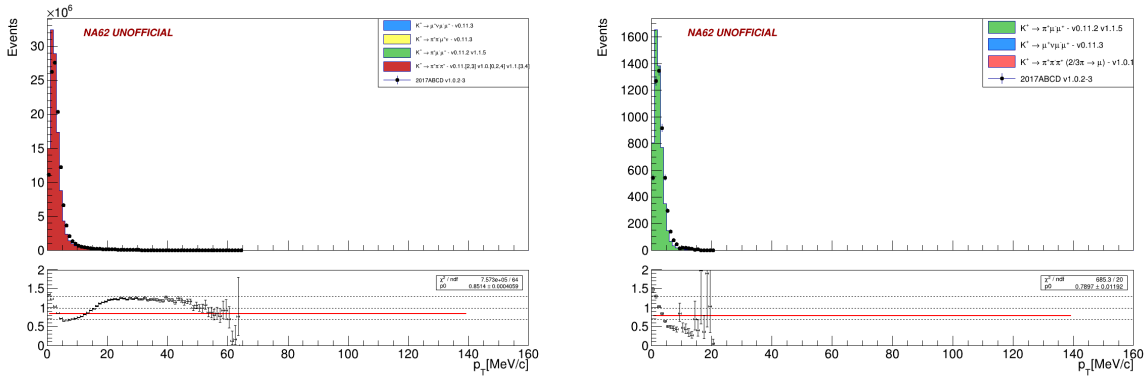

Figure 4.30: GTK transverse momentum for events passing the $K_{3\pi}$ (left) and $K_{\pi\mu\mu}$ (right) event selections.

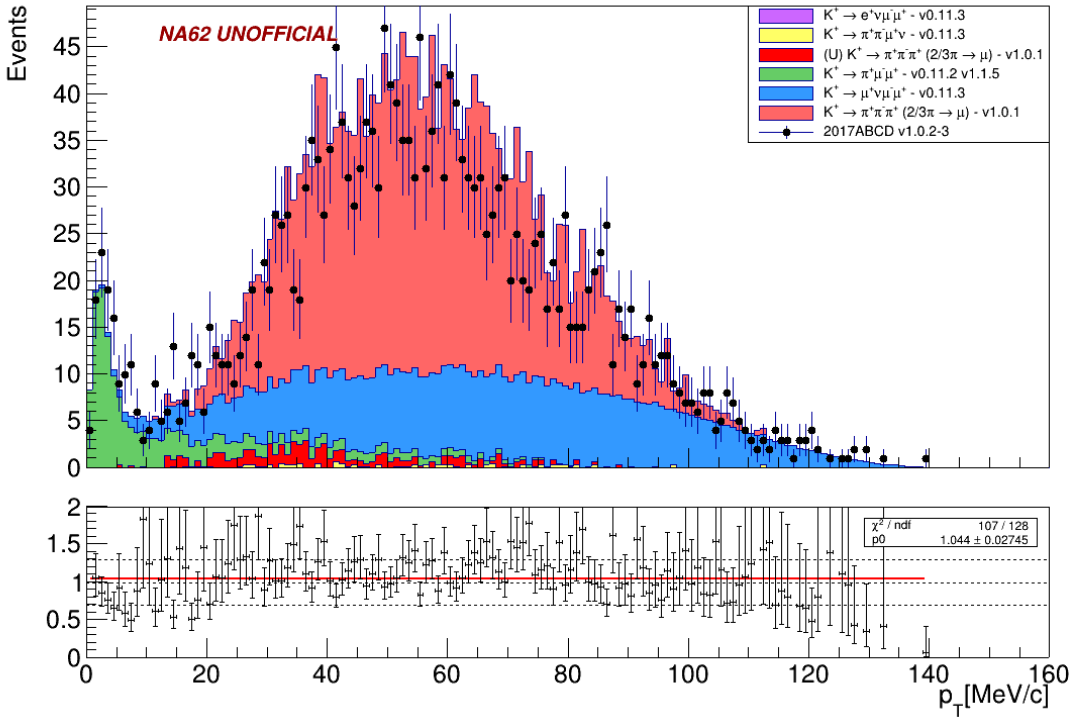

Figure 4.31: GTK transverse momentum for $K_{\mu\nu\mu\mu}$ events before the final m^2_{miss} cut.

5

Conclusions

This work described the

$$K^+ \to \mu^+\nu_\mu\mu^+\mu^- \tag{5.1}$$

analysis selection and the procedure to evaluate its BR. NA62 has demonstrated to be sensitive to this decay and the BR measurement has been calculated for the first time.

The $K_{\mu\nu\mu\mu}$ signal is clearly observable despite the abundant background contamination; this observation is possible thanks to the GTK detector that provides an accurate measure of p_K that is used to compute the transverse momentum and the squared missing mass. Without GTK, the signal peak cannot be resolved from the $K_{3\pi}$ background.

The biggest contribution to the background comes from $K_{3\pi}$ events with three pion decays. Currently, it is possible to describe this particular kind of background only with a Capped MC sample that is rich of those occurrences; despite that, the poor statistic of events, that reach the end of the signal selection, leads to an error on the BR measurement of $\sim$20 %. The NA62 collaboration started to produce a new Monte Carlo sample, in order to describe better the $K_{3\pi}$ events with 3 pion early decays, this is expected to improve the statistical error on the acceptance.

The lack of statistics is not the only concern; indeed, the shape of the background has demonstrated to be dependent by the upstream pileup generator. To quantify that effect

the BR measurement has been performed on different signal regions, the study states that there is no dominant systematic effect driven by the choice of the signal region.

There is room to improve this result and the selection, in particular, the study of the trigger efficiencies has to be performed also on the MC samples, that will estimate $\mathcal{E}_{L0_{MO2}}$ and will allow to exploit the $K_{3\pi}$ normalisation. The emulation of the L0 triggers is already implemented in the NA62 offline software framework, but the most significant source of inefficiencies is coming from the L1 Straw algorithm. The chapter 3 explained the infrastructure and the operations around the NA62 DAQ system; the last section of the chapter described the integration and the validation of the online HLT algorithms into the offline NA62 reconstruction. The technology developed to achieve the integration will be used to execute the HLT algorithms on the MC events and will allow to fully emulate the L1 trigger and understand the Straw efficiency.

In conclusion, the result obtained from the reference signal region on the 2017 data sample is:

$$BR(K^+ \to \mu^+\nu_\mu\mu^+\mu^-) = (1.18 \pm 0.21) \cdot 10^{-8} \qquad err\% = 18\% \tag{5.2}$$

which is compatible with the theoretical estimation obtained from the Chiral Perturbation Theory[10]. The amount of $K^+ \to \mu^+\nu_\mu\mu^+\mu^-$ events observed is:

$$n_{K_{\mu\nu\mu\mu}} = (601 \pm 106) \qquad err\% = 18\%. \tag{5.3}$$

The 2018 sample still needs to be analysed and is expected to provide more than a factor two of events.

6

Appendix

6.1 Normalisation acceptances

Version	$A_{K_{3\pi}}(K_{3\pi})$	err%
v0.11.2	(0.1031 ±0.0003)	0.3%
v0.11.3	(0.1032 ±0.0003)	0.3%
v1.0.0	(0.1012 ±0.0003)	0.3%
v1.0.2	(0.1011 ±0.0003)	0.3%
v1.0.4	(0.1035 ±0.0003)	0.3%
v1.1.3	(0.1031 ±0.0002)	0.2%
v1.1.4	(0.10186 ±0.00004)	0.04%

Table 6.1: The table lists the acceptances of the $K_{3\pi}$ MC samples to the $K_{3\pi}$ selection. The error associated to the acceptance is calculated with the binomial error.

Version	$A_{K_{\pi\mu\mu}}(K_{\pi\mu\mu})$	err%
v0.11.2	(0.0641 $\pm$0.0001)	0.2%
v1.1.5	(0.0628 $\pm$0.0001)	0.2%

Table 6.2: The table lists the acceptances of the $K_{\pi\mu\mu}$ MC samples to the $K_{\pi\mu\mu}$ selection. The error associated to the acceptance is calculated with the binomial error.

6.2 Squared missing mass calculation

In this section the $K_{\mu\nu\mu\mu}$ squared missing mass will be derived. The spectrum of this quantity is used to count the $K_{\mu\nu\mu\mu}$ observed events. The missing mass is defined as follows:

$$m^2_{miss} = (p_K - \sum_i^3 p_{\mu_i})^2 = (p_K - p_{\mu_1} - p_{\mu_2} - p_{\mu_3})^2 \tag{6.1}$$

where p is the four-momentum.

$$\begin{aligned} m^2_{miss} = (E_K - E_{\mu_1} - E_{\mu_2} - E_{\mu_3}, \vec{p_K} - \vec{p_{\mu_1}} - \vec{p_{\mu_2}} - \vec{p_{\mu_3}})^2 \\ = (E_K - E_{\mu_1} - E_{\mu_2} - E_{\mu_3})^2 - [(p_{K_x} - p_{\mu_{1_x}} - p_{\mu_{2_x}} - p_{\mu_{3_x}})^2 \\ +(p_{K_y} - p_{\mu_{1_y}} - p_{\mu_{2_y}} - p_{\mu_{3_y}})^2 + (p_{K_z} - p_{\mu_{1_z}} - p_{\mu_{2_z}} - p_{\mu_{3_z}})^2] \end{aligned} \tag{6.2}$$

Considering generic spacial term: $(p_{K_j} - p_{\mu_{1_j}} - p_{\mu_{2_j}} - p_{\mu_{3_j}})^2$ where j can be x, y or z and reminding the remarkable product:

$$\begin{aligned} (a-b-c-d)^2 = (a-b-c-d)\cdot(a-b-c-d) \\ = a^2 + b^2 + c^2 + d^2 - 2ab - 2ac - 2ad + 2bc + 2bd + 2cd \end{aligned} \tag{6.3}$$

gives the following result:

$$\begin{aligned} (p_{K_j} - p_{\mu_{1_j}} - p_{\mu_{2_j}} - p_{\mu_{3_j}})^2 \\ = p^2_{K_j} + p^2_{\mu_{1_j}} + p^2_{\mu_{2_j}} + p^2_{\mu_{3_j}} \\ -2p_{K_j}p_{\mu_{1_j}} - 2p_{K_j}p_{\mu_{2_j}} - 2p_{K_j}p_{\mu_{3_j}} \\ +2p_{\mu_{1_j}}p_{\mu_{2_j}} + 2p_{\mu_{1_j}}p_{\mu_{3_j}} + 2p_{\mu_{2_j}}p_{\mu_{3_j}} \end{aligned} \tag{6.4}$$

The sum over the three x, y and z components leads to:

$$\begin{aligned}
(p_{K_x} - p_{\mu 1_x} - p_{\mu 2_x} - p_{\mu 3_x})^2 + (p_{K_y} - p_{\mu 1_y} - p_{\mu 2_y} - p_{\mu 3_y})^2 + (p_{K_z} - p_{\mu 1_z} - p_{\mu 2_z} - p_{\mu 3_z})^2 \\
= p_{K_x}^2 + p_{\mu 1_x}^2 + p_{\mu 2_x}^2 + p_{\mu 3_x}^2 \\
-2p_{K_x}p_{\mu 1_x} - 2p_{K_x}p_{\mu 2_x} - 2p_{K_x}p_{\mu 3_x} \\
+2p_{\mu 1_x}p_{\mu 2_x} + 2p_{\mu 1_x}p_{\mu 3_x} + 2p_{\mu 2_x}p_{\mu 3_x} \\
+p_{K_y}^2 + p_{\mu 1_y}^2 + p_{\mu 2_y}^2 + p_{\mu 3_y}^2 \\
-2p_{K_y}p_{\mu 1_y} - 2p_{K_y}p_{\mu 2_y} - 2p_{K_y}p_{\mu 3_y} \\
+2p_{\mu 1_y}p_{\mu 2_y} + 2p_{\mu 1_y}p_{\mu 3_y} + 2p_{\mu 2_y}p_{\mu 3_y} \\
+p_{K_z}^2 + p_{\mu 1_z}^2 + p_{\mu 2_z}^2 + p_{\mu 3_z}^2 \\
-2p_{K_z}p_{\mu 1_z} - 2p_{K_z}p_{\mu 2_z} - 2p_{K_z}p_{\mu 3_z} \\
+2p_{\mu 1_z}p_{\mu 2_z} + 2p_{\mu 1_z}p_{\mu 3_z} + 2p_{\mu 2_z}p_{\mu 3_z} \\
= p_{K_x}^2 + p_{K_y}^2 + p_{K_z}^2 + p_{\mu 1_x}^2 + p_{\mu 1_y}^2 + p_{\mu 1_z}^2 + p_{\mu 2_x}^2 + p_{\mu 2_y}^2 + p_{\mu 2_z}^2 + p_{\mu 3_x}^2 + p_{\mu 3_y}^2 + p_{\mu 3_z}^2 \\
-2(p_{K_x}p_{\mu 1_x} + p_{K_y}p_{\mu 1_y} + p_{K_z}p_{\mu 1_z}) \\
-2(p_{K_x}p_{\mu 2_x} + p_{K_y}p_{\mu 2_y} + p_{K_z}p_{\mu 2_z}) \\
-2(p_{K_x}p_{\mu 3_x} + p_{K_y}p_{\mu 3_y} + p_{K_z}p_{\mu 3_z}) \\
+2(p_{\mu 1_x}p_{\mu 2_x} + p_{\mu 1_y}p_{\mu 2_y} + p_{\mu 1_z}p_{\mu 2_z}) \\
+2(p_{\mu 1_x}p_{\mu 3_x} + p_{\mu 1_y}p_{\mu 3_y} + p_{\mu 1_z}p_{\mu 3_z}) \\
+2(p_{\mu 2_x}p_{\mu 3_x} + p_{\mu 2_y}p_{\mu 3_y} + p_{\mu 2_z}p_{\mu 3_z})
\end{aligned} \tag{6.5}$$

Then reminding that:

$$p_{j_x}p_{k_x} + p_{j_y}p_{k_y} + p_{j_z}p_{k_z} = p_j \cdot p_k = \left|\vec{p_j}\right|^2 |\vec{p_k}|^2 \cos(\theta_{jk}) \tag{6.6}$$

can be rewritten as:

$$\begin{aligned}
(p_{K_x} - p_{\mu 1_x} - p_{\mu 2_x} - p_{\mu 3_x})^2 + (p_{K_y} - p_{\mu 1_y} - p_{\mu 2_y} - p_{\mu 3_y})^2 + (p_{K_z} - p_{\mu 1_z} - p_{\mu 2_z} - p_{\mu 3_z})^2 \\
= |\vec{p_K}|^2 + \left|\vec{p_{\mu 1}}\right|^2 + \left|\vec{p_{\mu 2}}\right|^2 + \left|\vec{p_{\mu 3}}\right|^2 \\
-2|\vec{p_K}|^2\left|\vec{p_{\mu 1}}\right|^2 \cos(\theta_{K\mu 1}) - 2|\vec{p_K}|^2\left|\vec{p_{\mu 2}}\right|^2 \cos(\theta_{K\mu 2}) - 2|\vec{p_K}|^2\left|\vec{p_{\mu 3}}\right|^2 \cos(\theta_{K\mu 3}) \\
+2\left|\vec{p_{\mu 1}}\right|^2\left|\vec{p_{\mu 2}}\right|^2 \cos(\theta_{\mu 1\mu 2}) + 2\left|\vec{p_{\mu 1}}\right|^2\left|\vec{p_{\mu 3}}\right|^2 \cos(\theta_{\mu 1\mu 3}) + 2\left|\vec{p_{\mu 2}}\right|^2\left|\vec{p_{\mu 3}}\right|^2 \cos(\theta_{\mu 2\mu 3})
\end{aligned} \tag{6.7}$$

Concerning the energy term: $(E_K - E_{\mu_1} - E_{\mu_2} - E_{\mu_3})^2$, the remarkable product in equation 6.3 and the following relation:

$$E = \sqrt{m^2 + |\vec{p}|^2}, \tag{6.8}$$

it is possible to derive:

$$\begin{aligned}
&(E_K - E_{\mu_1} - E_{\mu_2} - E_{\mu_3})^2 \\
&= E_K^2 - E_{\mu_1}^2 - E_{\mu_2}^2 - E_{\mu_3}^2 \\
&-2E_K E_{\mu_1} - 2E_K E_{\mu_2} - 2E_K E_{\mu_3} \\
&+2E_{\mu_1} E_{\mu_2} + 2E_{\mu_1} E_{\mu_3} + 2E_{\mu_2} E_{\mu_3} \\
&= m_k^2 + 3m_\mu^2 + |\vec{p_K}|^2 + \left|\vec{p_{\mu_1}}\right|^2 + \left|\vec{p_{\mu_2}}\right|^2 + \left|\vec{p_{\mu_3}}\right|^2 \\
&-2\sqrt{m_K^2 + |\vec{p_K}|^2}\sqrt{m_\mu^2 + \left|\vec{p_{\mu_1}}\right|^2} - 2\sqrt{m_K^2 + |\vec{p_K}|^2}\sqrt{m_\mu^2 + \left|\vec{p_{\mu_2}}\right|^2} - 2\sqrt{m_K^2 + |\vec{p_K}|^2}\sqrt{m_\mu^2 + \left|\vec{p_{\mu_3}}\right|^2} \\
&+2\sqrt{m_\mu^2 + \left|\vec{p_{\mu_1}}\right|^2}\sqrt{m_\mu^2 + \left|\vec{p_{\mu_2}}\right|^2} + 2\sqrt{m_\mu^2 + \left|\vec{p_{\mu_1}}\right|^2}\sqrt{m_\mu^2 + \left|\vec{p_{\mu_3}}\right|^2} + 2\sqrt{m_\mu^2 + \left|\vec{p_{\mu_2}}\right|^2}\sqrt{m_\mu^2 + \left|\vec{p_{\mu_3}}\right|^2}
\end{aligned} \tag{6.9}$$

Putting energy and spacial terms together:

$$\begin{aligned}
m_{miss}^2 &= m_k^2 + 3m_\mu^2 + |\vec{p_K}|^2 + \left|\vec{p_{\mu_1}}\right|^2 + \left|\vec{p_{\mu_2}}\right|^2 + \left|\vec{p_{\mu_3}}\right|^2 \\
&-2\sqrt{m_K^2 + |\vec{p_K}|^2}\sqrt{m_\mu^2 + \left|\vec{p_{\mu_1}}\right|^2} - 2\sqrt{m_K^2 + |\vec{p_K}|^2}\sqrt{m_\mu^2 + \left|\vec{p_{\mu_2}}\right|^2} \\
&-2\sqrt{m_K^2 + |\vec{p_K}|^2}\sqrt{m_\mu^2 + \left|\vec{p_{\mu_3}}\right|^2} + 2\sqrt{m_\mu^2 + \left|\vec{p_{\mu_1}}\right|^2}\sqrt{m_\mu^2 + \left|\vec{p_{\mu_2}}\right|^2} \\
&+2\sqrt{m_\mu^2 + \left|\vec{p_{\mu_1}}\right|^2}\sqrt{m_\mu^2 + \left|\vec{p_{\mu_3}}\right|^2} + 2\sqrt{m_\mu^2 + \left|\vec{p_{\mu_2}}\right|^2}\sqrt{m_\mu^2 + \left|\vec{p_{\mu_3}}\right|^2} \\
&-(|\vec{p_K}|^2 + \left|\vec{p_{\mu_1}}\right|^2 + \left|\vec{p_{\mu_2}}\right|^2 + \left|\vec{p_{\mu_3}}\right|^2 \\
&-2|\vec{p_K}|^2\left|\vec{p_{\mu_1}}\right|^2\cos(\theta_{K\mu_1}) - 2|\vec{p_K}|^2\left|\vec{p_{\mu_2}}\right|^2\cos(\theta_{K\mu_2}) - 2|\vec{p_K}|^2\left|\vec{p_{\mu_3}}\right|^2\cos(\theta_{K\mu_3}) \\
&+2\left|\vec{p_{\mu_1}}\right|^2\left|\vec{p_{\mu_2}}\right|^2\cos(\theta_{\mu_1\mu_2}) + 2\left|\vec{p_{\mu_1}}\right|^2\left|\vec{p_{\mu_3}}\right|^2\cos(\theta_{\mu_1\mu_3}) + 2\left|\vec{p_{\mu_2}}\right|^2\left|\vec{p_{\mu_3}}\right|^2\cos(\theta_{\mu_2\mu_3}))
\end{aligned} \tag{6.10}$$

That leads to:

$$\begin{aligned}
m_{miss}^2 = m_k^2 + 3m_\mu^2 &- 2\sqrt{m_K^2 + |\vec{p_K}|^2}\sqrt{m_\mu^2 + \left|\vec{p_{\mu_1}}\right|^2} - 2\sqrt{m_K^2 + |\vec{p_K}|^2}\sqrt{m_\mu^2 + \left|\vec{p_{\mu_2}}\right|^2} \\
&-2\sqrt{m_K^2 + |\vec{p_K}|^2}\sqrt{m_\mu^2 + \left|\vec{p_{\mu_3}}\right|^2} + 2\sqrt{m_\mu^2 + \left|\vec{p_{\mu_1}}\right|^2}\sqrt{m_\mu^2 + \left|\vec{p_{\mu_2}}\right|^2} \\
&+2\sqrt{m_\mu^2 + \left|\vec{p_{\mu_1}}\right|^2}\sqrt{m_\mu^2 + \left|\vec{p_{\mu_3}}\right|^2} + 2\sqrt{m_\mu^2 + \left|\vec{p_{\mu_2}}\right|^2}\sqrt{m_\mu^2 + \left|\vec{p_{\mu_3}}\right|^2} \\
&+2|\vec{p_K}|^2\left|\vec{p_{\mu_1}}\right|^2\cos(\theta_{K\mu_1}) + 2|\vec{p_K}|^2\left|\vec{p_{\mu_2}}\right|^2\cos(\theta_{K\mu_2}) + 2|\vec{p_K}|^2\left|\vec{p_{\mu_3}}\right|^2\cos(\theta_{K\mu_3}) \\
&-2\left|\vec{p_{\mu_1}}\right|^2\left|\vec{p_{\mu_2}}\right|^2\cos(\theta_{\mu_1\mu_2}) - 2\left|\vec{p_{\mu_1}}\right|^2\left|\vec{p_{\mu_3}}\right|^2\cos(\theta_{\mu_1\mu_3}) - 2\left|\vec{p_{\mu_2}}\right|^2\left|\vec{p_{\mu_3}}\right|^2\cos(\theta_{\mu_2\mu_3})
\end{aligned} \tag{6.11}$$

Please notice that in the equation are present all the angles between the kaon and muons: $\theta_{K\mu_1}$, $\theta_{K\mu_2}$ and $\theta_{K\mu_3}$; and all reciprocal angles between muons: $\theta_{\mu_1\mu_2}$, $\theta_{\mu_1\mu_3}$ and $\theta_{\mu_2\mu_3}$.

Bibliography

[1] Andrzej J. Buras et al. "$K^+ \to \pi^+ \nu\bar{\nu}$ and $K_L \to \pi^0 \nu\bar{\nu}$ in the Standard Model: status and perspectives". In: *Journal of High Energy Physics* 2015.11 (Mar. 2015), pp. 1–34. ISSN: 10298479. DOI: 10.1007/JHEP11(2015)033. URL: http://arxiv.org/abs/1503.02693%20http://dx.doi.org/10.1007/JHEP11(2015)033.

[2] M. Tanabashi et al. "Review of Particle Physics". English (US). In: *Physical Review D - Particles, Fields, Gravitation and Cosmology* 98.3 (Aug. 2018). ISSN: 1550-7998. DOI: https://doi.org/10.1103/PhysRevD.98.030001.

[3] Johan Bijnens. "Chiral perturbation theory beyond one loop". In: *Progress in Particle and Nuclear Physics* 58.2 (Apr. 2007), pp. 521–586. ISSN: 01466410. DOI: 10.1016/j.ppnp.2006.08.002. URL: https://linkinghub.elsevier.com/retrieve/pii/S014664100600072X.

[4] J. Gasser et al. "Chiral perturbation theory: Expansions in the mass of the strange quark". In: *Nuclear Physics B* 250.1-4 (Jan. 1985), pp. 465–516. ISSN: 0550-3213. DOI: 10.1016/0550-3213(85)90492-4. URL: https://www.sciencedirect.com/science/article/pii/0550321385904924.

[5] G. Ecker. "Strong interactions of light flavours". In: (Nov. 2000). URL: http://arxiv.org/abs/hep-ph/0011026.

[6] Gerhard Ecker. "Chiral symmetry". In: *Broken Symmetries*. Springer Berlin Heidelberg, 1999, pp. 83–129. DOI: 10.1007/BFb0105525. URL: http://link.springer.com/10.1007/BFb0105525.

[7] Vincenzo Cirigliano et al. "Two-Loop Effective Theory Analysis of $\pi(K) \to e\bar{\nu}_e[\gamma]$ Branching Ratios". In: *Physical Review Letters* 99.23 (Dec. 2007), p. 231801. ISSN: 0031-9007. DOI: 10.1103/PhysRevLett.99.231801. URL: https://link.aps.org/doi/10.1103/PhysRevLett.99.231801.

[8] C. Lazzeroni et al. "Precision measurement of the ratio of the charged kaon leptonic decay rates". In: *Physics Letters B* 719.4-5 (Feb. 2013), pp. 326–336. ISSN: 03702693. DOI: 10.1016/j.physletb.2013.01.037. URL: https://linkinghub.elsevier.com/retrieve/pii/S0370269313000786.

[9] S. Dawson. "Higgs boson production in semi-leptonic K and π decays". In: *Physics Letters B* 222.1 (May 1989), pp. 143–148. ISSN: 0370-2693. DOI: 10.1016/0370-2693(89)90737-5. URL: https://www.sciencedirect.com/science/article/pii/0370269389907375.

[10] J. Bijnens et al. "Radiative Semileptonic Kaon Decays". In: (Sept. 1992). DOI: 10.1016/0550-3213(93)90259-R. URL: http://arxiv.org/abs/hep-ph/9209261%20http://dx.doi.org/10.1016/0550-3213(93)90259-R.

[11] M. S. Atiya et al. "Search for a light Higgs boson in the decay $K^+ \to \pi^+ H, H \to \mu^+\mu^-$". In: *Physical Review Letters* 63.20 (Nov. 1989), pp. 2177–2180. ISSN: 00319007. DOI: 10.1103/PhysRevLett.63.2177. URL: https://link.aps.org/doi/10.1103/PhysRevLett.63.2177.

[12] Gordan Krnjaic et al. "Probing Muonic Forces and Dark Matter at Kaon Factories". In: (Feb. 2019). URL: http://arxiv.org/abs/1902.07715.

[13] M.S. Atiya et al. "A detector to search for $K^+ \to \pi^+ \nu\bar{\nu}$". In: *Nuclear Instruments and Methods in Physics Research Section A: Accelerators, Spectrometers, Detectors and Associated Equipment* 321.1-2 (Sept. 1992), pp. 129–151. ISSN: 0168-9002. DOI: 10.1016/0168-9002(92)90382-E. URL: https://www.sciencedirect.com/science/article/pii/016890029290382E.

[14] S. Adler et al. "Measurement of the $K^+ \to \pi^+ \nu\bar{\nu}$ branching ratio". In: *Physical Review D* 77.5 (Mar. 2008), p. 052003. ISSN: 1550-7998. DOI: 10.1103/PhysRevD.77.052003. URL: https://link.aps.org/doi/10.1103/PhysRevD.77.052003.

[15] E. Cortina Gil et al. "The beam and Detector of the NA62 experiment at CERN". In: *Journal of Instrumentation* 12.5 (May 2017), P05025–P05025. ISSN: 17480221. DOI: 10.1088/1748-0221/12/05/P05025. URL: http://stacks.iop.org/1748-0221/12/i=05/a=P05025?key=crossref.ea7c38eed4dd9ae7326b0dbaf0ed6ed7.

[16] *NA62: Technical Design Document*. Dec. 2010. URL: http://cds.cern.ch/record/1404985.

[17] John R Fry et al. "Precision magnetic field mapping for CERN experiment NA62". In: *Journal of Physics G: Nuclear and Particle Physics* 43.12 (Dec. 2016), p. 125004. ISSN: 0954-3899. DOI: 10.1088/0954-3899/43/12/125004. URL: http://stacks.iop.org/0954-3899/43/i=12/a=125004?key=crossref.8343d44856461cc1a6e9f6e30d136991.

[18] Alexander Kluge et al. "NA62 Giga Tracker". In: *Proceedings of 19th International Workshop on Vertex Detectors PoS(VERTEX 2010)*. Vol. 113. Trieste, Italy: Sissa Medialab, Feb. 2011, p. 040. DOI: 10.22323/1.113.0040. URL: https://pos.sissa.it/113/040.

[19] G. Aglieri Rinella et al. "The NA62 GigaTracKer: a low mass high intensity beam 4D tracker with 65 ps time resolution on tracks". In: *Journal of Instrumentation* 14.07 (July 2019), P07010–P07010. ISSN: 1748-0221. DOI: 10.1088/1748-0221/14/07/P07010. URL: https://iopscience.iop.org/article/10.1088/1748-0221/14/07/P07010.

[20] "The OPAL detector at LEP". In: *Nuclear Instruments and Methods in Physics Research Section A: Accelerators, Spectrometers, Detectors and Associated Equipment* 305.2 (July 1991), pp. 275–319. ISSN: 0168-9002. DOI: 10.1016/0168-9002(91)90547-4. URL: https://www.sciencedirect.com/science/article/pii/0168900291905474.

[21] V. Fanti et al. "The beam and detector for the NA48 neutral kaon CP violation experiment at CERN". In: *Nuclear Instruments and Methods in Physics Research Section A: Accelerators, Spectrometers, Detectors and Associated Equipment* 574.3 (May 2007), pp. 433–471. ISSN: 0168-9002. DOI: 10.1016/J.NIMA.2007.01.178. URL: https://www.sciencedirect.com/science/article/pii/S0168900207002719?via%3Dihub.

[22] R. Ammendola et al. "The integrated low-level trigger and readout system of the CERN NA62 experiment". In: *Nuclear Instruments and Methods in Physics Research Section A: Accelerators, Spectrometers, Detectors and Associated Equipment* 929 (June 2019), pp. 1–22. ISSN: 0168-9002. DOI: 10.1016/J.NIMA.2019.03.012. URL: https://www.sciencedirect.com/science/article/pii/S0168900219303055.

[23] B G Taylor. "Timing distribution at the LHC". In: (2002). DOI: 10.5170/CERN-2002-003.63. URL: http://cds.cern.ch/record/592719.

[24] B. Angelucci et al. "TEL62: an integrated trigger and data acquisition board". In: *2011 IEEE Nuclear Science Symposium Conference Record*. IEEE, Oct. 2011, pp. 823–826. ISBN: 978-1-4673-0120-6. DOI: 10.1109/NSSMIC.2011.6154547. URL: http://ieeexplore.ieee.org/document/6154547/.

[25] G. Haefeli et al. "The LHCb DAQ interface board TELL1". In: *Nuclear Instruments and Methods in Physics Research Section A: Accelerators, Spectrometers, Detectors and Associated Equipment* 560.2 (May 2006), pp. 494–502. ISSN: 0168-9002. DOI: 10.1016/J.NIMA.2005.12.212. URL: https://www.sciencedirect.com/science/article/pii/S0168900205026100.

[26] J Christiansen. *HPTDC High Performance Time to Digital Converter*. 2004. URL: http://cds.cern.ch/record/1067476.

[27] G. Aglieri Rinella et al. "The TDCpix Readout ASIC: A 75 ps Resolution Timing Front-End for the Gigatrackerof theNA62 Experiment". In: *Physics Procedia* 37 (Jan. 2012), pp. 1608–1617. ISSN: 1875-3892. DOI: 10.1016/J.PHPRO.2012.04.106. URL: https://www.sciencedirect.com/science/article/pii/S1875389212018779.

[28] D. Moraes et al. *The CARIOCA Front End Chip for the LHCb muon chambers*. Jan. 2003. URL: http://inspirehep.net/record/928997/.

[29] A Ceccucci et al. "The NA62 Liquid Krypton calorimeter readout module". In: *Journal of Instrumentation* 6.12 (Dec. 2011), pp. C12017–C12017. ISSN: 1748-0221. DOI: 10.1088/1748-0221/6/12/C12017. URL: http://stacks.iop.org/1748-0221/6/i=12/a=C12017?key=crossref.7bd1f0b3255e1ca83de22685137ca440.

[30] URL: https://www.caen.it/.

[31] D. Soldi et al. "Level Zero Trigger Processor for the NA62 experiment". In: *Journal of Instrumentation* 13.5 (May 2018), P05004–P05004. ISSN: 17480221. DOI: 10.1088/1748-0221/13/05/P05004. URL: http://stacks.iop.org/1748-0221/13/i=05/a=P05004?key=crossref.060df8d3e9456e5b72d9e86fb250b499.

[32] Marco Boretto. "The data acquisition system of the NA62 experiment at CERN". In: *EPJ Web of Conferences* 214 (Sept. 2019). Ed. by A. Forti et al., p. 01037. ISSN: 2100-014X. DOI: 10.1051/epjconf/201921401037. URL: https://www.epj-conferences.org/10.1051/epjconf/201921401037.

[33] *Brocade Data sheet*. URL: http://www.dataswitchworks.com/datasheets/brocade-icx-7750-ds.pdf.

[34] Ansible IT automation engine. URL: https://www.ansible.com.

[35] Scientific Linux CERN 6. URL: http://linux.web.cern.ch/linux/scientific6.

[36] CERN CentOS 7. URL: http://linux.web.cern.ch/linux/centos7.

[37] Red Hat Enterprise Linux is a Linux distribution developed by Red Hat. URL: https://www.redhat.com/en/technologies/linux-platforms/enterprise-linux.

[38] CentOS a Linux distribution compatible with its upstream source Red Hat Enterprise Linux. URL: https://www.centos.org.

[39] GCC 4.8 series. URL: http://www.gnu.org/software/gcc/gcc-4.8.

[40] ISO/IEC. (2011). ISO International Standard ISO/IEC 14882:2011 Programming Language C++. Geneva, Switzerland. URL: http://www.open-std.org/jtc1/sc22/wg21/docs/papers/2012/n3337.pdf.

[41] CERN AIMS2 client https://twiki.cern.ch/twiki/bin/view/LinuxSupport/Aims2.

[42] Ansible configuration for the NA62 cluster https://gitlab.cern.ch/ep-dt-di/daq/na62/ansible-na62farm.

[43] RPM package system https://rpm.org.

[44] NA62 DIM interface software repository https://github.com/NA62/na62-farm.

[45] NA62 DAQ-farm software repository https://github.com/NA62/na62-farm.

[46] NA62 Merger software repository https://github.com/NA62/na62-farm-merger.

[47] NA62 farm library https://github.com/NA62/na62-farm-lib.

[48] NA62 trigger algorithms software repository https://github.com/NA62/na62-trigger-algorithms.

[49] Nicolas Lurkin. "The NA62 Run Control". In: *2013 IEEE Nuclear Science Symposium and Medical Imaging Conference (2013 NSS/MIC)*. IEEE, Oct. 2013, pp. 1–4. ISBN: 978-1-4799-0534-8. DOI: 10.1109/NSSMIC.2013.6829575. URL: http://ieeexplore.ieee.org/document/6829575/.

[50] C. Gaspar et al. "DIM, a portable, light weight package for information publishing, data transfer and inter-process communication". In: *Computer Physics Communications* 140.1-2 (Oct. 2001), pp. 102–109. ISSN: 0010-4655. DOI: 10.1016/S0010-4655(01)00260-0. URL: https://www.sciencedirect.com/science/article/pii/S0010465501002600.

[51] *PF_RING*. URL: https://www.ntop.org/products/packet-capture/pf_ring/.

[52] *ZMQ*. URL: http://zeromq.org/.

[53] URL: http://www.cplusplus.com/reference/map/map/.

[54] URL: https://en.cppreference.com/w/cpp/thread/condition_variable.

[55] *CASTOR CERN Advanced STORage manager*. URL: http://castor.web.cern.ch/.

[56] *FTS File Transfer Service*. URL: https://fts.web.cern.ch/.

[57] *Globus Grid FTP server*. URL: https://www.globus.org/.

[58] *MariaDB*. URL: https://mariadb.org/.

[59] NA62 CDR software https://gitlab.cern.ch/mboretto/cdr.

[60] FTS3 rest API https://pypi.org/project/fts3-rest-API.

[61] Elastic Stack is a complete end-to-end log analysis solution. URL: https://www.elastic.co/products.

[62] Lightweight Shipper for Logs. URL: https://www.elastic.co/products/beats/filebeat.

[63] Logstash is server-side data processing pipeline that ingests data from a multitude of sources and transforms it. URL: https://www.elastic.co/products/logstash.

[64] Elasticsearch is a distributed, RESTful search and analytics engine. URL: https://www.elastic.co/products/elasticsearch.

[65] URL: https://www.elastic.co/products/kibana.

[66] J.R. Batley et al. "New measurement of the $K^{\pm} \to \pi^{\pm}\mu^{+}\mu^{-}$ decay". In: *Physics Letters B* 697.2 (Feb. 2011), pp. 107–115. ISSN: 0370-2693. DOI: 10.1016/J.PHYSLETB.2011.01.042. URL: https://www.sciencedirect.com/science/article/pii/S0370269311000797.

[67] The NA62 framework. URL: https://gitlab.cern.ch/NA62FW/na62fw.

[68] The NA62 software website. URL: https://na62-sw.web.cern.ch/software.

[69] The CERN ROOT library. URL: https://root.cern.ch.

[70] The Geant4 library. URL: https://geant4.web.cern.ch.

[71] $K_{\mu\nu\mu\mu}$ analyser repository. URL: https://gitlab.cern.ch/mboretto/kmunumumu.

[72] I. Mandrinchenko. *Kalman fit package*. May 1994. URL: http://inspirehep.net/record/1234634/.